Structural characterisation of autophagy-related protein LC3C

Inaugural-Dissertation

zur Erlangung des Doktorgrades
der Mathematisch-Naturwissenschaftlichen Fakultät
der Heinrich-Heine-Universität Düsseldorf

vorgelegt von

Carsten Krichel
aus Aachen

Plombières, April 2016

aus dem Institut für Physikalische Biologie
der Heinrich-Heine-Universität Düsseldorf

Gedruckt mit der Genehmigung der
Mathematisch-Naturwissenschaftlichen Fakultät der
Heinrich-Heine-Universität Düsseldorf

Referent: Prof. Dr. Dieter Willbold

Koreferent: PD Dr. Oliver Weiergräber

Tag der mündlichen Prüfung: 31.05.2016

Contents

List of Figures

List of Tables

1. Introduction

1.1. Autophagy – A Short Historical Overview

The orchestration of a cell's complex environment is a most astounding characteristic of biological life. The foundation of this interplay is a continuous supply and a prompt availability of elementary molecular building blocks or precursor molecules necessary for cellular homeostasis. Precursor molecules, such as amino acids, are needed for the synthesis of vastly diverse macromolecular cellular components.

A discontinuity in this supply will result in severe cellular stress, and a prolonged absence may endanger cellular survival altogether. Most eukaryotes therefore possess an evolutionarily conserved mechanism which is able to bypass a temporary state of nutrient depletion. When activated, in times of nutrient scarcity and stress, cells resort to partial self-consumption–or *autophagy*–of non-essential cytoplasmic macromolecules.

Autophagy itself is a most interesting cellular phenomenon, for its versatility is unmatched. It allows the degradation of comparably small monomeric proteins as well as larger protein aggregates. Even entire organelles, like mitochondria, and invading pathogens may be decomposited as part of an innate immune response. The first detailed description of the then unnamed autophagic process was published in the late 1950's based on detailed morphological analyses of rodent renal cells and hepatocytes (Novikoff et al., 1956; Clark, 1957).

Soon after these initial observations, *ex vivo* rat hepatocytes have been investigated by glucagon perfusion experiments and lead Ashford and Porter to the conclusion "(...) Possibly some condition it establishes in the cell leads to the development of foci of physiologic autolysis (...) and such areas are automatically surrounded by a membrane (...)" (Ashford and Porter, 1962).

While the relationship between degradation of mitochondria and the involvement of

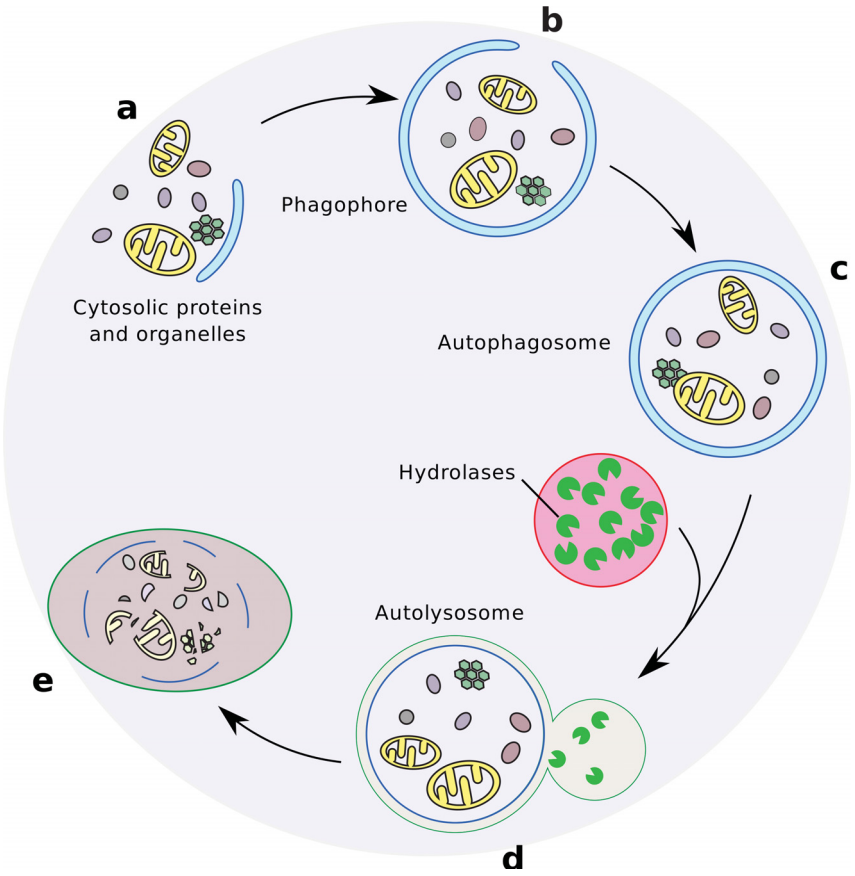

Figure 1.1.: Illustration of cellular macroautophagy. (**a**) Sequestration of cytosolic targets at the phagophore assembly site (PAS), (**b**) phagophore extension and (**c**) formation of a closed, double-membrane vesicle, termed autophagosome. A mature autophagosome fuses with lysosomal organelles (**d**) to create an autolysosome, resulting in the degradation of cargo molecules by hydrolases (**e**) and release of the building blocks into the cytosol. Adapted from Xie and Klionsky (2007).

lysosomal compartments in hepatic cells has been further traced (Novikoff and Essner, 1962), Novikoff suggested “cytolysosomes” as designation for the newly discovered organelles. In the end it was Christian de Duve who coined the term *autophagy* for this phenomenon in the early 1960’s (Klionsky, 2008a).

1.2. Autophagy – The Molecular Era

Optical and electron microscopic observations have been the driving force of advancements in autophagy research. Owing to the physical principles of these meth-

ods and state of the art at the time, research has been restricted to the phenomenological description of microscopic fate and interplay of comparably large organelles involved in autophagy. The way into the molecular and genomic era has been paved when studies of autophagy-deficient *Saccharomyces cerevisiae* yeast mutants resulted in the description of the first autophagy-related (Atg) genes (Takeshige et al., 1992; Tsukada and Ohsumi, 1993; Thumm et al., 1994). With the first Atg gene, coding for a protein later termed autophagy-related 1 (Atg1), the foundation has been laid to decipher a plethora of molecular mechanisms underlying autophagy (Matsuura et al., 1997).

Through genetic analyses of *S. cerevisiae*, until today more than 30 autophagy-related proteins have been identified (Nakatogawa et al., 2009; Weiergräber et al., 2013). Most of these are conserved in higher eukaryotes as well and are often complemented by additional paralogues, possibly due to cell type differentiation in higher eukaryotes and a subsequent necessity to procure additional regulatory options (Feng et al., 2014).

The majority of Atg proteins can be assorted to the autophagic core machinery, which comprises a group of autophagic proteins essential for formation of autophagosomes (Xie and Klionsky, 2007). Autophagosomes are double-membrane vesicles engulfing and sequestering cellular components destined for degradation. Upon initiation of autophagy, e.g. under nutrient deprivation, several Atg proteins are localised at the pre-autophagosomal structure also known as phagophore assembly site (PAS) (Suzuki et al., 2001). Concomitantly, cytosolic targets of autophagy are sequestered and engulfed by a newly emerging cup-shaped structure, a phagophore, which subsequently closes to form a fully developed, double-membrane vesicle termed autophagosome (see also Figure 1.1). The autophagsome matures further by fusion with endosomes containing endocytic markers (Mizushima et al., 2002). And in a final step, through fusion with a lysosome, the autophagosomal inner membrane and autophagic cargo are enzymatically degraded (Nakatogawa et al., 2009). Thereby autophagy provides new building blocks under stress conditions to ensure continuous operation of a cell's biochemical machinery.

The above described intracellular sequestration of cytosolic targets by autophagosome formation is termed non-selective or bulk autophagy and used synonymously with "autophagy" throughout this work. Specific autophagic pathways are named by their primary target organelle including pexophagy–the degradation of peroxisomes–

which has been extensively described for the yeasts *P. pastoris* and *H. polymorpha* (Dunn et al., 2005), and mitophagy, the autophagic degradation route for mitochondria which has been focused by the very first studies of autophagy (Novikoff and Essner, 1962).

Closely related but mechanistically different autophagy processes have been named microautophagy and chaperone mediated autophagy. Whereas the former engulfs part of the cytoplasm by invagination of a lysosome, the latter directly targets single proteins with the help of chaperones (Li et al., 2012).

During autophagosome formation, the autophagic core machinery orchestrates the assembly of essential autophagic proteins. This core machinery can be subdivided into four functional units: (1) the Atg9 cycling system–important for phagophore nucleation–, (2) the Atg1 / Unc-51-like kinase complex–regulating induction of autophagosome formation–, (3) the phosphatidylinositol 3-kinase complex–synthesising phosphatidylinositol 3-phosphate which in turn is essential for recruitment of proteins during autophagosome formation–, and, finally, (4) the Atg12 and Atg8 protein conjugation systems (Mizushima et al., 2011).

1.2.1. Autophagic Protein Conjugation Systems

In 1998, with Atg12, the first protein involved in an autophagic conjugation system has been described. Shortly thereafter, a second protein involved in a different autophagic protein conjugation system, Atg8 (also known as Aut7 or Apg8), has been discovered and since then investigated in depth (Mizushima et al., 1998; Kirisako et al., 2000; Ichimura et al., 2000). The importance of these conjugation systems has become evident by their conservation from simpler unicellular eukaryotic organisms, like yeasts, to highly specialised mammalian cells (Mizushima et al., 1998).

The molecular mechanisms of the autophagic protein conjugation systems are related to the–at the time of discovery–already widely known ubiquitination phenomenon (Pickart, 2001). Similarities are so prevalent that Atg12, Atg8 and their homologues have been labelled ubiquitin-like modifiers (Hochstrasser, 2000). Furthermore, the autophagic machinery utilises enzymes functionally equivalent to ubiquitin activating (E1) and conjugating enzymes (E2), and to ubiquitin-protein ligases (E3) (Pickart, 2001). While Atg12, much like ubiquitin, is covalently coupled to a target protein, Atg8 and its homologues target a phospholipid. The conjugation mechanism is described

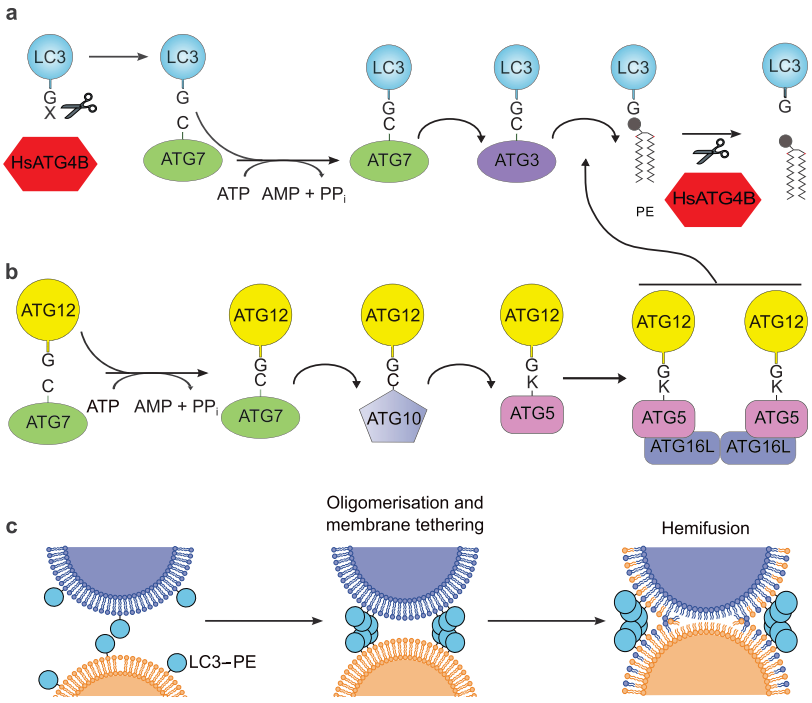

Figure 1.2.: Comparison of Atg8 / LC3 and ATG12 autophagic protein conjugation mechanisms, and the role of lipid-conjugated LC3 in autophagic fusion events. (**a**) Atg8 / LC3 conjugation mechanism. Atg8 / LC3 are processed by cleaving the carboxy-terminus to expose a conserved glycine residue by the cystein protease HsATG4B–the prevalent human ATG4 homologue. Cleaved Atg8 / LC3 is subsequently transfered from E1-like ATG7 to E2-like ATG3, and, finally, to phosphatidylethanolamine (PE) by the E3-like ATG12-ATG5-ATG16L complex. Conjugation of Atg8 / LC3 to PE is reversible by HsATG4B. (**b**) Conjugation of ATG12 to ATG5 is catalysed by E1-like ATG7 and the E2-like ATG10 to form the ATG12-ATG5-ATG16L complex which is essential for Atg8 / LC3-PE formation. (**c**) Atg8 / LC3-PE mediates *in vitro* membrane-tethering and hemifusion of liposomal membranes; *in vivo* Atg8 / LC3-PE expansion of autophagosomal membranes. Adapted from Nakatogawa et al. (2009).

in more detail below (see also Figure 1.2 a and 1.2 b).

In analogy to other ubiquitin-like modifiers, Atg8-like proteins are synthesised as precursor proteins, containing additional carboxy-terminal residue(s), which are then cleaved by an ATG4 protease (see also Figure 1.2 a) (He et al., 2003; Tanida et al., 2004). The action of this enzyme exposes the conserved carboxy-terminal glycine and generates the form-I of an Atg8-like protein (Kabeya et al., 2000; Kirisako et al., 2000; Tanida et al., 2003, 2004). Subsequently, the form-I protein is modified by the concerted action of the E1-like activating enzyme Atg7 and the E2-like conjugating enzyme Atg3 (Ichimura et al., 2000), to be linked, in a final step, via the exposed glycine

to the phospholipid phosphatidylethanolamine (PE) by the E3-like Atg5-Atg12-Atg16 complex (Fujita et al., 2008). This yields, now in contrast to ubiquitination, where the target is a polypeptide, conjugation of an Atg8-like protein to a phospholipid. The lipidated Atg8-like protein is commonly referred to by the suffix II, or PE (e.g. Atg8-II or Atg8-PE). Notably, the deconjugation reaction is again catalysed by ATG4. *In vitro* studies have suggested the possibility of an additional phospholipid target (phosphatidylserine) for mammalian Atg8 homologues, but could not be confirmed *in vivo*, yet (Sou et al., 2006).

Atg12's role as autophagic conjugation system remains–in contrast to Atg8-like proteins–more limited and elusive. It has been established that the Atg5-Atg12 protein complex is a key factor for autophagosom formation and, as illustrated in Figure 1.2 b, essential for Atg8-PE formation (Kim et al., 2001; Fujita et al., 2008). Interestingly, the E1-like activating enzyme Atg7 does not distinguish between Atg12 and Atg8-like proteins and is employed by both conjugation systems.

Although already described in the late 1980s as a protein associating with microtubules and later additionally ascribed a role as regulator of microtubule binding activity (Kuznetsov and Gelfand, 1987; Mann and Hammarback, 1994), it has been in the early 2000s when microtubule-associated protein 1 light chain 3B (MAP1LC3B or LC3B) has been identified as first mammalian Atg8 homologue (Kabeya et al., 2000). Today, at least eight homologous human ATG8 genes have been described (Weiergräber et al., 2013). Through sequence identity they can be subdivided into the GABARAP (γ-aminobutyric acid type A receptor-associated protein)-like and LC3-like protein subfamilies (see also Figure 1.3) (Shpilka et al., 2011). The GABARAP-like protein subfamily consists of eponymous GABARAP, GABARAPL1 (also kown as GEC1), and GABARAPL2 (GATE-16) (Xin et al., 2001). The LC3-like protein subfamily, on the other hand, includes LC3A, LC3B, most extensively studied by cellular biological experiments, and LC3C (He et al., 2003). Expression patterns for each protein vary depending on cell type and tissue. For example, while LC3A is prevalently expressed in cardiomyocytes, the overall less abundant LC3C shows highest concentrations in the lung (He et al., 2003). A consensus on distinct roles of homologous proteins has still to be reached, although it has been speculated that LC3-like proteins are involved in early elongation steps during autophagosome formation, while GABARAP-like proteins are essential for autophagosome maturation (Weidberg et al., 2010).

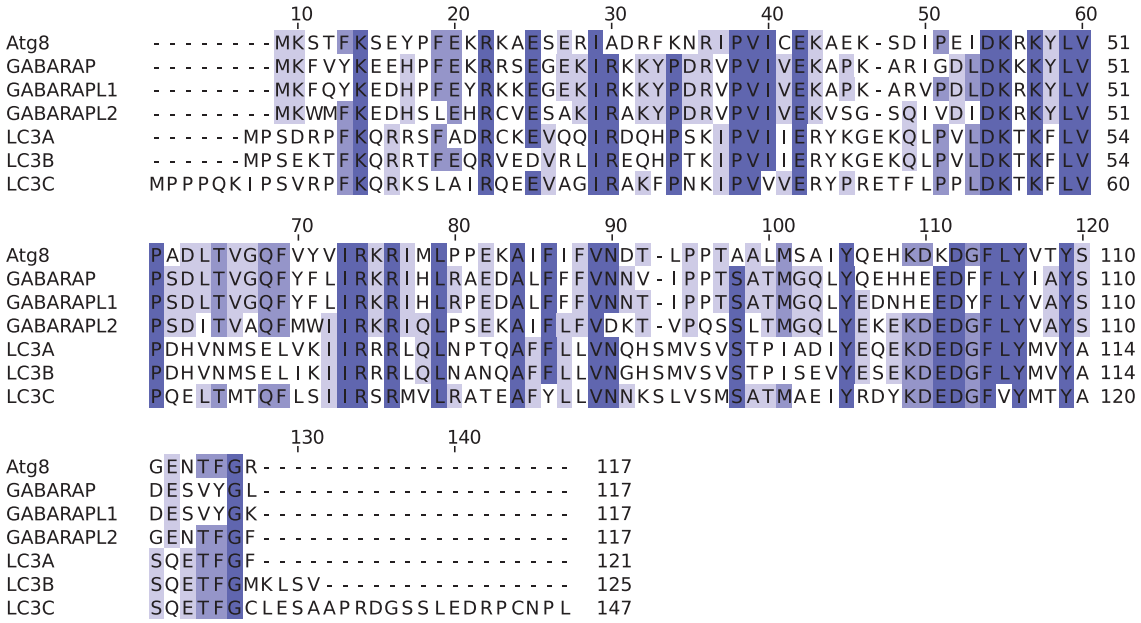

Figure 1.3.: Sequence alignment of *S. cerevisiae*'s Atg8 and the canonical human homologues GABARAP, GABARAPL1 (GEC1), GABARAPL2 (GATE-16), and LC3A, LC3B, and LC3C. Highly conserved residues are highlighted in shades of blue; darker shading indicates a higher conservation. Post-translational phosphorylation sites in LC3-like proteins have been described for LC3A (protein kinase A (PKA), S12), and LC3B (protein kinase C, T6 and T29). A possible PKA phosphorylation site in LC3C can be found with serine 18 (S18). In GABARAP-like proteins, however, no phosphorylation sites have been reported. Conserved residues important for structural stabilisation of amino-terminal helix $\alpha 2$ via salt-bridges can be found in the 110–112 region of all Atg8-like proteins.

The conjugation of an LC3-like protein to an emerging phagophore is essential for autophagosome genesis and membrane tethering (see also Figure 1.2 c) (Nakatogawa et al., 2007). LC3 is attached to prospective inner and outer autophagosomal membranes. While LC3-PE found on the inner membrane is degraded after autolysosome formation (Kirisako et al., 1999; Huang et al., 2000; Kabeya et al., 2000), LC3-PE on the outer autophagosomal membrane may be released back into the cytosol and recycled. Deconjugation of lipidated LC3 is also catalysed by ATG4 enzyme. Interestingly, the amount of Atg8-PE / LC3-PE adhering to an autophagosomal membrane influences the expansion of a phagophore and can control the size of a resulting autophagosome organelle (Ichimura et al., 2000; Nakatogawa et al., 2007; Xie et al., 2008). Following initiation of autophagy, LC3 expression is often upregulated in mammalian cells (Klionsky et al., 2007), and as LC3 is a vital component of the autopha-

gic pathway it consequently serves as *bona fide* marker for autophagy from initiation to degradation of cargo, a process known as autophagic flux (Kabeya et al., 2000; Mizushima et al., 2004; Bampton et al., 2005; Klionsky, 2008b; Mizushima et al., 2010).

Next to autophagosome genesis, LC3-like proteins are involved in membrane tethering *in vitro* (see also Figure 1.2 c), while mutational analyses have demonstrated LC3-like proteins are required for autophagosome formation *in vivo* (Nakatogawa et al., 2007). Additionally, LC3-like proteins are involved in axonal transport of autophagosomes in neurons through interaction of LC3 with the neuronal scaffolding protein JIP1 (Fu et al., 2014).

1.2.2. Structural Characteristics of LC3 Proteins

A decisive step forward in the effort to understand the molecular basis of autophagic conjugation mechanisms has been achieved by determination of the first three-dimensional structure of the mammalian Atg8-homologue GAPARAPL2, also known as GATE-16 or Golgi-associated ATPase enhancer of 16 kDa (Paz et al., 2000). Structural similarities between GABARAPL2 and ubiquitin were striking and underpinned the notion of Atg8-like proteins' mode of action being based on a conserved structural motif and not a catalytic phenomenon (Paz et al., 2000). Similar conclusions have later been made for other Atg8-like proteins: *Arabidopsis thaliana*'s Atg12 (Suzuki et al., 2005), *S. cerevisiae*'s Atg8 (Kumeta et al., 2010; Schwarten et al., 2010), and its mammalian homologues, namely GABARAP (Knight et al., 2002; Bavro et al., 2002; Stangler et al., 2002), GABARAPL1 (GEC1) (Rozenknop et al., 2011), and the LC3-family members LC3A (Suzuki et al., 2014), LC3B (Kouno et al., 2005; Ichimura et al., 2008; Noda et al., 2008), and LC3C (von Muhlinen et al., 2012; Suzuki et al., 2014).

Structurally, Atg8 and homologous proteins share a common ubiquitin-like fold. This fold is composed of two inner, parallel β-strands, each neighboured by one outer, antiparallel β-strand, thereby completing a central β-sheet, which in turn is flanked by two α-helices (see also Figure 1.4). This fold belongs to the $\alpha + \beta$ class and has been termed β-grasp due to an apparent grasp of a helix by a central β-sheet (Overington, 1992; Orengo et al., 1994; Murzin et al., 1995).

The β-grasp fold defines a versatile superfamily, found in a vast variety of func-

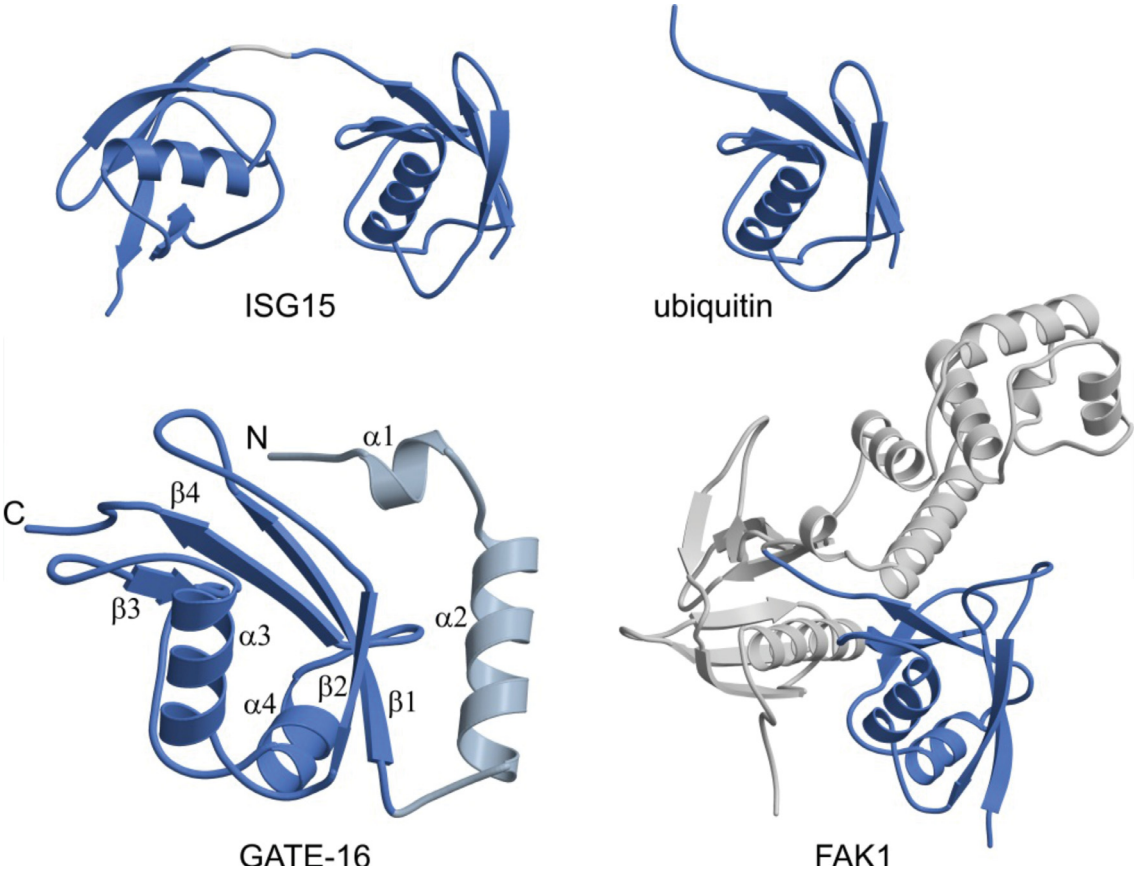

Figure 1.4.: Comparison of the conserved β-grasp fold (dark blue) found in a variety of protein families represented by respective crystal structures (Weiergräber et al., 2013). GATE-16 (PDB ID 1EO6) as a representative of the Atg8 family proteins, ubiquitin (PDB ID 1UBQ), ubiquitin-like ISG15 showing a β-grasp tandem (PDB ID 1Z2M), and β-grasp motif-containing FERM domain of the FAK1 protein (PDB ID 2AEH). Compared to ubiquitin, Atg8 homologues, like GATE-16, contain a specific N-terminal extension (light blue).

tionally different protein domains: for example in iron-sulfur binding-clusters, soluble ligand and Ras-binding domains, in the active site of phosphatidylinositol 3-kinase γ and as subdomain in other kinases (Paz et al., 2000; Burroughs et al., 2007a,b; Ceccarelli et al., 2006). The β-grasp is an apparently highly conserved protein fold, while amino acid composition and sequence in these examples are not. Therefore the β-grasp can be regarded as an illustration of conservation of protein structure in biological evolution (Shakhnovich et al., 2003; Goldstein, 2008; Ingles-Prieto et al., 2013; Weiergräber et al., 2013).

In proteins of the Atg8-family, the central β-grasp is usually referred to as carboxy-

terminal or ubiquitin-like domain and is sufficient for protein maturation and carboxy-terminal conjugation to the phospholipid PE (Shvets et al., 2008). However, a hallmark of Atg8 / LC3-like proteins are two additional amino-terminal α-helices complementing the β-grasp motif, addressed as amino-terminal extension, amino-terminal helical domain, or amino-terminal subdomain (see also Figure 1.4).

The amino-terminal domain is a defining feature of individual GABARAP- and LC3-family members. It is comprised of a long α-helix α2, and, often, a shorter helix α1 formed by anterior residues. Residues preceding α1 are then labelled amino-terminal region (ATR) and ordinarily show no regular secondary structure. Especially the short α1-helix and ATR are subject to an apparent structural heterogeneity in Atg8-like proteins. This is manifested in elevated B-factors in crystal structures, and / or broadened resonance signals found in NMR studies of Atg8-like proteins in solution.

For human GABARAP, for instance, two stable, distinct conformations of helix α1 and ATR relative to the remainder of the protein are reported. In the closed conformation, helix α1 and the ATR are in close contact with the carboxy-terminal domain, while in the open conformation the respective residues point towards the surrounding medium (Coyle et al., 2002). Initially, these conformations have been described for protein crystals obtained from different crystallisation conditions (Stangler et al., 2002). In solution, on the other hand, NMR line-broadening of several α1 and ATR residues have indicated an overall intrinsic conformational heterogeneity or dynamics on the slow micro- to millisecond timescale (Knight et al., 2002; Stangler et al., 2002). Analogous observations have been made for *S. cerevisiae* Atg8, where both amino-terminal helices are subject to conformational heterogeneity relative to the carboxy-terminal domain (Schwarten et al., 2010).

In contrast to Atg8, the longer amino-terminal α2-helix in mammalian LC3-like proteins remains in a restricted, stable conformation in immediate vicinity to the carboxy-terminal domain. This phenomenon is mediated by salt bridges between conserved residues of helix α2 and corresponding spatially close residues in the carboxy-terminal domain (see also Figures 1.3 and 1.4). Especially conserved residues of α2 (e.g. R22 or E25 in LC3C) are involved and interact with conserved residues of the carboxy-terminal domain (e.g. D110 to D112 in LC3C).

The exact role of the amino-terminal domain of Atg8-like proteins is still controversial and under debate. Amino-acid composition and sequence vary among Atg8-like proteins (see also Figure 1.3) and result in differing electrostatic surface potentials.

Furthermore, the amino-terminal domain may be involved in tubulin-binding activity. With GABARAP, for instance, residues influencing tubulin binding are found in the first 35 amino acids–encompassing helices α1 and α2 (Wang et al., 1999). Further studies pinpoint tubulin-binding activity to the first 22, mostly basic residues (Wang and Olsen, 2000). Otherwise, NMR titration experiments have not confirmed a specific interation between GABARAP and tubulin, yet (Knight et al., 2002).

The carboxy-terminal residues of most Atg8-like proteins are subject to conformational heterogeneity, as well. Whereas for GABARAP, as the exception to the rule, a direct contact of carboxy-terminus and amino-terminal residues and therefore compact fold has been reported (Stangler et al., 2002; Knight et al., 2002), GABARAPL1's carboxy-terminus, on the other hand, is not arranged in close vicinity to the amino-terminus (Rozenknop et al., 2011). The carboxy-terminus of GABARAPL2 adopts two conformations–one extended, one curved–, as observed in the two molecules in the asymmetric unit of GABARAPL2 crystals (Paz et al., 2000). This carboxy-terminal structural mobility has also been suggested by NMR data and molecular dynamics simulations and may assist in ATG4-binding during maturation of Atg8-like precursor proteins (Ma et al., 2015). Overall, the discussed conformational heterogeneity may as well be a result of a carboxy-terminal dynamics present in all Atg8-like proteins.

A defining structural hallmark of all Atg8-like proteins are two highly conserved hydrophobic binding pockets. These are essential for target interactions and are lined by residues of both subdomains. Here, the convex side of the central β-sheet and α2 (and to some extent α1) form the hydrophobic binding pocket one (also described as hp1 or W-site), while the concave face of the central β-sheet together with helix α3 shape the second hydrophobic binding pocket (hp2 or L-site). Other ubiquitin-like proteins lack equivalent hydrophobic binding pockets, thus rendering these a distinctive feature of Atg8-family proteins (Noda et al., 2008; Weiergräber et al., 2013).

1.2.3. The LC3-Interacting Region

In the last decades, the focus in autophagy research lay on components and mechanisms of bulk and thereby unspecific degradation of cytosolic targets. In recent times, however, it has become increasingly clear that autophagic pathways involve several selective routes, as well. This notion was sparked by the identification and characterisation of mammalian autophagy receptor proteins like the polyubiquitin binding

protein p62 (also known as sequestosome 1 or SQSTM1), NBR1 (neighbour of Brca1 (breast cancer 1, early onset) gene), or, lately, optineurin (Vadlamudi et al., 1996; Pankiv et al., 2007; Kirkin et al., 2009; Wild et al., 2011).

Autophagy receptors bind (poly-)ubiquitinated protein inclusions, organelles or pathogens via their ubiquitin-binding domain. Concurrently, these receptors and, indeed, all known LC3-binding proteins, bind LC3-like proteins through a short conserved, hydrophobic sequence termed LIR (LC3-interacting region), or AIM (Atg8-interacting motif) (Pankiv et al., 2007; Klionsky and Schulman, 2014). Initially identified as a 22-residue amino acid sequence in human p62/SQSTM1, subsequent studies have pinpointed the LIR motif to the four residue core sequence (W/Y/F)xx(L/I/V), often preceded by acidic residues (Pankiv et al., 2007; Ichimura et al., 2008; Noda et al., 2008; Alemu et al., 2012). Tryptophan is energetically favoured over tyrosine or phenylalanine in a LIR-sequence, although a lowered binding affinity–when tryptophan is replaced by tyrosine or phenylalanine–can be compensated for by preceding acidic residues (Alemu et al., 2012; Rogov et al., 2013). It is postulated that these acidic LIR residues are involved in electrostatic interactions with residues of the LC3-like protein. Here, two conserved lysine residues of the ubiquitin-like domain (K48/K50 in LC3A/B or K55/K57 in LC3C) have to be highlighted (Pankiv et al., 2007; Shvets et al., 2008; Rogov et al., 2013). Still, the aromatic amino acid of the LIR core motif has emerged as a clear necessity for LIR function (Alemu et al., 2012). The aromatic side-chain directly interacts with LC3-like protein's hydrophobic binding pocket one (hp1). The fourth (aliphatic) amino acid of the LIR core motif, on the other hand, associates with hydrophobic binding pocket two (hp2) (Ichimura et al., 2008; Noda et al., 2008). Interestingly, several proteins of the autophagic core machinery contain LIR motifs as well, and therefore are potentially able to recruit or associate with LC3-like proteins at different stages of autophagosome formation (Alemu et al., 2012).

The physical binding event to a LIR-sequence involves residues of the LC3-like protein's β2-strand. Here, the central β-sheet is augmented by an additional, parallel β-strand attaching to β2 through backbone hydrogen bonds.

Recently, a non-canonical three residue LIR motif (LVV), termed CLIR, has been identified with the xenophagy receptor NDP52 (nuclear domain 10 protein of 52 kDa), which specifically binds human LC3-like homologue LC3C (von Muhlinen et al., 2012). The CLIR motif lacks the aromatic residue typical of canoncial LIRs and binds LC3C's

hydrophobic pockets solely via its aliphatic LVV sequence. Furthermore, binding of the CLIR motif to LC3C results in the formation of an anti-parallel β-strand, which is reversed in comparison to canonical LIR binding. This study has described for the first time a distinctive and non-overlapping role for a mammalian LC3 homologue.

1.3. Regulation of Autophagy Through Post-Translational Modifications

A tight regulation of biochemical pathways is of prime importance for cellular homeostasis. On the one hand regulation can act on a transcriptional or translational level, directly affecting gene expression. On the other hand, post-synthetic or post-translational modifications allow to control activity of already expressed and available protein reserves. Hereby cells have the possibility of an immediate, fast response to cellular events. In most cases, post-translational modifications of proteins result in covalent attachment of a single or multiple chemical functional groups to side-chains.

Autophagic proteins of the Atg8 / LC3-family are known to be subject to four major post-translational modifications: proteolysis, lipidation, acetylation and phosphorylation (Xie et al., 2015). While proteolysis of Atg8 / LC3-like proteins occurs during maturation of their precursors, the lipidation by covalently attaching PE to carboxy-terminal glycine is the most crucial and essential function of Atg8 / LC3-like proteins. In recent years, however, post-translational control of autophagy through acetylation and phosphorylation came into focus.

Proteins are phosphorylated by transferring the γ-phosphate group of ATP to the hydroxyl oxygen of either serine, threonine, or tyrosine, and is catalysed by protein kinases. Most protein kinases can be assigned to one out of two major classes, which preferentially modify serine / threonine residues and tyrosine side-chains, respectively (Ubersax and Ferrell, 2007). Protein acetylation, on the other hand, is catalysed by acetyltransferases using acetyl coenzyme A as a cofactor. Here, acetyl-CoA's thioester bonded acetyl-group is transferred to a lysine ϵ-amino group (Verdin et al., 2015).

Interestingly, protein acetylation can be linked to cellular nutrient levels. As nutrients are depleted, the NAD^+ concentration is increased, which in turn activates sirtuin deacetylases decreasing acetylation levels of target proteins (Verdin et al.,

2015). Furthermore, through studies of mammalian cells, the influence of acetylation on starvation-induced autophagy has been investigated (Lee et al., 2008; Lee and Finkel, 2009). On a cellular level, artificially increasing expression levels of the deacetylase Sirt1 (sirtuin1), increases autophagic activity even in the presence of sufficent nutrients (Lee et al., 2008). On the other hand, knockdown of the acetyltransferase p300 reduces acetylation of several Atg proteins. Then again, increased expression of p300 results in inhibition of starvation-induced autophagy (Lee and Finkel, 2009). Recently, studies have been conducted on the translocation of nuclear LC3B into the cytoplasm of mammalian cells. Here, two lysine residues of LC3B (K49 and K51)–conserved among LC3-like proteins and key residues for LIR binding–are deacetylated under starvation conditions by Sirt1, followed by the translocation of LC3B into the cytoplasm during starvation induced autophagy. Furthermore, acetylation is predominantly found for LC3B-I and conjugation of LC3B to PE is influenced by acetylation (Huang et al., 2015). Since the aforementioned lysine residues are key residues of LIR binding, acetylation of these lysines (K49 and K51) may influence LC3B's ability to mediate protein-protein interactions.

Besides influencing autophagy by acetylation, the function of LC3-like proteins can be modulated by phosphorylation, as well. Through studies of mammalian LC3A, a conserved protein kinase A (PKA) phosphorylation site has been identified (Cherra et al., 2010). This phosphorylation site is not present in GABARAP-like proteins and may be a key difference between the GABARAP-like and LC3-like protein families. The presumed target of PKA phosphorylation in LC3-like proteins is a conserved serine or threonine residue–found with LC3A at position 12 and with LC3C at position 18 (see also Figure 1.3).

Through phosphorylation of LC3A, induction of autophagy by effector substances is down-regulated (Cherra et al., 2010). Conversely, phosphorylated LC3A (phospho-LC3A) is dephosphorylated during autophagy induction and subsequently increasingly recruited into autophagosomes (Cherra et al., 2010). Membrane fusion events, mediated by LC3-like proteins, are dependent on their amino-terminal residues. The addition of a bulky, negatively charged phosphate group may thus influence subsequent interactions depending on electrostatic interactions (Sugawara et al., 2004). It is therefore speculated that phosphorylated LC3-like proteins may provide an inactive pool, ready to be mobilised in response to autophagic stimuli (Cherra et al., 2010). In addition, and especially with regard to LC3-like proteins, a phosphorylation of tar-

get residues within amino-terminal α-helix 2 may introduce a dramatic change in the helix' polarity and thereby decisively influence the protein's function.

Nearly simultaneously to PKA studies by Cherra et al. (2010), phosphorylation of LC3B by protein kinase C (PKC) has been reported (Jiang et al., 2010). Here, two threonine residues (T6 and T29), both found in the amino-terminal domain, as well, have been identified as *in vitro* PKC phosphorylation sites (see also Figure 1.3). Furthermore, it has been postulated that PKC inhibitors induce lipidation of LC3B and increase autophagosome formation, while the effect of PKC activators is the contrary. Although *in vivo* studies with phospho-mimicking point mutations of LC3B have been conducted (T6D/Q and / or T29D/Q), a clear role of LC3B phosphorylation by PKC could not be confirmed and overlapping functionality of LC3- and GABARAP-like proteins may have obscured this study (Jiang et al., 2010).

In addition to the influence of post-translational modifications on LC3-like protein's amino-terminal domain, consequences of post-translational LIR sequence modification has also been investigated. Especially optineurin, an autophagy receptor involved in *Salmonella enterica* clearance, came into focus (Wild et al., 2011). Here, the core LIR sequence is neighboured upstream by a modifiable serine residue, whose phosphorylation directly influences cargo-selective autophagy.

By these examples, it seems likely that LC3-like lipidation systems are modulated by post-translational modifications. Further structural studies would allow to decipher key atomic details of the action of these modifications and in turn create the possibility to selectively target LC3-like proteins in a cellular environment.

2. Aims

Autophagy depends on at least two distinct protein conjugation systems. One of these systems attaches ubiquitin-like modifiers to expanding autophagosomal membranes, which sequester cargo destined for autophagic degradation. These autophagosomal ubiquitin-like modifiers are members of the Atg8 (autophagy-related 8) protein family, the function of which has been first described for the yeast *Saccharomyces cerevisiae*. In human cells, however, Atg8 has diversified into the GABARAP-like and LC3-like protein subfamilies. The lastly discovered member of the LC3-like subfamily, LC3C, is the least well characterised and unique in regard to overall number of amino acids, length of the carboxy-terminal propeptide removed during maturation, and length of the functionally uncharacterised amino-terminal region of the mature, cytosolic protein.

The foremost aim of this thesis is therefore to determine a high-quality structural model of LC3C by liquid-state nuclear magnetic resonance (NMR) spectroscopy. Commonly, biomolecular NMR studies require high amounts of pure and stable protein. For this reason, LC3C's gene has to be cloned, and protein expression and purification schemes have to be developed. Furthermore, purified LC3C samples have to be concentrated and NMR buffer and data acquisition conditions optimised. Assignment of LC3C's backbone and side-chain resonances from heteronuclear, triple resonance experiments form the foundation to generate a high-quality NMR structural model and is therefore an essential part of this work. Distance information for structure calculations will be deduced from NOESY (nuclear Overhauser effect spectroscopy) data. And finally, LC3C's structural dynamics will be analysed on multiple time scales.

Post-translational modification by phosphorylation of LC3-like proteins LC3A and LC3B by protein kinases is discussed as a potential determinant of their cell biological activity. In this thesis, the structural biology of LC3C phosphorylation by protein kinase A (PKA) should be investigated. For this purpose, an *in-vitro* phosphorylation scheme

for LC3C has to be developed. Additionally, the progress of LC3C phosphorylation by PKA and its effects on backbone resonance signals should be traced and interpreted using NMR spectroscopy.

3. Scientific Publications

The following peer-reviewed scientific articles have emerged from this work.

- **Sequence-specific ^{1}H, ^{15}N, and ^{13}C resonance assignments of the autophagy-related protein LC3C**
  Carsten Krichel, Oliver H. Weiergräber, Marina Pavlidou, Jeannine Mohrlüder, Melanie Schwarten, Dieter Willbold, Philipp Neudecker
  Biomol NMR Assign. 2016 Apr;10(1):41-3. doi: 10.1007/s12104-015-9633-z. Impact factor 0.76 (2015)

  Own contribution: Design and execution of cloning, expression and purification experiments. Realisation of NMR experiments, data evaluation and interpretation. Wrote manuscript (95%).

- **Solution Structure of the Autophagy-related Protein LC3C Reveals a Polyproline II Motif on a Mobile Tether with Phosphorylation Site**
  Carsten Krichel, Christina Möller, Oliver Schillinger, Pitter F. Huesgen, Heinrich Sticht, Birgit Strodel, Oliver H. Weiergräber, Dieter Willbold, and Philipp Neudecker

  Own contribution: Conceived and designed experiments, produced samples, performed NMR and phosphorylation experiments. Analysed and interpreted data resulting in protein structure determination, observation and interpretation of phosphorylation reaction by NMR. Wrote manuscript draft.

3.1. Reference 1

Sequence-specific ^{1}H, ^{15}N, and ^{13}C resonance assignments of the autophagy-related protein LC3C

Carsten Krichel, Oliver H. Weiergräber, Marina Pavlidou, Jeannine Mohrlüder, Melanie Schwarten, Dieter Willbold, Philipp Neudecker

Biomol NMR Assign. 2016 Apr;10(1):41-3. doi: 10.1007/s12104-015-9633-z.

Biomol NMR Assign (2016) 10:41–43
DOI 10.1007/s12104-015-9633-z

ARTICLE

Sequence-specific ^{1}H, ^{15}N, and ^{13}C resonance assignments of the autophagy-related protein LC3C

Carsten Krichel[1,2] · Oliver H. Weiergräber[1] · Marina Pavlidou[1] · Jeannine Mohrlüder[1] · Melanie Schwarten[1] · Dieter Willbold[1,2] · Philipp Neudecker[1,2]

Received: 15 July 2015 / Accepted: 11 August 2015 / Published online: 18 August 2015

Abstract Autophagy is a versatile catabolic pathway for lysosomal degradation of cytoplasmic material. While the phenomenological and molecular characteristics of autophagic non-selective (bulk) decomposition have been investigated for decades, the focus of interest is increasingly shifting towards the selective mechanisms of autophagy. Both, selective as well as bulk autophagy critically depend on ubiquitin-like modifiers belonging to the Atg8 (autophagy-related 8) protein family. During evolution, Atg8 has diversified into eight different human genes. While all human homologues participate in the formation of autophagosomal membrane compartments, microtubule-associated protein light chain 3C (LC3C) additionally plays a unique role in selective autophagic clearance of intracellular pathogens (xenophagy), which relies on specific protein–protein recognition events mediated by conserved motifs. The sequence-specific ^{1}H, ^{15}N, and ^{13}C resonance assignments presented here form the stepping stone to investigate the high-resolution structure and dynamics of LC3C and to delineate LC3C's complex network of molecular interactions with the autophagic machinery by NMR spectroscopy.

Keywords Heteronuclear NMR · Sequence-specific resonance assignments · Microtubule-associated protein light chain 3C · MAP1LC3C · LC3C · Autophagy

✉ Philipp Neudecker
p.neudecker@fz-juelich.de

[1] Institute of Complex Systems, ICS-6: Structural Biochemistry, Forschungszentrum Jülich, 52425 Jülich, Germany

[2] Institut für Physikalische Biologie und BMFZ, Heinrich-Heine-Universität Düsseldorf, 40225 Düsseldorf, Germany

Biological context

Microtubule-associated protein light chain 3C (MAP1LC3C or simply LC3C) is a member of the Atg8 protein family involved in macroautophagy (Shpilka et al. 2011). In humans, the Atg8-family includes eight genes (Weiergräber et al. 2013), coding for proteins divided into two subfamilies: the GABARAP-like and the MAP1LC3-like proteins. LC3C shares significant sequence identity with MAP1LC3-subfamily (LC3A 59 %, LC3B 55 %) and GABARAP-subfamily proteins (GABARAP 40 %, GABARAPL1 39 %, GABARAPL2 43 %) alike, with the largest sequence differences found in the amino-terminal region. The functional role of this diversification is still poorly understood and could not be related to structural properties to date. Interestingly, only minor variations in the hydrophobic leucine recognition pocket of LC3C in comparison to LC3A and LC3B are a key determinant of LC3C's unique role in xenophagy (Noda et al. 2010; von Muhlinen et al. 2012). Chemical shift assignments and solution structures of Atg8-like proteins are known for mammalian GABARAP (Stangler et al. 2002), GABARAPL1 (Rozenknop et al. 2011), for LC3-like proteins LC3A (Kouno et al. 2005), LC3B (Rogov et al. 2013), and for yeast Atg8 (Schwarten et al. 2010; Kumeta et al. 2010).

As a crucial first step in the investigation of the structure, dynamics, and molecular interactions of LC3C by NMR spectroscopy, we report the sequence-specific ^{1}H, ^{15}N, and ^{13}C resonance assignments.

Methods and experiments

Protein expression and purification

In vivo, LC3C is expressed as a 147-residue protein, which is subsequently cleaved by ATG4B to yield the mature

cytosolic LC3C protein of 126 amino acids (He et al. 2003). For in vitro studies, an *E. coli* codon optimised LC3C gene coding for the full-length human protein was synthesised (GeneArt, Regensburg, Germany; now Thermo Scientific) according to Uniprot accession number Q9BXW4 with additional BamH1 and NotI restriction sites. The gene was cloned into a pGEX-4T-2 bacterial expression vector resulting in an amino-terminal GST-LC3C fusion protein. Two stop codons were introduced with the QuikChange XL II kit (Stratagene, Waldbronn, Germany) to obtain the coding sequence for the mature LC3C of 126 amino acids, and expression was optimised in *E. coli* Rosetta2 (DE3) cells. The cells were grown in selective LB medium containing ampicillin and chloramphenicol (100 and 34 µg/ml, respectively) at 37 °C to an OD_{600} of 0.6, harvested by centrifugation (4000×*g*, 20 min) and resuspended in isotopically labelled, selective M9 medium (0.5 g/l $^{15}NH_4Cl$ and/or 2 g/l glucose-$^{13}C_6$). The culture was then grown in M9 medium at 37 °C until it reached an OD_{600} of 1.0, then equilibrated at 25 °C and 200 rpm for 0.5 h. Protein expression was induced by adding IPTG to a final concentration of 1.0 mM and continued at 25 °C for 5 h. Cells were harvested by centrifugation as before, resuspended in cell lysis buffer (tris-buffered saline (TBS: 137 mM NaCl, 2.7 mM KCl, 19.0 mM Tris-HCl), 5 % (v/v) glycerol, 5 mM 2-mercaptoethanol, 20 µg/ml DNAse1, 0.1 % (v/v) Triton X-100, complete EDTA-free protease inhibitor cocktail (Roche, Mannheim, Germany), pH 9.0) and lysed by cell disruption (1.7 kbar, 10 °C). Cell lysate containing soluble GST-LC3C fusion protein was cleared by centrifugation (50000×*g* at 12 °C for 45 min) and loaded onto equilibrated (TBS, 5 % (v/v) glycerol, 1 mM 2-mercaptoethanol, 5 mM EDTA, 0.01 % (v/v) Triton X-100, pH 8.0) GSH-Sepharose and the slurry incubated over night at 6 °C under mild agitation. GSH-Sepharose bound GST-LC3C fusion protein was washed (TBS, 5 % (v/v) glycerol, 0.01 % (v/v) Triton X-100, pH 8.0) and 40 µg bovine thrombin (Merck, Darmstadt, Germany) per ml slurry added. The thrombin hydrolysis reaction was completed at room temperature within 1 h and leads to GST-free LC3C with a two amino acid amino-terminal cloning artefact (Gly-1 and Ser0). Buffer containing free LC3C was eluted by gravity flow, and dialysed overnight (Spectra Por, 1000 Da, Spectrumlabs, Frankfurt, Germany) in 6 °C pre-chilled buffer (20 mM PIPES, 50 mM NaCl, 0.5 % (v/v) glycerol, pH 6.0). Further purification steps included cation exchange chromatography (Resource S 1 ml, GE Healthcare, Freiburg, Germany) and a final purification and buffer exchange step in NMR buffer (20 mM PIPES, 150 mM NaCl, 0.1 mM EDTA, pH 6.0) by size exclusion chromatography (Superdex 75, 16/60, GE Healthcare, Freiburg, Germany). Fractions containing LC3C were pooled and concentrated at 6 °C with an Amicon stirred cell (1000 Da nominal molecular weight limit (NMWL), regenerated cellulose membrane, Millipore, Schwalbach, Germany) and Amicon Ultra 0.5 ml spin columns (3000 Da NMWL, Millipore, Schwalbach, Germany) at 8000×*g* and 10 °C in a refrigerated benchtop centrifuge. Concentrated samples were supplemented with 2 % (v/v) glycerol-d_8 (Euriso-top, Gif-sur-Yvette, France) and 10 % (v/v) D_2O. NMR samples contained between 370 and 570 µM LC3C protein.

NMR spectroscopy

NMR experiments were recorded at 20.0 °C on Varian INOVA or Bruker AVANCE III spectrometers with cryogenically cooled triple or quadruple resonance probes with pulse-field gradient capabilities operating at a ^1H frequency of 600 MHz. ^1H chemical shifts were referenced to an external DSS sample, ^{13}C and ^{15}N chemical shifts were referenced indirectly using frequency ratios (Cavanagh et al. 2007). The sequence-specific assignment of backbone resonances was accomplished by using [^1H-^{15}N] HSQC, HNCA, HNCACB, CBCA(CO)NH, and C(CO)NH experiments (Sattler et al. 1999; Cavanagh et al. 2007). Carbonyl chemical shifts were derived from an HNCO experiment. Side-chain resonances were assigned using [^1H–^{13}C] ct-HSQC, HNHA, [^1H–^{15}N] TOCSY–HSQC, HBHA(CO)NH, H(CCO)NH, (H)CCH–COSY, H(C)CH–COSY, HC(C)H–TOCSY (Kovacs and Gossert 2014), 2D [^1H–^1H] TOCSY, [^1H–^{15}N] NOESY–HSQC (120 ms mixing time), [^1H–^{13}C] NOESY–HSQC (120 ms mixing time), 3D [^1H–^{15}N] [^1H–^{15}N] HSQC–NOESY–HSQC (150 ms mixing time), and 3D [^1H–^{13}C] [^1H–^{15}N] HSQC–NOESY–HSQC (150 ms mixing time) spectra (Sattler et al. 1999; Cavanagh et al. 2007). Resonance assignments of the aromatic side-chains were obtained from the HC(C)H–TOCSY (Kovacs and Gossert 2014), [^1H–^{15}N] NOESY–HSQC, and [^1H–^{13}C] NOESY-HSQC experiments. NMR data were processed using NMRPipe and NMRDraw (Delaglio et al. 1995). Assignment was accomplished with NMRView (One Moon Scientific, Inc.) and CcpNmr Analysis (Vranken et al. 2005). $^3J_{HNH\alpha}$ scalar coupling constants were calculated in CcpNmr Analysis from a quantitative HNHA experiment with a coherence transfer time of 12.3 ms, using a relaxation correction factor of 1.10 (Cavanagh et al. 2007).

Assignments and data deposition

Analysis of the backbone assignment experiments allowed sequence-specific resonance assignments of 115 of the 117 backbone amide groups (98 %), as shown in Fig. 1. Inspection of the NMR spectra and preliminary analysis of

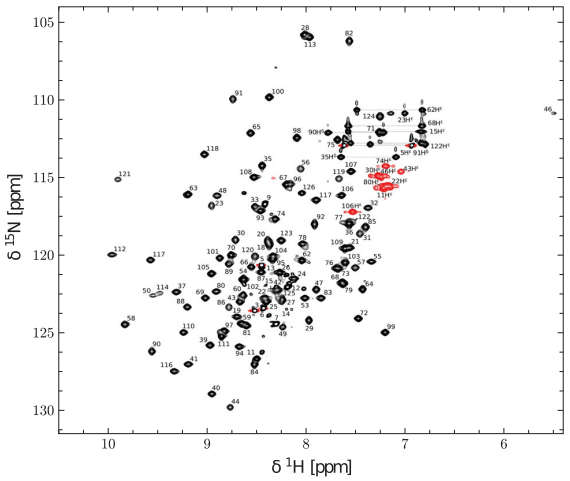

Fig. 1 [^{1}H–^{15}N] HSQC spectrum of 560 μM [*U*–^{15}N] LC3C in NMR buffer (20 mM PIPES, 150 mM NaCl, 0.1 mM EDTA, 2 % (v/v) glycerol-d_8, pH 6.0) recorded at 20.0 °C and 600 MHz. Backbone resonance assignments are indicated by *residue numbers*. Side-chain resonances of Asn and Gln residues are connected by *horizontal lines*, amine side-chain resonances of Arg are aliased in the ^{15}N dimension and shown in *red*. Backbone resonances of Arg16 and Lys17 could not be identified due to severe exchange line broadening

^{15}N relaxation and relaxation dispersion experiments reveal the presence of exchange line broadening due to conformational heterogeneity, which seems to be a common feature of the Atg8 protein family (Schwarten et al. 2010; Weiergräber et al. 2013) and hampered resonance assignment in some regions of LC3C. Accordingly, the backbone amide resonances of Arg16 and Lys17 could not be assigned. Note that the backbone amide proton of Arg46 exhibits a strong upfield shift (5.50 ppm), most likely due to ring current effects from the aromatic side-chain of Tyr44 in the vicinity. In total, side-chain assignments were obtained for 96 % of the protons, 90 % of the carbons, and 89 % of the nitrogens. 99 % of the $^{13}C\alpha$ and $^{1}H\alpha$ resonances could be assigned. The chemical shifts of the Pro2 $^{1}H\delta$, Pro3 $^{1}H\gamma$, $^{1}H\delta$, and Pro45 $^{1}H\delta$ methylene groups could not be assigned due to spectral overlap. Assigned chemical shifts and $^{3}J_{HNH\alpha}$ coupling constants have been deposited with the Biological Magnetic Resonance Data Bank under accession code 26603.

References

Cavanagh J, Fairbrother WJ, Palmer AG, Rance M, Skelton NJ (2007) Protein NMR spectroscopy, 2nd edn. Elsevier Academic Press, Burlington

Delaglio F, Grzesiek S, Vuister GW, Zhu G, Pfeifer J, Bax A (1995) NMRPipe: a multidimensional spectral processing system based on UNIX pipes. J Biomol NMR 6:277–293

He H, Dang Y, Dai F, Guo Z, Wu J, She X, Pei Y, Chen Y, Ling W, Wu C, Zhao S, Liu JO, Yu L (2003) Post-translational modifications of three members of the human MAP1LC3 family and detection of a novel type of modification for MAP1LC3B. J Biol Chem 278:29278–29287

Kouno T, Mizuguchi M, Tanida I, Ueno T, Kanematsu T, Mori Y, Shinoda H, Hirata M, Kominami E, Kawano K (2005) Solution structure of microtubule-associated protein light chain 3 and identification of its functional subdomains. J Biol Chem 280:24610–24617

Kovacs H, Gossert A (2014) Improved NMR experiments with ^{13}C-isotropic mixing for assignment of aromatic and aliphatic side chains in labeled proteins. J Biomol NMR 58:101–112

Kumeta H, Watanabe M, Nakatogawa H, Yamaguchi M, Ogura K, Adachi W, Fujioka Y, Noda NN, Ohsumi Y, Inagaki F (2010) The NMR structure of the autophagy-related protein Atg8. J Biomol NMR 47:237–241

Noda NN, Ohsumi Y, Inagaki F (2010) Atg8-family interacting motif crucial for selective autophagy. FEBS Lett 584:1379–1385

Rogov VV, Suzuki H, Fiskin E, Wild P, Kniss A, Rozenknop A, Kato R, Kawasaki M, McEwan DG, Löhr F, Güntert P, Dikic I, Wakatsuki S, Dötsch V (2013) Structural basis for phosphorylation-triggered autophagic clearance of *Salmonella*. Biochem J 454:459–466

Rozenknop A, Rogov VV, Rogova NY, Löhr F, Güntert P, Dikic I, Dötsch V (2011) Characterization of the interaction of GABARAPL-1 with the LIR motif of NBR1. J Mol Biol 410:477–487

Sattler M, Schleucher J, Griesinger C (1999) Heteronuclear multidimensional NMR experiments for the structure determination of proteins in solution employing pulsed field gradients. Prog Nucl Magn Reson Spectrosc 34:93–158

Schwarten M, Stoldt M, Mohrlüder J, Willbold D (2010) Solution structure of Atg8 reveals conformational polymorphism of the N-terminal domain. Biochem Biophys Res Commun 395:426–431

Shpilka T, Weidberg H, Pietrokovski S, Elazar Z (2011) Atg8: an autophagy-related ubiquitin-like protein family. Genome Biol 12:226

Stangler T, Mayr LM, Willbold D (2002) Solution structure of human $GABA_A$ receptor-associated protein GABARAP: implications for biological function and its regulation. J Biol Chem 277:13363–13366

von Muhlinen N, Akutsu M, Ravenhill BJ, Foeglein A, Bloor S, Rutherford TJ, Freund SMV, Komander D, Randow F (2012) LC3C, bound selectively by a noncanonical LIR motif in NDP52, is required for antibacterial autophagy. Mol Cell 48:329–342

Vranken WF, Boucher W, Stevens TJ, Fogh RH, Pajon A, Llinas M, Ulrich EL, Markley JL, Ionides J, Laue ED (2005) The CCPN data model for NMR spectroscopy: development of a software pipeline. Proteins 59:687–696

Weiergräber OH, Mohrlüder J, Willbold D (2013) Atg8 family proteins—autophagy and beyond. In: Bailly Y (ed) Autophagy—a double-edged sword—cell survival or death? InTech, Rijeka, pp 13–45. doi:10.5772/55647

3.2. Reference 2

Solution Structure of the Autophagy-related Protein LC3C Reveals a Polyproline II Motif on a Mobile Tether with Phosphorylation Site

Carsten Krichel, Christina Möller, Oliver Schillinger, Pitter F. Huesgen, Heinrich Sticht, Birgit Strodel, Oliver H. Weiergräber, Dieter Willbold, and Philipp Neudecker

Manuscript in submission.

Solution Structure of the Autophagy-related Protein LC3C Reveals a Polyproline II Motif on a Mobile Tether with Phosphorylation Site

Carsten Krichel[1,2], Christina Möller[1,2], Oliver Schillinger[1,3], Pitter F. Huesgen[4], Heinrich Sticht[5], Birgit Strodel[1,3], Oliver H. Weiergräber[1], Dieter Willbold[1,2,*], and Philipp Neudecker[1,2,*]

From the [1]ICS-6 (Strukturbiochemie), Forschungszentrum Jülich, 52425 Jülich, Germany, [2]Institut für Physikalische Biologie and BMFZ, Heinrich-Heine-Universität Düsseldorf, 40225 Düsseldorf, Germany, [3]Institut für Theoretische Chemie und Computerchemie, Heinrich-Heine-Universität Düsseldorf, 40225 Düsseldorf, Germany, [4]ZEA-3 (Analytik), Forschungszentrum Jülich, 52425 Jülich, Germany, and the [5]Institut für Biochemie, Friedrich-Alexander-Universität Erlangen-Nürnberg, 91054 Erlangen, Germany

Running title: *Solution Structure of the Autophagy-related Protein LC3C*

* To whom correspondence should be addressed: Prof. Dieter Willbold, ICS-6 (Strukturbiochemie), Forschungszentrum Jülich, 52425 Jülich, Germany, Telephone: +49 (2461) 61-2100; Fax: +49 (2461) 61-2023; E-mail: d.willbold@fz-juelich.de; Dr. Philipp Neudecker, ICS-6 (Strukturbiochemie), Forschungszentrum Jülich, 52425 Jülich, Germany, Telephone: +49 (2461) 61-9487; Fax: +49 (2461) 61-2023; E-mail: p.neudecker@fz-juelich.de

Keywords: autophagy, microtubule-associated protein (MAP), nuclear magnetic resonance (NMR), protein dynamic, protein kinase A (PKA), protein phosphorylation, protein structure

ABSTRACT

(Macro-)autophagy is a compartmental degradation pathway conserved from yeast to mammals. In *S. cerevisiae* the protein Atg8 mediates membrane tethering/hemifusion and cargo recruitment and is essential for autophagy. In humans, these roles are assumed by the MAP1LC3/GABARAP family of proteins, which show high sequence identity with each other and with Atg8 but considerable variation in their amino-terminal region. MAP1LC3C, in particular, has a conspicuous amino-terminal extension that is absent in the other family members and whose structural and functional role remains unclear. We have determined the high-resolution three-dimensional structure and measured the backbone dynamics of MAP1LC3C by NMR spectroscopy. From Ser18 to Ala120, MAP1LC3C forms an α-helix followed by the ubiquitin-like tertiary fold with two hydrophobic binding pockets used by MAP1LC3/GABARAP proteins to recognize targets presenting LC3-interacting regions (LIRs). The C-terminal Gly126 is mobile and accessible for anchoring to autophagosomal membranes. Unlike other MAP1LC3/GABARAP proteins, the amino-terminal region of MAP1LC3C does not form a stable helix α_1 but a "sticky arm" consisting of a polyproline II motif on a flexible linker. Ser18 at the interface between this linker and the structural core can be phosphorylated *in vitro* by protein kinase A (PKA), which causes additional conformational heterogeneity as monitored by NMR spectroscopy and molecular dynamics simulations, including changes in the LIR-binding interface. Based on these results we propose that the amino-terminal polyproline II motif mediates specific interactions with the microtubule cytoskeleton and that phosphorylation by PKA modulates the interplay of MAP1LC3C with its LIR-presenting target proteins and with the cytoskeleton.

INTRODUCTION

Macroautophagy - hereafter termed autophagy - is an intracellular lysosomal degradation pathway conserved in eukaryotes (1). Upon initiation of autophagy a newly emerging double membrane structure, the phagophore, engulfs cytoplasmatic targets and closes to form a double membrane vesicle, the autophagosome, which then fuses with lysosomal organelles for cargo degradation. The protein Atg8 (autophagy-related 8) is essential for autophagosome genesis in the yeast *Saccharomyces cerevisiae* (2). The carboxy-terminal residue of Atg8, Arg117 (Fig. 1),

is removed by the *S. cerevisiae* cysteine protease Atg4 to expose a conserved glycine, Gly116, at the C-terminus. Subsequently, this exposed glycine can enzymatically be conjugated covalently to the membrane lipid phosphatidylethanolamine and thereby tethered to the growing phagophore (3).

In humans, the Atg8 gene has diversified into at least eight orthologs, which can be divided into two subfamilies: the GABARAP (γ-aminobutyric acid type A receptor associated protein)-like and MAP1LC3 (microtubule associated proteins 1 light chain 3)-like proteins (4,5). The functional role of this diversification is still poorly understood. Like Atg8, these proteins are initially expressed as longer precursor proteins and then cleaved by the *H. sapiens* ATG4 family of cysteine proteases to expose the conserved glycine (Gly126 in the case of MAP1LC3C; Fig. 1) at the C-terminus. The high-resolution three-dimensional structure of several of these proteins has been determined experimentally by X-ray crystallography and/or NMR spectroscopy (reviewed in ref. 5). In particular, solution structures have been reported for yeast Atg8 (6-8), for the human GABARAP-like proteins GABARAP (9) and GABARAPL1 (10), and for the MAP1LC3-like proteins MAP1LC3A (11), MAP1LC3A in complex with SQSTM1 (12), and MAP1LC3B in complex with optineurin (13). Recently, crystal structures for MAP1LC3C in the free form (14; PDB 3WAM) as well as in complex with Atg13 (14; PDB 3WAP) and in complex with NDP52 (15; PDB 3VVW) were published. All these Atg8 homologs share a ubiquitin-like core structural motif consisting of a four-stranded β-sheet flanked by two α-helices, which is extended by an amino-terminal α-helical domain. The human MAP1LC3 (or simply LC3) proteins differ most significantly in the amino-terminal region (NTR) preceding this α-helical domain, which is considerably longer in LC3C as compared to LC3A and LC3B (Fig. 1). While for the latter two proteins a role of the NTR in membrane tethering (2,16) or in recognition of mitochondrial phospholipids during mitophagy has been reported (17), the functional implications of the longer NTR found in LC3C are still poorly understood.

Autophagy research has historically focused on unspecific (bulk) degradation of cytosolic targets. Recently, however, mammalian autophagy receptor proteins have been described that mediate selective autophagic pathways (18,19). Recruitment of selective autophagic degradation targets to LC3-like proteins is mediated by the target's conserved LC3-interacting region (LIR) of four amino acids with a canonical sequence motif (W/Y/F-x-x-L/I/V) (12,18,20). In contrast to other LC3 proteins, LIR binding to LC3C in selective autophagy can also be mediated by a non-canonical LIR motif (CLIR) (15). Upon binding to LC3 the two large hydrophobic side chains flanking the LIR of the target insert into two hydrophobic pockets on the surface of LC3 and the backbone of the LIR forms an additional, parallel β-strand to extend the core LC3 β-sheet separating the two hydrophobic pockets (12).

Autophagy is regulated by a variety of mechanisms, including the modulation of LC3 protein-protein interactions via post-translational modifications. On the one hand, the affinity of binding to LC3 can be enhanced by modification of the target LIR (19,21). On the other hand, post-translational modifications of the LC3 proteins themselves have been described. Intriguingly, the post-translational modification sites are predominantly localized within the NTR of LC3. Cherra et al. (22) reported the down-regulation of autophagy upon phosphorylation of LC3A at Ser12 by protein kinase A (PKA), while Jiang et al. (23) studied the influence of phosphorylation of LC3B at Thr6 and Thr26 by protein kinase C (PKC) on autophagosome formation. Both studies concluded that an increased cellular protein kinase activity could attenuate autophagy. Structural studies, however, were beyond the scope of these works. LC3C shares the PKA phosphorylation site mentioned above (Ser18 in this case) with LC3A and LC3B (22), and, unlike other LC3-proteins, contains a second PKC phosphorylation site at Ser9 as predicted by computational algorithms (24). Furthermore, Huang et al. (25) reported the influence of de-acetylation of a lysine residue in nuclear-localized LC3, suggesting further modulating options for LC3 activity in its interplay with the autophagic machinery. Other diverse post-translational modifications of autophagy-related proteins have been reviewed recently (26).

In order to provide a structural basis for understanding the functional role of the NTR of

LC3C on the atomic level we have determined the three-dimensional structure of human MAP1LC3C directly in solution and investigated the backbone dynamics and the influence of *in vitro* phosphorylation by PKA using NMR spectroscopy.

RESULTS AND DISCUSSION

Description of the Structure in Solution– As reported previously (27), inspection of the NMR spectra and analysis of the ^{15}N relaxation and relaxation dispersion experiments (see below) reveal that LC3C exhibits extensive conformational heterogeneity in several regions of the protein, which results in significant conformational averaging and/or exchange line broadening of the NMR spectra. Accordingly, manual inspection of the experimental restraints was necessary to exclude artificially restrictive restraints derived from conformationally averaged spectral parameters such as NOEs or $^{3}J_{HNH\alpha}$ couplings. An ensemble of ten solution structures was calculated from 1162 NOE distance restraints, 214 dihedral angle restraints, and 102 hydrogen bond distance restraints. Of note, all three α-helices feature a slowly exchanging backbone amide hydrogen donor involved in N-capping hydrogen bonds to side chain oxygen atoms (α_2: Ile21 HN – Ser18 Oγ; α_3: Gln68 HN – Thr65 Oγ1; α_4: Glu103 HN – Thr100 Oγ1). Experimental restraints and statistics of the structural ensemble are summarized in Table 1.

The overall structure of LC3C features a globular, ubiquitin-like fold consisting of four β-strands, three α-helices, and polymorphic terminal regions (see Fig. 2). The core of LC3C is formed by a twisted, mixed parallel/antiparallel β-sheet consisting of two inner β-strands (β_1, β_4) pairing in a parallel orientation, each paired by an antiparallel β-strand (β_2 and β_3, respectively) on the outside. The three α-helices α_2, α_3, and α_4 (this numbering has been chosen for consistency with other members of the Atg8 family that have an additional α-helix at the N-terminus) are flanking the inner β-sheet on both faces, with helix α_3 in an orientation that is approximately perpendicular to that of α_2 and α_4. It is this arrangement of the regular secondary structure elements that forms the two characteristic hydrophobic surface pockets, hp1 between α_2 and β_2 on one face of the β-sheet and hp2 between α_3 and β_2 on the other face (Fig. 2), which allow Atg8 family proteins to bind canonical or non-canonical LC3-interacting regions (LIRs) via β-strand pairing of the LIR backbone to the edge strand β_2 while accommodating the two bulky hydrophobic side-chains of the LIR in hp1 and hp2 (12). The side-chain of Lys55, which is located just N-terminal of strand β_2 and has been reported to restrict access to hp2 in order to contribute to LIR recognition (14), is partially solvent-exposed in solution and sufficiently flexible across the ensemble of structures to allow the formation of a complex with a specifically recognized ligand (not shown).

The tertiary structure of LC3C is stabilized not just by hydrogen bonds but also by a variety of hydrophobic interactions involving aliphatic and aromatic side-chains. Tertiary contacts with aromatic side-chains give rise to several readily identifiable ^{1}H chemical shift outliers due to ring current effects. Most notably, the backbone amide proton of Arg46 displays a remarkable upfield shift (5.50 ppm), which is caused by the vicinity to the aromatic side-chain of Tyr44 and has been reported previously (27). Unfortunately, this chemical shift is too close to the residual $^{1}H_2O$ signal (4.82 ppm at 20.0°C) not to be affected by band-selective water flip-back pulses (28) and the amide resonance of Arg46 is therefore visible only with artificially reduced intensity in amide-detected NMR experiments. Additional upfield shifts of ^{1}H chemical shifts were also identified for one of the two methyl groups of Val40 (–0.36 ppm), which is positioned in between the aromatic side chains of Phe114 and Tyr116, for the $^{1}H\delta1$ methyl group of Ile73 (–0.15 ppm), which is oriented towards Phe69, as well as for one of the two methyl groups of Val26 (0.18 ppm), which faces the aromatic ring of Phe114, and for one of the two protons of the $^{1}H\delta$ methylene group of Lys109 (0.68 ppm), which is close to Tyr105. Strong downfield shifts of ^{1}H chemical shifts were found for one of the two protons of the $^{1}H\beta$ methylene group of Asp110 (3.79 ppm), which is in the vicinity of the aromatic side-chain of Tyr116, for Thr118 $^{1}H\alpha$ (6.28 ppm), which is adjacent to the aromatic side-chain of Tyr119, and for Tyr119 $^{1}H\alpha$ (6.15 ppm) itself.

Conformational Dynamics–While the

structural core from Ser18 to Ala120 is well defined in solution with an average atomic RMSD from the average structure of 0.72 Å for the backbone and 1.30 Å for all heavy atoms (Table 1), several regions of the protein are constrained by only very few long-range NOE restraints (Fig. 3D) and therefore show markedly increased atomic RMSDs (Fig. 3C), namely the N-terminus (Met1 to Lys17), the C-terminus (Ser121 to Gly126), and – to a lesser extent – the loops between strands β_1 and β_2 (Tyr44 to Thr56), between helix α_3 and strand β_3 (Met77 to Phe85), and between strand β_3 and helix α_4 (Asn90 to Ala99). Inspection of the ^{15}N relaxation data (Figs. 3 and 4) reveals that these regions are indeed highly flexible as indicated by several $\{^1H\}^{15}N$ values below 0.65 (29), ^{15}N transverse relaxation rates R_2 significantly slower than the average over residues Ser18 to Ala120 of 25.0/s ± 6.7/s, and ^{15}N longitudinal relaxation rates R_1 significantly faster than the average over residues Ser18 to Ala120 of 0.87/s ± 0.07/s (Fig. 4). Accordingly, "model-free" analysis (30) of the ^{15}N relaxation data reveals large-amplitude backbone motions on the sub-nanosecond time-scale that are reflected in low generalized order parameters S^2 at both termini and in some loop regions (Fig. 3B). By contrast, the regular secondary structure elements are quite rigid on the sub-nanosecond time-scale, with S^2 values consistently exceeding 80%. The ratios between ^{15}N transverse and longitudinal relaxation rates of the rigid structural core of LC3C at 800 MHz are best fit by an oblate axially symmetric rotational diffusion tensor with eigenvalues of 1.39×10^7/s and 1.30×10^7/s at 20.0°C, corresponding to overall rotational autocorrelation times (31) of τ_A = 12.0 ns, τ_B = 12.1 ns, and τ_C = 12.6 ns. In the approximation of fully isotropic rotational diffusion this reduces to a single autocorrelation time of τ_{iso} = 12.3 ns. Although prediction of the hydrodynamics of LC3C on the basis of its tertiary structure is not straightforward because of the flexibility of the long terminal regions, these autocorrelation times are slightly longer than but still consistent with the hydrodynamic properties expected for a predominantly monomeric protein the size of LC3C in the relatively viscous buffer used here.

In addition to the generalized order parameters S^2 from ^{15}N relaxation, which are a measure of the motional restriction of the amide bond vector orientation with respect to the molecular frame on the sub-nanosecond time-scale on a scale of 0 (unrestricted motion) to 1 (rigid), we also calculated the Random Coil Index (RCI) (32) order parameters, S_{RCI}^2, which are a measure of how different the backbone chemical shifts are from those of a disordered random coil on a scale of 0 (typical for a random coil) to 1 (typical for a well-ordered backbone conformation). In general, the generalized order parameters from ^{15}N relaxation, S^2, are in good agreement with the RCI order parameters, S_{RCI}^2, with one very conspicuous exception (Fig. 3B): Although the orientation of the NTR relative to the structural core of the molecule is largely disordered (S^2 < 50%), the local backbone conformation of the first four residues is not consistent with a random coil (S_{RCI}^2 > 60%). Instead, a local backbone overlay of these residues reveals that the three consecutive proline residues Pro2 to Pro4 adopt a canonical polyproline II (PPII) helical geometry (Fig. 5) with its typical backbone torsion angles $\Phi \approx -75°$ and $\Psi \approx +120°$. From a structural point of view, the conformation of the unique NTR of LC3C (Fig. 1) in solution can therefore be described as an amino-terminal PPII motif attached to the ubiquitin-like core of the protein via a highly flexible 13-residue tether.

Whereas R_1 is solely sensitive to fast dynamics in the ns to ps regime, R_2 is also influenced by slower conformational exchange processes on the µs to ms time-scale (33). Inspection of the ^{15}N R_2 rates indeed shows many residues with ^{15}N transverse relaxation rates that are highly elevated by conformational exchange contributions (Fig. 4A). More detailed analysis using the “model-free” formalism (30) reveals that a large number of backbone amide groups covering virtually the entire structural core of the protein are affected by one or more conformational exchange processes on the µs to ms time-scale (data not shown), most prominently helix α_2 (especially its C-terminal side), the loop connecting strands β_1 and β_2, the loops before and after strand β_3, and the C-terminal region (Fig. 4A). These “hotspots” are corroborated by preliminary ^{15}N CPMG relaxation dispersion experiments but are non-contiguous in the tertiary structure, so delineation of the number and nature

of these extensive conformational exchange processes has to await systematic quantification by relaxation dispersion spectroscopy, which is beyond the scope of the present work.

Conformational exchange processes can also affect the backbone amide H/D exchange rates, k_{ex}. Amide protons involved in stable hydrogen bonds are protected from exchange with the solvent and therefore show very large protection factors, $PF = k_{int}/k_{ex}$, which measure how many times slower the protons exchange with the solvent in NMR buffer than under denaturing (random coil) conditions. However, if such a hydrogen-bonded ("closed") conformation C is in equilibrium with an alternate conformation O that is not hydrogen-bonded ("open") then solvent exchange will readily occur via the fraction p_O of the protein that populates the alternate conformation. In the case of conformational exchange on the micro- to millisecond time-scale at pH 6.0 and 20°C it can be shown (34) that the resulting protection factors should be of the order of the inverse of the fractional population of the "open" state, $PF \approx 1/p_O$. As expected, the distribution of the highly protected backbone amide groups primarily reflects the hydrogen bonds stabilizing the regular secondary structure elements of LC3C (Fig. 6). By contrast, none of the amide groups in the flexible terminal regions is sufficiently protected from solvent exchange to allow experimental detection. Note that most of the amide protons in the loops identified above as "hotspots" of the conformational exchange on the millisecond time-scale also appear to exchange readily with the solvent (Fig. 6), indicating that the hydrogen bonding network of the regular secondary structure elements is stable and preserved by the conformational exchange processes; indeed, the high protection factors $PF \approx 2\times10^3$ to 3×10^4 found in all regular secondary structure elements are at variance with those expected for an "open" state with a fractional population $p_O >> 0.1\%$ large enough to give rise to any significant exchange line broadening. In particular, this rules out global unfolding of LC3C as the source of the observed exchange line broadening.

Comparison with X-ray Structures– Overall, the NMR solution structure is in excellent agreement with the X-ray structures published for free LC3C(8-125) (14; PDB 3WAM), LC3C in complex with NDP52 (15; PDB 3VVW), and LC3C(8-125) in complex with the LIR of Atg13 (14; PDB 3WAP) (Fig. 7), with RMSDs of 0.65 Å, 0.89 Å, and 1.09 Å, respectively, for the backbone atoms of the structural core from Ser18 to Ala120. Minor differences are seen for the loops between strands β_1 and β_2 (Tyr44 to Thr56) and between helix α_3 and strand β_3 (Met77 to Phe85), which are involved in crystal contacts in the X-ray structures (14) and undergo backbone motions on the pico- to nanosecond time-scale in solution (see above). The largest differences, however, are observed for the NTR from the N-terminus to Lys17 (Fig. 7). In the crystal structure of LC3C in complex with NDP52 (15; PDB 3VVW) residues Met1 to Pro12 could not be observed in the electron density map, consistent with our observation that this region exhibits no long-range order relative to the structural core of the protein (see above). The crystal structures of LC3C(8-125) in the free form and in complex with Atg13 (14; PDB 3WAM and 3WAP, respectively) lack the additional six residues - including the polyproline motif - at the N-terminus of LC3C compared to LC3A and LC3B entirely (Fig. 1). In the absence of Atg13 no electron density could be found for residues before Arg11 but an additional helix α_1 is formed from Pro12 to Lys17, which is also found in many other proteins of the Atg8 family (14). Whether this difference in conformation is a consequence of the different crystallization conditions, the different crystal packing, the different resolution of the electron density maps, or the presence of the LIR of Atg13 remains unclear. In solution, no medium-range NOE pattern characteristic for such an additional helix α_1 could be identified (Fig. 3D), and the low RCI order parameters S_{RCI}^2 are not indicative of any stable secondary structure in this region (Fig. 3B). However, some of the resonances in this region could not be identified in the NMR spectra (27), most likely as a result of exchange line broadening due to conformational heterogeneity, so it is possible that this region transiently forms a metastable α-helical conformation. In addition to the N-terminal region, there are also conformational differences in the C-terminal region: Whereas the C-terminal residues Ser121 to Gly126 fold back towards the face of the central β-sheet in the crystal structures (Fig. 7), this region is poorly defined in solution (Fig. 2) by

the sparse medium- and long-range NOEs (Fig. 3D), which reflects high mobility on the ps to ns time-scale (see above) and line broadening due to conformational exchange on the µs to ms time-scale (Fig. 4A). The mobility of the C-terminus in solution ensures that Gly126 (which is notably absent in the construct LC3C(8-125) used for two of the crystal structures; 14) is readily accessible for lipid conjugation by the ATG7/ATG3 system.

Phosphorylation–In contrast to the GABARAP-like protein subfamily, the LC3 proteins share an amino-terminal, conserved PKA phosphorylation site (22). In LC3C, the target residue is Ser18, whose hydroxyl group provides the N-capping hydrogen bond acceptor (35) for helix α_2 (see above). We have used a series of [^{1}H-^{15}N] HSQC spectra to follow chemical shift changes of the LC3C backbone amide groups during incubation with PKA *in vitro*. Subsequently, after > 72 h, *in vitro* PKA-treated LC3C was proteolytically cleaved and analyzed by MALDI-LTQ-Orbitrap MS/MS. Glu-C hydrolysis of LC3C resulted in an amino-terminal fragment (GSMPPPQKIPSVRPFKQRKSLAIRQEE) for which a change in mass equivalent to the addition of a single phosphate group could be identified, and this fragment also gave rise to mass spectrometric bands equivalent to a neutral loss of H_3PO_4 (mass change approximately -98 Da) and HPO_3 (mass change approximately -80 Da), which are characteristic for phosphorylated peptides.

The signal-to-noise ratio of the [^{1}H-^{15}N] HSQC spectra decreased over the incubation period of 45 h, although the solution remained clear and no new set of peaks with random coil chemical shifts that would indicate denaturation of the protein sample was observed to emerge. Initial chemical shift changes of several backbone amide resonances were already observed within the first 3.5 h after addition of PKA, but no further changes were detected after 10.5 h. Four qualitatively different patterns of chemical shift changes were found for different sets of residues: (i) Most of the backbone amide resonances show no significant chemical shift changes at all, including the intense resonances of the mobile amino-terminal residues from Met1 to Val10 (Fig. 8A) and the carboxy-terminal residues Thr124 and Gly126, indicating that the conformation of these regions is unaffected by phosphorylation. (ii) By contrast, the amide groups of residues Arg11 to Gln15 exhibit two separate resonances with similar intensities in the presence of PKA, one at the position of the resonance in the unphosphorylated form plus an additional one with slightly different chemical shifts that appears to be present only with extremely low intensity close to the detection limit in the unphosphorylated form, as seen in Fig. 8B for Phe13. Accordingly, the effect of phosphorylation of Ser18 on this region appears to be an increase in the population of an alternate conformation, which exchanges with the conformation dominating in the unphosphorylated form on a time-scale of about 10 ms or slower, or not at all. It is possible that this alternate conformation is essentially the additional helix α_1 that this region forms in the crystal structure of LC3C(8-125) (see above), although the relatively small chemical shift changes are also compatible with a subtler change in conformation. Note that two separate sets of NMR resonances resulting from slow conformational exchange are also observed for many residues located in or near helix α_1 of GABARAP, which does not share the PKA phosphorylation site (Fig. 1), in the absence of PKA (9; C. M. and P. N., unpublished). (iii) Another set of backbone amide resonances, such as those of Glu25 (Fig. 8A), Val26 (Fig. 8B), Asp110, Glu111 (Fig. 8D), Gly113, and Glu123 (Fig. 8C) display a gradual but complete transition over the first 10.5 h of incubation with PKA from the chemical shifts of the unphosphorylated form to a newly emerging resonance with chemical shifts close enough to the original resonance to be readily traced. (iv) Finally, another set of backbone amide resonances including Ser18 (Fig. 8C), Leu19, Ala20 (Fig. 8C) and Arg22 (Fig. 8A) in the immediate vicinity of the phosphorylation site, as well as Ala31 and Lys32 at the C-terminal end of helix α_2, Tyr44, Arg46, Phe49 and Leu50 in the loop connecting strands β_1 and β_2, Lys55 to Lys57 in the LIR binding region, Tyr86, Asp112, and Ser121 disappear within 7.0 h after addition of PKA without any new resonance with similar chemical shifts emerging. We cannot rule out that amide resonances for these residues in the phosphorylated protein appear elsewhere in the spectrum because the quality of the NMR spectra of phosphorylated LC3C under these buffer conditions is insufficient for multidimensional assignment experiments. Alternatively, the disappearance of these resonance could be caused

by unfavorable relaxation properties due to sample aggregation or chemical exchange on the μs to ms time-scale. Either way, the observed chemical shift changes indicate that phosphorylated LC3C is even more conformationally heterogeneous than unphosphorylated LC3C.

As described above, the side-chain of Ser18 provides an N-capping hydrogen bond acceptor (Fig. 9), so phosphorylation of Ser18 could have an influence on the stability of this hydrogen bond and, in turn, on the stability of helix α_2 in general, maybe even trigger a helix-to-coil transition (35). Moreover, helix α_2 is held in place by several favorable tertiary contacts, most notably electrostatic interactions of the side-chain of Arg22 with the negatively charged side-chains of Asp110, Glu111, and Asp112 (Fig. 9) in the loop between helix α_4 and strand β_4, a rigid loop that shows little sign of backbone mobility on the ps to ns time-scale nor of line broadening from conformational exchange on the μs to ms time-scale (Figs. 2, 3, 4). The chemical shift changes of the backbone amide resonance from Asp110 to Gly113 upon addition of PKA (see above) suggest that the negative charge of the phosphate group modification modulates these interactions.

To test the plausibility of these hypotheses we performed comparative molecular dynamics (MD) simulations of LC3C in the unmodified (Ser18) and phosporylated (pSer18) form. In the context of a random-coil peptide, the pK_a of phosphoserine is very close to 6.0, the pH of the NMR buffer used here, and the exchange between the protonated (monoanionic) and deprotonated (dianionic) states is fast on the chemical shift time-scale (36). Although both the pK_a and the exchange rate of the protonation equilibrium can be modulated by tertiary interactions we have to assume that both states are populated to a considerable degree in our NMR experiments (37); in fact, exchange between these two protonation states might well be the cause underlying some of the line broadening or peak splitting in the NMR spectra of phosphorylated LC3C described above. Therefore, we calculated three MD trajectories of 100 ns each, one with the unmodified serine (Ser18), one with the protonated phosphoserine ($pSer18^-$), and one with the deprotonated phosposerine ($pSer18^{2-}$). The hydrogen bond between the amide group of Ile21 and the side-chain of Ser18 is indeed formed a considerable fraction of the time along the MD trajectory (albeit not as stable as expected from the amide H/D exchange experiments) (Fig. S3) but virtually absent from the MD trajectories for $pSer18^-$ (Fig. S4) and $pSer18^{2-}$ (Fig. S5), which corroborates our hypothesis that this hydrogen bond is destabilized by phosphorylation by PKA. However, helix α_2 remains stable for the entire duration of the MD trajectories regardless of the phosphorylation state of Ser18 (Figs. S3, S4, S5) and no helix-to-coil transition is observed, at least not on the time-scale of 100 ns covered by the MD simulations. Instead of forming a hydrogen bond with the amide group of Ile21 the single negative charge of the monoanionic phosphate group of $pSer18^-$ favors a salt bridge with the positively charged side-chain of Lys17 (Fig. S4); intriguingly, the additional helix α_1 is populated a significant fraction of the MD trajectory calculated with $pSer18^-$ (Fig. S4), in support of our suspicion that phosphorylation of Ser18 might stabilize a helical conformation in this region (see above). Of course, these MD simulations do not rule out the possibility of any additional conformational changes on a time-scale slower than about 100 ns that might be triggered by phosphorylation. For example, the disappearance of the amide resonances of Ala31 and Lys32 at the C-terminal end of helix α_2 could readily be explained if this region acts as a hinge for repositioning of helix α_2. In light of our experimental observation that the chemical shifts of several resonances in the LIR binding region of LC3C are strongly affected by phosphorylation (see above) a modulating effect of PKA on both, affinity as well as specificity of LC3C for its target LIRs appears highly likely.

Conclusions–High-resolution structure determination by NMR spectroscopy confirms that the well-ordered core (residues 18 to 120) of the autophagy-related protein MAP1LC3C adopts virtually the same tertiary structure in solution as in X-ray crystallography, although extensive exchange line broadening reveals the existence of alternate, low-populated conformations. By contrast, both termini are highly mobile. The mobility of the C-terminus guarantees full access of the lipid conjugation machinery to the C-terminal residue for membrane anchoring of LC3C. The N-terminus forms a polyproline II

helix (Pro2, Pro3, Pro4) tethered to the ubiquitin-like core via a flexible linker, an arrangement that has been described as a "sticky arm" in the literature (38). Short proline-rich regions are a highly diverse protein-protein interaction motif found in a large number of proteins, often recognized by dedicated protein-protein interaction domains such as WW domains, SH3 domains, or profilins (38). In this context, ligand specificity is usually conferred by the spacing of the proline residues as well as the biophysical properties of the side-chains flanking the prolines, and sometimes further modulated by phosphorylation. While the N-terminal sequence motif of LC3C, MPPPQK (Fig. 1), deviates from the stereotypical WW and SH3 domain ligand motifs as compiled by Kay et al. (38), interfacing to such a protein-protein interaction domain cannot be ruled out as the functional role of the N-terminal PPII motif of LC3C. Intriguingly, though, proline-rich regions have also been identified to mediate interactions with microtubules, more specifically with the β-tubulin subunit (39). Flexible proline-rich regions are involved in the interaction of the intrinsically disordered microtubule-associated protein Tau with microtubules, and phosphorylation has recently been shown to change the conformation and microtubule interaction mode of the second proline-rich region of Tau (40,41). The full name MAP1LC3 (microtubule associated proteins 1 light chain 3) reflects the fact that this subfamily was originally identified as proteins associated with microtubules (42), and the interplay between autophagy and microtubules is well-documented (43), albeit still poorly understood. In the case of GABARAP the interaction with the negatively charged microtubular surface was mapped to the positively charged helix α_2 with 7 basic residues (44). Because this motif appears to be absent from LC3C, where only 3 of these 7 basic residues are conserved in helix α_2 from Ser18 to Phe33 (Fig. 1), it is plausible to hypothesize that the divergence of the amino-terminal region across the human GABARAP/MAP1LC3 family (Fig. 1) provides for differential interaction with the cytoskeleton. The PKA phosphorylation site at Ser18 at the N-cap of helix α_2 of LC3C is well-positioned to further modulate such an interaction. The chemical shift changes upon phosphorylation do not indicate a direct influence on the PPII motif itself but are consistent with repositioning of helix α_2 and possibly also stabilization of a short additional helix α_1 in the NTR. Phosphorylation of Ser18 also has a large effect on the chemical shifts in the LIR binding region of LC3C and can therefore be expected to modulate affinity and specificity of the interaction of LC3C with its target LIRs or CLIRs.

EXPERIMENTAL PROCEDURES

Cloning, Expression and Purification– LC3C was cloned, expressed and purified as an amino-terminal GST-LC3C fusion protein as described in detail previously (27). Thrombin cleavage and final purification by cation exchange and size exclusion chromatography yielded highly pure samples of the cytosolic LC3C protein of 126 amino acids with a two-residue amino-terminal cloning artifact (Gly-1 and Ser0) (Figs. S1 and S2), which were concentrated to between 370 μM and 700 μM for NMR spectroscopy.

NMR Spectroscopy–NMR samples of 370 μM to 700 μM [U-^{15}N] or [U-^{13}C,^{15}N] LC3C were prepared in 20 mM PIPES, 150 mM NaCl, 0.1 mM EDTA and supplemented with 2% (v/v) glycerol-d_8 (Euriso-top, Gif-sur-Yvette, France) and 10% (v/v) ^2D_2O at pH 6.0 (NMR buffer). NMR experiments were recorded at 20.0°C on Varian INOVA or Bruker AVANCE III spectrometers operating at ^{1}H frequencies of 600 MHz and 800 MHz and equipped with cryogenically cooled triple or quadruple resonance probes with pulse-field gradient capabilities. Sequence-specific ^{1}H, ^{15}N, and ^{13}C backbone and side-chain NMR resonance assignments and $^3J_{HNH\alpha}$ scalar coupling constants were reported previously (27; BMRB 26603). ^{1}H-^{1}H distance information was derived from the following nuclear Overhauser effect spectroscopy (NOESY) experiments: 2D [^{1}H-^{1}H] NOESY (45) (120 ms mixing time) in 99% ^2D_2O, 3D [^{1}H-^{15}N] NOESY-HSQC (46) (120 ms mixing time) in 90% ^1H_2O/10% ^2D_2O, 3D [^{1}H-^{13}C] NOESY-HSQC (47) (120 ms mixing time) in 99% ^2D_2O, 3D [^{1}H-^{15}N] [^{1}H-^{15}N] HSQC-NOESY-HSQC (48,49) (150 ms mixing time) in 90% ^1H_2O/10% ^2D_2O, and 3D [^{1}H-^{13}C] [^{1}H-^{15}N] HSQC-NOESY-HSQC (50) (150 ms mixing time) in 90% ^1H_2O/10% ^2D_2O. The ^1H_2O resonance was suppressed by excitation sculpting

(51) in the 2D [^{1}H,^{1}H] homonuclear experiments and by gradient coherence selection in the heteronuclear experiments, quadrature detection in the indirect dimensions was achieved by States-TPPI (52) or the echo/antiecho method (53,54). All NMR spectra were processed using NMRPipe and NMRDraw (55) and analysed with NMRViewJ (56) and CcpNmr Analysis (57).

To measure amide proton/deuteron (H/D) exchange a sample of 570 µM [U-^{15}N] LC3C in NMR buffer was freeze-dried and a series of seven consecutive [^{1}H-^{15}N] HSQC experiments was recorded 0.3, 1.6, 2.8, 5.4, 7.9, 12.9, and 17.9 h after reconstitution of the lyophilized sample in ^2D_2O. Signal intensities in the resulting [^{1}H-^{15}N] HSQC spectra were quantified using CcpNmr Analysis and fitted by mono-exponential decay functions to extract amide H/D exchange rates for semi-quantitative analysis (58). Experimental H/D exchange rates, k_{ex}, were converted into protection factors PF = k_{int}/k_{ex}, where k_{int} are the intrinsic (unprotected) H/D exchange rates for these experimental conditions as predicted from the amino acid sequence (59) using the SPHERE server (http://landing.foxchase.org/research/labs/roder/sphere).

Protein backbone amide group dynamics on the pico- to nanosecond time-scale was probed by ^{15}N spin relaxation experiments (33,60) recorded on a sample of 510 µM [U-^{15}N] LC3C in NMR buffer at 800 MHz and 20.0°C. ^{15}N longitudinal relaxation rates, R_1, were obtained from ^{15}N inversion recovery experiments (60,61) with 11 different inversion recovery times (3 of them collected in duplicate) between 80 ms and 1200 ms and a recycle delay of 2.5 s. ^{15}N rotating frame relaxation rates, $R_{1\rho}$, were obtained from ^{15}N spin lock experiments (62) with 10 different spin lock times (3 of them collected in duplicate) between 10 ms and 100 ms with a spin lock field strength of 2.02 kHz and a recycle delay of 3.0 s. Amide resonance intensities were quantified by three-way decomposition and fit by mono-exponential decay functions using MUNIN (63,64) to extract the ^{15}N relaxation rates R_1 and $R_{1\rho}$. ^{15}N transverse relaxation rates, R_2, were calculated from R_1 and $R_{1\rho}$ (65). {^{1}H}^{15}N heteronuclear NOE values were calculated as the amide resonance intensity ratios in a pair of interleaved spectra recorded with and without proton saturation by applying a train of 120° pulses at a field strength of 11.6 kHz for the final 6.0 s of the recycle delay of 15.0 s (60). Uncertainties of the {^{1}H}^{15}N NOE values were estimated from the spectral noise background. The overall rotational diffusion tensor and "model-free" parameters (30) describing internal motion of the protein backbone such as the generalized order parameters for sub-nanosecond internal motion, S^2, were determined by fitting the experimental ^{15}N R_1 and R_2 rates and {^{1}H}^{15}N NOE values using Tensor 2.0 (66) with the default parameters based on the lowest-energy structure of LC3C. Amide groups with {^{1}H}^{15}N NOE values below 0.65 and/or with R_2/R_1 ratios deviating by more than 10% from the mean value were considered to possess significantly increased internal mobility and excluded from the calculation of the rotational diffusion tensor (29). The presence of millisecond time-scale exchange processes was probed by ^{15}N single-quantum Carr-Purcell-Meiboom-Gill (CPMG) relaxation dispersion experiments (67,68) recorded on this sample at 800 MHz and 20.0°C. In each ^{15}N CPMG experiment 14 different CPMG frequencies $\nu_{CPMG} = 1/(2\delta)$, where δ is the time between consecutive refocusing pulses, ranging from 50.0 Hz to 1000.0 Hz were sampled during a constant-time relaxation interval of T_{CPMG} = 40 ms. Amide resonance intensities $I(\nu_{CPMG})$ were quantified by three-way decomposition using MUNIN (63,64) and converted into effective transverse relaxation rates, $R_{2eff}(\nu_{CPMG}) = -\ln(I(\nu_{CPMG})/I_0)/T_{CPMG}$, where I_0 is the corresponding resonance intensity in a reference spectrum recorded without the constant-time relaxation interval. Error estimates ΔR_{2eff} for R_{2eff} were obtained from duplicate measurements at 3 different ν_{CPMG} values as described previously (69).

Structural Restraints and Structure Calculation–Based on the almost complete assignment of the ^{1}H, ^{15}N, and ^{13}C resonances of LC3C published previously (27), the NOE cross peaks in the [^{1}H-^{15}N] and [^{1}H-^{13}C] NOESY-HSQC spectra were quantified with CcpNmr Analysis 2.4.1 (57) and automatically assigned and converted into NOE distance restraints using ARIA 2.3 (70,71) in an iterative procedure. All resulting NOE assignments were inspected

manually. 94 $^{3}J_{HNH\alpha}$ coupling constants were obtained from a quantitative HNHA experiment with a coherence transfer time of 12.3 ms and relaxation correction factor of 1.1 (72,73) as described previously (27). 32 of these $^{3}J_{HNH\alpha}$ in the well-ordered core of the protein were sufficiently different from the value of 7.0 Hz that is indicative of rotameric averaging (74) and had sufficiently small experimental uncertainties to be converted into Φ backbone torsion angle restraints using the Karplus relation (72) as implemented in CcpNmr Analysis with a tolerance of ±30°. Additional Φ and Ψ backbone dihedral angle restraints were derived from the secondary chemical shifts ($^{1}H_{N}$, $^{1}H_{\alpha}$, ^{15}N, ^{13}CO, $^{13}C_{\alpha}$, $^{13}C_{\beta}$) by TALOS-N (75,76). Amide hydrogen bond donors were identified as slowly exchanging protons in the H/D exchange experiment and the corresponding hydrogen bond acceptors were found by proximity in later stages of the structure calculation process and then incorporated as additional distance restraints. For each of the 51 hydrogen bonds the distance between the amide proton and the acceptor was restrained to between 1.5 Å and 2.3 Å and the distance between the amide nitrogen and the acceptor to between 2.5 Å and 3.5 Å. These experimental restraints served as input for the calculation of 100 structures using restrained molecular dynamics simulations with ARIA-optimized CNS 1.21 (77) using the CNS protocol parameters listed in Table S1. The 10 structures showing the lowest energy values were further refined in an explicit water shell using the CSDX/OPLS hybrid force field as implemented in ARIA/CNS (78) and selected for further characterization. Structural models were visualized by PyMOL (The PyMOL Molecular Graphics System, Version 1.7.2.1, Schrödinger, LLC) and analyzed using ARIA/CNS, the NIH version 1.2.1 (79) of X-PLOR 3.851 (80), PROCHECK-NMR (81), MolProbity (82), and CING (83).

In-vitro Phosphorylation–LC3C samples were phosphorylated *in vitro* using the catalytic subunit of murine PKA (NEB, Frankfurt a. M., Germany). A 700 µM sample of [U-^{15}N] or [U-^{13}C,^{15}N]-labeled LC3C in NMR buffer was supplemented with 1 mM ATP and subsequently 5 mM $MgCl_2$ (PKA buffer). This change in buffer conditions was monitored by [^{1}H-^{15}N] HSQC spectra to rule out any major spectral differences that might indicate a substantial modulation of the structure or dynamics of LC3C. Finally, 0.5 µl PKA (circa 1000 U) were added and the reaction was monitored by a series of twelve consecutive [^{1}H-^{15}N] HSQC experiments at 600 MHz and 20.0°C over a period of 45 h. Additionally, [^{1}H-^{13}C] ct-HSQC and HNCA experiments were recorded at 600 MHz and 20.0°C after 72 h of incubation. Furthermore, the phosphorylation reaction was analyzed by proteolytic hydrolysis with trypsin and Glu-C of the [U-^{13}C,^{15}N]-labeled reaction product, followed by MALDI-LTQ-Orbitrap MS/MS analysis.

Molecular Dynamics Simulations–The lowest-energy solution structure after water refinement was used as a starting structure for molecular dynamics (MD) simulations. Three independent phosphorylation states of LC3C were simulated: unmodified serine 18 (Ser18), serine 18 mutated to a protonated phosphoserine (pSer18^{-}), and serine 18 mutated to a deprotonated phosphoserine (pSer18^{2-}). The Amber force field ff99SB-ILDN (84) was used in conjunction with the TIP3P water model (85). Parameters for bonded and van der Waals interactions of the phosphorylated serine residue were taken from the GAFF force field (86) generated with acpype.py (87) and the partial charges from Homeyer et al. (37). All MD simulations were performed using GROMACS 5.1 (88). The protein was centered in a dodecahedral box with a minimum solute-to-wall distance of 1 nm. Sodium chloride ions were added to neutralize the systems and mimic a salt concentration of approximately 100 mM. The systems were first energy-minimized, equilibrated in the NPT ensemble (i. e., with a constant number of molecules, pressure, and temperature) for 1 ns and then simulated for 100 ns each in the NPT ensemble at 298 K (Nosé-Hoover thermostat; 89) and 1.0 bar (Parrinello-Rahman barostat; 90). Van der Waals and short-range electrostatic interactions were cut off at 12 Å and long-range electrostatics were treated with the particle mesh Ewald method (91). Bond lengths and bond angles of hydrogen atoms were constrained to their equilibrium values with the LINCS algorithm (92). The equations of motion were integrated with a velocity Verlet integrator and a time step of 2 fs. Atom positions were saved every 10 ps.

Acknowledgments: This work has been supported by grants from the DFG (SFB1208, A07 (B. S.), B02 (D. W.) and B03 (P. N.)). The authors acknowledge access to the Jülich-Düsseldorf Biomolecular NMR Center.

Databases: The atomic coordinates and experimental restraints (code 2NCN) have been deposited in the Protein Data Bank (http://www.wwpdb.org/).

Conflict of interest: The authors declare that they have no conflicts of interest with the contents of this article.

Author contributions: C. K., O. H. W., D. W., and P. N. conceived and designed the experiments. C. K. produced the NMR samples. C. K., C. M., and P. N. performed the NMR experiments. C. K., C. M., H. S., O. H. W., and P. N. analyzed the data. P. F. H. performed and analyzed the mass spectroscopy. O. S. and B. S. performed and analyzed the MD simulations. All authors wrote the paper and approved the final version of the manuscript.

REFERENCES

1. Nakatogawa, H., Suzuki, K., Kamada, Y., and Ohsumi, Y. (2009) Dynamics and diversity in autophagy mechanisms: lessons from yeast. *Nat. Rev. Mol. Cell Biol.* **10**, 458-467
2. Nakatogawa, H., Ichimura, Y., and Ohsumi, Y. (2007) Atg8, a Ubiquitin-like Protein Required for Autophagosome Formation, Mediates Membrane Tethering and Hemifusion. *Cell* **130**, 165-178
3. Ichimura, Y., Kirisako, T., Takao, T., Satomi, Y., Shimonishi, Y., Ishihara, N., Mizushima, N., Tanida, I., Kominami, E., Ohsumi, M., Noda, T., and Ohsumi, Y. (2000) A ubiquitin-like system mediates protein lipidation. *Nature* **408**, 488-492
4. Shpilka, T., Weidberg, H., Pietrokovski, S., and Elazar, Z. (2011) Atg8: an autophagy-related ubiquitin-like protein family. *Genome Biol.* **12**, 226
5. Weiergräber, O. H., Mohrlüder, J., and Willbold, D. (2013) Atg8 Family Proteins — Autophagy and Beyond. In *Autophagy - A Double-Edged Sword - Cell Survival or Death?* (Bailly, Y., Ed.) InTech, pp. 13-45, DOI: 10.5772/55647
6. Schwarten, M., Stoldt, M., Mohrlüder, J., and Willbold, D. (2010) Solution structure of Atg8 reveals conformational polymorphism of the N-terminal domain. *Biochem. Biophys. Res. Commun.* **395**, 426-431
7. Kumeta, H., Watanabe, M., Nakatogawa, H., Yamaguchi, M., Ogura, K., Adachi, W., Fujioka, Y., Noda, N. N., Ohsumi, Y., and Inagaki, F. (2010) The NMR structure of the autophagy-related protein Atg8. *J. Biomol. NMR* **47**, 237-241
8. Noda, N. N., Satoo, K., Fujioka, Y., Kumeta, H., Ogura, K., Nakatogawa, H., Ohsumi, Y., and Inagaki, F. (2011) Structural Basis of Atg8 Activation by a Homodimeric E1, Atg7. *Mol. Cell* **44**, 462-475
9. Stangler, T., Mayr, L. M., and Willbold, D. (2002) Solution Structure of Human $GABA_A$ Receptor-associated Protein GABARAP: implications for biological function and its regulation. *J. Biol. Chem.* **277**, 13363-13366
10. Rozenknop, A., Rogov, V. V., Rogova, N. Y., Löhr, F., Güntert, P., Dikic, I., and Dötsch, V. (2011) Characterization of the Interaction of GABARAPL-1 with the LIR Motif of NBR1. *J. Mol. Biol.* **410**, 477-487
11. Kouno, T., Mizuguchi, M., Tanida, I., Ueno, T., Kanematsu, T., Mori, Y., Shinoda, H., Hirata, M., Kominami, E., and Kawano, K. (2005) Solution Structure of Microtubule-associated Protein Light Chain 3 and Identification of Its Functional Subdomains. *J. Biol. Chem.* **280**, 24610-24617
12. Noda, N. N., Kumeta, H., Nakatogawa, H., Satoo, K., Adachi, W., Ishii, J., Fujioka, Y., Ohsumi, Y., and Inagaki, F. (2008) Structural basis of target recognition by Atg8/LC3 during selective autophagy. *Genes Cells* **13**, 1211-1218
13. Rogov, V. V., Suzuki, H., Fiskin, E., Wild, P., Kniss, A., Rozenknop, A., Kato, R., Kawasaki, M., McEwan, D. G., Löhr, F., Güntert, P., Dikic, I., Wakatsuki, S., and Dötsch, V. (2013) Structural basis for phosphorylation-triggered autophagic clearance of *Salmonella*. *Biochem. J.* **454**, 459-466
14. Suzuki, H., Tabata, K., Morita, E., Kawasaki, M., Kato, R., Dobson, R. C., Yoshimori, T., and Wakatsuki, S. (2014) Structural Basis of the Autophagy-Related LC3/Atg13 LIR Complex: Recognition and Interaction Mechanism. *Structure* **22**, 47-58
15. von Muhlinen, N., Akutsu, M., Ravenhill, B. J., Foeglein, A., Bloor, S., Rutherford, T. J., Freund, S. M., Komander, D., and Randow, F. (2012) LC3C, Bound Selectively by a Noncanonical LIR Motif in NDP52, Is Required for Antibacterial Autophagy. *Mol. Cell* **48**, 329-342
16. Weidberg, H., Shpilka, T., Shvets, E., Abada, A., Shimron, F., and Elazar, Z. (2011) LC3 and GATE-16 N Termini Mediate Membrane Fusion Processes Required for Autophagosome Biogenesis. *Dev. Cell* **20**, 444-454

17. Chu, C. T., Ji, J., Dagda, R. K., Jiang, J. F., Tyurina, Y. Y., Kapralov, A. A., Tyurin, V. A., Yanamala, N., Shrivastava, I. H., Mohammadyani, D., Qiang Wang, K. Z., Zhu, J., Klein-Seetharaman, J., Balasubramanian, K., Amoscato, A. A., Borisenko, G., Huang, Z., Gusdon, A. M., Cheikhi, A., Steer, E. K., Wang, R., Baty, C., Watkins, S., Bahar, I., Bayr, H., and Kagan, V. E. (2013) Cardiolipin externalization to the outer mitochondrial membrane acts as an elimination signal for mitophagy in neuronal cells. *Nat. Cell Biol.* **15**, 1197-1205
18. Pankiv, S., Clausen, T. H., Lamark, T., Brech, A., Bruun, J. A., Outzen, H., Øvervatn, A., Bjørkøy, G., and Johansen, T. (2007) p62/SQSTM1 Binds Directly to Atg8/LC3 to Facilitate Degradation of Ubiquitinated Protein Aggregates by Autophagy. *J. Biol. Chem.* **282**, 24131-24145
19. Wild, P., Farhan, H., McEwan, D. G., Wagner, S., Rogov, V. V., Brady, N. R., Richter, B., Korac, J., Waidmann, O., Choudhary, C., Dötsch, V., Bumann, D., and Dikic, I. (2011) Phosphorylation of the Autophagy Receptor Optineurin Restricts *Salmonella* Growth. *Science* **333**, 228-233
20. Ichimura, Y., Kumanomidou, T., Sou, Y. S., Mizushima, T., Ezaki, J., Ueno, T., Kominami, E., Yamane, T., Tanaka, K., and Komatsu, M. (2008) Structural Basis for Sorting Mechanism of p62 in Selective Autophagy. *J. Biol. Chem.* **283**, 22847-22857
21. Birgisdottir, A. B., Lamark, T., and Johansen, T. (2013) The LIR motif - crucial for selective autophagy. *J. Cell. Sci.* **126**, 3237-3247
22. Cherra, S. J., Kulich, S. M., Uechi, G., Balasubramani, M., Mountzouris, J., Day, B. W., and Chu, C. T. (2010) Regulation of the autophagy protein LC3 by phosphorylation. *J. Cell Biol.* **190**, 533-539
23. Jiang, H., Cheng, D., Liu, W., Peng, J., and Feng, J. (2010) Protein kinase C inhibits autophagy and phosphorylates LC3. *Biochem. Biophys. Res. Commun.* **395**, 471-476
24. Blom, N., Gammeltoft, S., and Brunak, S. (1999) Sequence and Structure-based Prediction of Eukaryotic Protein Phosphorylation Sites. *J. Mol. Biol.* **294**, 1351-1362
25. Huang, R., Xu, Y., Wan, W., Shou, X., Qian, J., You, Z., Liu, B., Chang, C., Zhou, T., Lippincott-Schwartz, J., and Liu, W. (2015) Deacetylation of Nuclear LC3 Drives Autophagy Initiation under Starvation. *Mol. Cell* **57**, 456-466
26. Xie, Y., Kang, R., Sun, X., Zhong, M., Huang, J., Klionsky, D. J., and Tang, D. (2015) Posttranslational modification of autophagy-related proteins in macroautophagy. *Autophagy* **11**, 28-45
27. Krichel, C., Weiergräber, O. H., Pavlidou, M., Mohrlüder, J., Schwarten, M., Willbold, D., and Neudecker, P. (2016) Sequence-specific ^{1}H, ^{15}N, and ^{13}C resonance assignments of the autophagy-related protein LC3C. *Biomol. NMR Assign.* **10**, 41-43
28. Grzesiek, S., and Bax, A. (1993) The Importance of Not Saturating H_2O in Protein NMR. Application to Sensitivity Enhancement and NOE Measurements. *J. Am. Chem. Soc.* **115**, 12593-12594
29. Pawley, N. H., Wang, C., Koide, S., and Nicholson, L. K. (2001) An improved method for distinguishing between anisotropic tumbling and chemical exchange in analysis of ^{15}N relaxation parameters. *J. Biomol. NMR* **20**, 149-165
30. Lipari, G., and Szabo, A. (1982) Model-Free Approach to the Interpretation of Nuclear Magnetic Resonance Relaxation in Macromolecules. 2. Analysis of Experimental Results. *J. Am. Chem. Soc.* **104**, 4559-4570
31. Woessner, D. E. (1962) Nuclear Spin Relaxation in Ellipsoids Undergoing Rotational Brownian Motion. *J. Chem. Phys.* **37**, 647-654
32. Berjanskii, M. V., and Wishart, D. S. (2005) A Simple Method to Predict Protein Flexibility Using Secondary Chemical Shifts. *J. Am. Chem. Soc.* **127**, 14970-14971
33. Kay, L. E., Torchia, D. A., and Bax, A. (1989) Backbone Dynamics of Proteins As Studied by ^{15}N Inverse Detected Heteronuclear NMR Spectroscopy: Application to Staphylococcal Nuclease. *Biochemistry* **28**, 8972-8979

34. Neudecker, P., Robustelli, P., Cavalli, A., Walsh, P., Lundström, P., Zarrine-Afsar, A., Sharpe, S., Vendruscolo, M., and Kay, L. E. (2012) Structure of an Intermediate State in Protein Folding and Aggregation. *Science* **336**, 362-366
35. Doig, A. J., and Baldwin, R. L. (1995) N- and C-capping preferences for all 20 amino acids in α-helical peptides. *Protein Sci.* **4**, 1325-1336
36. Bienkiewicz, E. A., and Lumb, K. J. (1999) Random-coil chemical shifts of phosphorylated amino acids. *J. Biomol. NMR* **15**, 203-206
37. Homeyer, N., Horn, A. H. C., Lanig, H., and Sticht, H. (2006) AMBER force-field parameters for phosphorylated amino acids in different protonation states: phosphoserine, phosphothreonine, phosphotyrosine, and phosphohistidine. *J. Mol. Model.* **12**, 281-289
38. Kay, B. K., Williamson, M. P., and Sudol, M. (2000) The importance of being proline: the interaction of proline-rich motifs in signaling proteins with their cognate domains. *FASEB J.* **14**, 231-241
39. Gendreau, S., Schirmer, J., and Schmalzing, G. (2003) Identification of a tubulin binding motif on the $P2X_2$ receptor. *J. Chromatrogr. B* **786**, 311-318
40. Kadavath, H., Hofele, R. V., Biernat, J., Kumar, S., Tepper, K., Urlaub, H., Mandelkow, E., and Zweckstetter, M. (2015) Tau stabilizes microtubules by binding at the interface between tubulin heterodimers. *Proc. Natl. Acad. Sci. U.S.A.* **112**, 7501-7506
41. Schwalbe, M., Kadavath, H., Biernat, J., Ozenne, V., Blackledge, M., Mandelkow, E., and Zweckstetter, M. (2015) Structural Impact of Tau Phosphorylation at Threonine 231. *Structure* **23**, 1448-1458
42. Mann, S. S., and Hammarback, J. A. (1994) Molecular Characterization of Light Chain 3. *J. Biol. Chem.* **269**, 11492-11497
43. Mackeh, R., Perdiz, D., Lorin, S., Codogno, P., and Poüs, C. (2013) Autophagy and microtubules – new story, old players. *J. Cell. Sci.* **126**, 1071-1080
44. Coyle, J. E., Qamar, S., Rajashankar, K. R., and Nikolov, D. B. (2002) Structure of GABARAP in Two Conformations: Implications for $GABA_A$ Receptor Localization and Tubulin Binding. *Neuron* **33**, 63-74
45. Kumar, A., Ernst, R. R., and Wüthrich, K. (1980) A Two-Dimensional Nuclear Overhauser Enhancement (2D NOE) Experiment for the Elucidation of Complete Proton-Proton Cross-Relaxation Networks in Biological Macromolecules. *Biochem. Biophys. Res. Comm.* **95**, 1-6
46. Zhang, O., Kay, L. E., Olivier, J. P., and Forman-Kay, J. D. (1994) Backbone ^{1}H and ^{15}N resonance assignments of the N-terminal SH3 domain of drk in folded and unfolded states using enhanced-sensitivity pulsed field gradient NMR techniques. *J. Biomol. NMR* **4**, 845-858
47. Ikura, M., Kay, L. E., Tschudin, R., and Bax, A. (1990) Three-Dimensional NOESY-HMQC Spectroscopy of a ^{13}C-Labeled Protein. *J. Magn. Reson.* **86**, 204-209
48. Frenkiel, T., Bauer, C., Carr, M. D., Birdsall, B., and Feeney, J. (1990) HMQC-NOESY-HMQC, a Three-Dimensional NMR Experiment Which Allows Detection of Nuclear Overhauser Effects between Protons with Overlapping Signals. *J. Magn. Reson.* **90**, 420-425
49. Ikura, M., Bax, A., Clore, G. M., and Gronenborn, A. M. (1990) Detection of Nuclear Overhauser Effects between Degenerate Amide Proton Resonances by Heteronuclear Three-Dimensional Nuclear Magnetic Resonance Spectroscopy. *J. Am. Chem. Soc.* **112**, 9020-9022
50. Diercks, T., Coles, M., and Kessler, H. (1999) An efficient strategy for assignment of cross-peaks in 3D heteronuclear NOESY experiments. *J. Biomol. NMR* **15**, 177-180.
51. Hwang, T.-L., and Shaka, A. J. (1995) Water Suppression That Works. Excitation Sculpting Using Arbitrary Waveforms and Pulsed Field Gradients. *J. Magn. Reson. Series A* **112**, 275-279
52. Marion, D., Ikura, M., Tschudin, R., and Bax, A. (1989) Rapid Recoding of 2D NMR Spectra without Phase Cycling. Application to the Study of Hydrogen Exchange in Proteins. *J. Magn. Reson.* **85**, 393-399

53. Kay, L. E., Keifer, P., and Saarinen, T. (1992) Pure Absorption Gradient Enhanced Heteronuclear Single Quantum Correlation Spectroscopy with Improved Sensitivity. *J. Am. Chem. Soc.* **114**, 10663-10665
54. Schleucher, J., Sattler, M., and Griesinger, C. (1993) Coherence Selection by Gradients without Signal Attenuation: Application to the Three-Dimensional HNCO Experiment. *Angew. Chem. Int. Ed. Engl.* **32**, 1489-1491
55. Delaglio, F., Grzesiek, S., Vuister, G. W., Zhu, G., Pfeifer, J., and Bax, A. (1995) NMRPipe: A multidimensional spectral processing system based on UNIX pipes. *J. Biomol. NMR* **6**, 277-293
56. Johnson, B. A., and Blevins, R. A. (1994) NMRView: A computer program for the visualization and analysis of NMR data. *J. Biomol. NMR* **4**, 603-614
57. Vranken, W. F., Boucher, W., Stevens, T. J., Fogh, R. H., Pajon, A., Llinas, M., Ulrich, E. L., Markley, J. L., Ionides, J., and Laue, E. D. (2005) The CCPN Data Model for NMR Spectroscopy: Development of a Software Pipeline. *Proteins* **59**, 687-696
58. Andrec, M., Hill, R. B., and Prestegard, J. H. (1995) Amide exchange rates in *Escherichia coli* acyl carrier protein: Correlation with protein structure and dynamics. *Protein Sci.* **4**, 983-993
59. Bai, Y., Milne, J. S., Mayne, L., and Englander, S. W. (1993) Primary Structure Effects on Peptide Group Hydrogen Exchange. *Proteins* **17**, 75-86
60. Farrow, N. A., Muhandiram, R., Singer, A. U., Pascal, S. M., Kay, C. M., Gish, G., Shoelson, S. E., Pawson, T., Forman-Kay, J. D., and Kay, L. E. (1994) Backbone Dynamics of a Free and a Phosphopeptide-Complexed Src Homology 2 Domain Studied by ^{15}N NMR Relaxation. *Biochemistry* **33**, 5984-6003
61. Lakomek, N. A., Ying, J., and Bax, A. (2012) Measurement of ^{15}N relaxation rates in perdeuterated proteins by TROSY-based methods. *J. Biomol. NMR* **53**, 209-221
62. Korzhnev, D. M., Skrynnikov, N. R., Millet, O., Torchia, D. A., and Kay, L. E. (2002) An NMR Experiment for the Accurate Measurement of Heteronuclear Spin-Lock Relaxation Rates. *J. Am. Chem. Soc.* **124**, 10743-10753
63. Orekhov, V. Y., Ibraghimov, I. V., and Billeter, M. (2001) MUNIN: A new approach to multi-dimensional NMR spectra interpretation. *J. Biomol. NMR* **20**, 49-60
64. Korzhnev, D. M., Ibraghimov, I. V., Billeter, M., and Orekhov, V. Y. (2001) MUNIN: Application of three-way decomposition to the analysis of heteronuclear NMR relaxation data. *J. Biomol. NMR* **21**, 263-268
65. Tjanda, N., Wingfield, P., Stahl, S., and Bax, A. (1996) Anisotropic rotational diffusion of perdeuterated HIV protease from ^{15}N NMR relaxation measurements at two magnetic fields. *J. Biomol. NMR* **8**, 273-284
66. Dosset, P., Hus, J. C., Blackledge, M., and Marion, D. (2000) Efficient analysis of macromolecular rotational diffusion from heteronuclear relaxation data. *J. Biomol. NMR* **16**, 23-28
67. Loria, J. P., Rance, M., and Palmer, A. G. (1999) A Relaxation-Compensated Carr-Purcell-Meiboom-Gill Sequence for Characterizing Chemical Exchange by NMR Spectroscopy. *J. Am. Chem. Soc.* **121**, 2331-2332
68. Tollinger, M., Skrynnikov, N. R., Mulder, F. A. A., Forman-Kay, J. D., and Kay, L. E. (2001) Slow Dynamics in Folded and Unfolded States of an SH3 Domain. *J. Am. Chem. Soc.* **123**, 11341-11352
69. Neudecker, P., Zarrine-Afsar, A., Choy, W.-Y., Muhandiram, D. R., Davidson, A. R., and Kay, L. E. (2006) Identification of a Collapsed Intermediate with Non-native Long-range Interactions on the Folding Pathway of a Pair of Fyn SH3 Domain Mutants by NMR Relaxation Dispersion Spectroscopy. *J. Mol. Biol.* **363**, 958-976
70. Habeck, M., Rieping, W., Linge, J. P., and Nilges, M. (2004) NOE Assignment With ARIA 2.0: The Nuts and Bolts. In *Methods in Molecular Biology Vol. 278: Protein NMR Techniques* (Downing, A. K., Ed.), 2nd Ed., Humana Press, Totowa, NJ, pp. 379-402

71. Rieping, W., Habeck, M., Bardiaux, B., Bernard, A., Malliavin, T. E., and Nilges, M. (2007) ARIA2: Automated NOE assignment and data integration in NMR structure calculation. *Bioinformatics* **23**, 381-382
72. Vuister, G. W., and Bax, A. (1993) Quantitative *J* Correlation: A New Approach for Measuring Homonuclear Three-Bond $J(H^{N}H^{\alpha})$ Coupling Constants in ^{15}N-Enriched Proteins. *J. Am. Chem. Soc.* **115**, 7772-7777
73. Zhang, W., Smithgall, T., and Gmeiner, W. (1997) Three-dimensional structure of the Hck SH2 domain in solution. *J. Biomol. NMR* **10**, 263-272
74. Cavanagh, J., Fairbrother, W. J., Palmer, A. G., Rance, M., and Skelton, N. J. (2007) *Protein NMR Spectroscopy: Principles and Practice*, 2nd Ed., Elsevier Academic Press, Burlington, MA
75. Shen, Y., Delaglio, F., Cornilescu, G., and Bax, A. (2009) TALOS+: a hybrid method for predicting protein backbone torsion angles from NMR chemical shifts. *J. Biomol. NMR* **44**, 213-223
76. Shen, Y., and Bax, A. (2013) Protein backbone and sidechain torsion angles predicted from NMR chemical shifts using artificial neural networks. *J. Biomol. NMR* **56**, 227-241
77. Brünger, A. T., Adams, P. D., Clore, G. M., DeLano, W. L., Gros, P., Grosse-Kunstleve, R. W., Jiang, J. S., Kuszewski, J., Nilges, M., Pannu, N. S., Read, R. J., Rice, L. M., Simonson, T., and Warren, G. L. (1998) *Crystallography & NMR system*: A New Software Suite for Macromolecular Structure Determination. *Acta Crystallogr. D Biol. Crystallogr.* **54**, 905-921
78. Linge, J. P., and Nilges, M. (1999) Influence of non-bonded parameters on the quality of NMR structures: A new force field for NMR structure calculation. *J. Biomol. NMR* **13**, 51-59
79. Schwieters, C. D., Kuszewski, J. J., Tjandra, N., and Clore, G. M. (2003) The Xplor-NIH NMR molecular structure determination package. *J. Magn. Reson.* **160**, 65-73
80. Brünger, A. T. (1992) *X-PLOR Version 3.1. A System for X-ray Crystallography and NMR*, Yale University Press, New Haven, CT
81. Laskowski, R. A., MacArthur, M. W., Moss, D. S., and Thornton, J. M. (1993) *PROCHECK*: a program to check the stereochemical quality of protein structures. *J. Appl. Cryst.* **26**, 283-291
82. Chen, V. B., Arendall, W. B., Headd, J. J., Keedy, D. A., Immormino, R. M., Kapral, G. J., Murray, L. W., Richardson, J. S., and Richardson, D. C. (2010) *MolProbity*: all-atom structure validation for macromolecular crystallography. *Acta Crystallogr. D Biol. Crystallogr.* **66**, 12-21
83. Doreleijers, J. F., Sousa da Silva, A. W., Krieger, E., Nabuurs, S. B., Spronk, C. A. E. M., Stevens, T. J., Vranken, W. F., Vriend, G., and Vuister, G. W. (2012) CING: an integrated residue-based structure validation program suite. *J. Biomol. NMR* **54**, 267-283
84. Lindorff-Larsen, K., Piana, S., Palmo, K., Maragakis, P., Klepeis, J. L., Dror, R. O., and Shaw, D. E. (2010) Improved side-chain torsion potentials for the Amber ff99SB protein force field. *Proteins* **78**, 1950-1958
85. Jorgensen, W. L., Chandrasekhar, J., Madura, J. D., Impey, R. W., and Klein, M. L. (1983) Comparison of simple potential functions for simulating liquid water. *J. Chem. Phys.* **79**, 926-935
86. Wang, J., Wolf, R. M., Caldwell, J. W., Kollman, P. A., and Case, D. A. (2004) Development and Testing of a General Amber Force Field. *J. Comput. Chem.* **25**, 1157-1174
87. Sousa da Silva, A. W., and Vranken, W. F. (2012) ACPYPE - AnteChamber PYthon Parser interfacE. *BMC Research Notes* **5**, 367
88. Abraham, M. J., Murtola, T., Schulz, R., Páll, S., Smith, J. C., Hess, B., and Lindahl, E. (2015). GROMACS: High performance molecular simulations through multi-level parallelism from laptops to supercomputers. *SoftwareX* **1-2**, 19-25
89. Hoover, W. G. (1985) Canonical dynamics: Equilibrium phase-space distributions. *Phys. Rev. A* **31**, 1695-1697
90. Parrinello, M., and Rahman, A. (1981) Polymorphic transitions in single crystals: A new molecular dynamics method. *J. Appl. Phys.* **52**, 7182-7190
91. Darden, T., York, D., and Pedersen, L. (1993) Particle mesh Ewald: An $N\cdot\log(N)$ method for Ewald sums in large systems. *J. Chem. Phys.* **98**, 10089-10092

92. Hess, B. (2008) P-LINCS: A Parallel Linear Constraint Solver for Molecular Simulation. *J. Chem. Theory Comput.* **4**, 116-122
93. Waterhouse, A. M., Procter, J. B., Martin, D. M. A, Clamp, M. and Barton, G. J. (2009) Jalview Version 2 - a multiple sequence alignment editor and analysis workbench. *Bioinformatics* **25**, 1189-1191
94. Kabsch, W., and Sander, C. (1983) Dictionary of Protein Secondary Structure: Pattern Recognition of Hydrogen-Bonded and Geometrical Features. *Biopolymers* **22**, 2577-2637

TABLES

TABLE 1

Statistics of the NMR ensemble (n = 10)

Conformational restraints	
NOE distance restraints	
Total	1162
Intraresidual (i = j)	202
Sequential (|i − j| = 1)	387
Medium range (1 < |i − j| < 5)	266
Long range (|i − j| ≥ 5)	307
Ambiguous	57
Hydrogen bond distance restraints	102
Dihedral angle restraints	214
Residual restraint violations	
Average number of distance restraint violations per structure	
> 0.1 Å	7.8
> 0.3 Å	0.2 (max. 0.34 Å)
Average number of dihedral angle restraint violations	
> 1°	10.2
> 3°	0.4 (max 3.77°)
Atomic RMSDs from the average structure[a]	
Backbone atoms	0.72 Å ± 0.10 Å
Heavy atoms	1.30 Å ± 0.12 Å
MolProbity (82) Ramachandran statistics	
Favored regions	91.6%
Allowed regions	99.2%
Model content	
Total no. of residues	126
Ordered residue range	18-120
BMRB accession number	26603
PDB ID code	2NCN

[a] Ordered residue range (18-120)

FIGURE LEGENDS

FIGURE 1. Sequence alignment of *S. cerevisiae* Atg8 (Uniprot P38182) and the canonical human homologues GABARAP (O95166), GABARAPL1/GEC1 (Q9H0R8), GABARAPL2/GATE-16 (P60520), and LC3A (Q9H492), LC3B (Q9GZQ8), and LC3C (Q9BXW4). Highly conserved residues are highlighted in shades of gray; darker shading indicates higher conservation. All members of the Atg8 family can be cleaved by the cysteine protease family ATG4 after the conserved Gly126, which can subsequently be conjugated to a phospholipid moiety for membrane anchoring. The alignment was performed using Jalview version 2 (93).

FIGURE 2. Solution structure of LC3C shown as a superposition of the backbone traces of the 10 accepted structures with a schematic representation of the secondary structure elements as identified with DSSP (94). The tertiary structure of LC3C consists of three α-helices (α_2: Leu19 to Lys32, α_3: Met66 to Arg76, α_4: Met101 to Tyr108; red) and a central β-sheet of four β-strands (β_1: Lys36 to Arg43, β_2: Lys57 to Pro61, β_3: Tyr86 to Val89, β_4: Val115 to Ala120; blue). In the ubiquitin-like core of the protein the 10 accepted structures are in excellent agreement, whereas the amino (N) and carboxy (C) termini as well as some of the loops are highly flexible in solution. The location of the two hydrophobic pockets is indicated by hp1 and hp2. The overlay was performed using PyMOL (The PyMOL Molecular Graphics System, Version 1.7.2.1, Schrödinger, LLC).

FIGURE 3. $\{^1H\}^{15}N$ heteronuclear NOE values (**A**), generalized order parameters S^2 of the sub-nanosecond backbone amide motion (**B**), atomic RMSDs from the average structure (**C**), and distribution of NOEs (**D**). $\{^1H\}^{15}N$ values below 0.65 (dashed horizontal line) indicate increased internal mobility (29). Experimental order parameters S^2 obtained from ^{15}N relaxation analysis (blue) are compared with order parameters predicted from the Random Coil Index (RCI) (32), S_{RCI}^2 (red circles), calculated with the default parameters as implemented in TALOS-N (75,76). Backbone RMSDs are indicated by blue circles, side-chain heavy atom RMSDs by red squares. The regular secondary structure elements are indicated above the graph.

FIGURE 4. ^{15}N transverse (**A**) and longitudinal (**B**) relaxation rates and $\{^1H\}^{15}N$ heteronuclear NOE values (**C**) measured at 800 MHz and 20.0°C. Dashed horizontal lines in (**A**) and (**B**) represent the average values over the ordered region (residues 18-120). $\{^1H\}^{15}N$ values below 0.65 (dashed horizontal line in (**C**)) indicate increased internal mobility (29). The regular secondary structure elements are indicated above the graph.

FIGURE 5. The amino-terminal polyproline II motif of LC3C shown as a superposition of the 10 accepted structures. Only the backbone atoms of the two adjacent residues, Met1 and Gln5, are shown. Carbon, nitrogen, and oxygen atoms are color-coded green, blue, and red, respectively. (**A**) Side view, (**B**) view from Met1 along the helix axis showing the typical cloverleaf-like arrangement of the proline rings due to the three-fold symmetry of the left-handed PPII helix. Pairwise alignment of backbone atoms from Pro2 to Pro4 was performed using PyMOL (The PyMOL Molecular Graphics System, Version 1.7.2.1, Schrödinger, LLC).

FIGURE 6. Logarithmic plot of the protection factors, $PF = k_{int}/k_{ex}$, calculated from the apparent backbone amide proton/deuteron (H/D) exchange rates, k_{ex}, as measured in a series of $[^1H\text{-}^{15}N]$ HSQC experiments at 20.0°C. Amide protons with protection factors below about 1×10^2 exchange in less than half an hour and hence too rapidly to be observed with sufficient resonance intensity for quantification. By contrast, amide protons involved in hydrogen bonding in the regular secondary structure elements, which are indicated above the graph, are highly protected from solvent exchange ($PF \approx 5\times10^2$ to 3×10^4).

FIGURE 7. Comparison of a schematic representation of the secondary structure elements of the average solution structure of LC3C (green) with the crystal structures of LC3C in the free form (14; PDB 3WAM, yellow; backbone RMSD 0.65 Å for residues Ser18 to Ala120) as well as in complex with NDP52 (15; PDB 3VVW, red; 0.89 Å) and in complex with Atg13 (14; PDB 3WAP, blue; 1.09 Å). The overlay and

the calculation of backbone RMSDs were performed using PyMOL (The PyMOL Molecular Graphics System, Version 1.7.2.1, Schrödinger, LLC).

FIGURE 8. Overlay of sections of the [^{1}H-^{15}N] HSQC spectra of [U-^{13}C,^{15}N] LC3C before (black) and 3.5 h (red) and 7.0 h (green) after incubation with PKA to monitor the progress of *in vitro* phosphorylation. (**A**) Intense resonance signals of Met1 and Lys6 did not shift, while the shift of the resonance of Glu25 could be traced (open arrow) and the resonance of Arg22 disappears. (**B**) The populations of the split signal of Phe13 in the unphosphorylated state (black) shifted towards the minor peak position (filled arrow), while the resonance of Val26 could be traced to a new peak position (open arrow). (**C**) The intensities of the resonances of Ser18 and Ala20 decreased within 3.5 h and could not be traced to newly emerging peaks in the vicinity, in contrast to Glu123 (filled arrow) and (**D**) Glu111. The resonance of Met97 was not influenced by PKA reaction progress.

FIGURE 9. Electrostatic interactions of the acidic cluster formed by the side-chains of Asp110, Glu111, and Asp112 with helix α_2 residues Arg22 and Gln23 in the crystal structure of LC3C(8-125) (14; PDB 3WAM; hydrogen atoms were added with PyMOL). The backbone amide proton of Ile21 forms an N-capping motif with the side-chain hydroxyl oxygen of phosphorylation target Ser18 (dashed line). The figure was created with PyMOL (The PyMOL Molecular Graphics System, Version 1.7.2.1, Schrödinger, LLC).

FIGURES

FIGURE 1

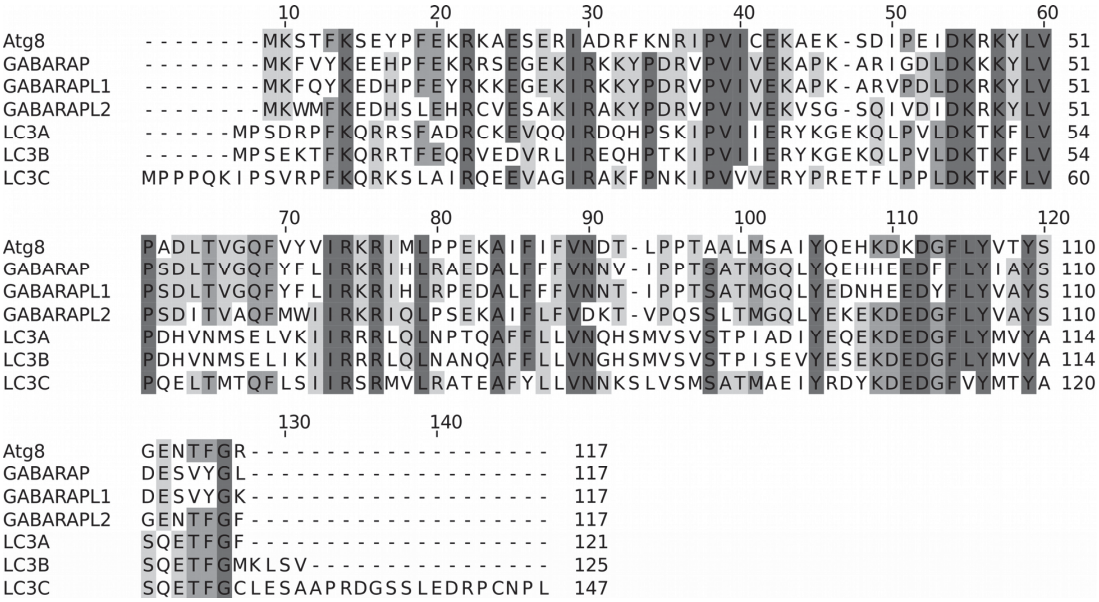

FIGURE 2

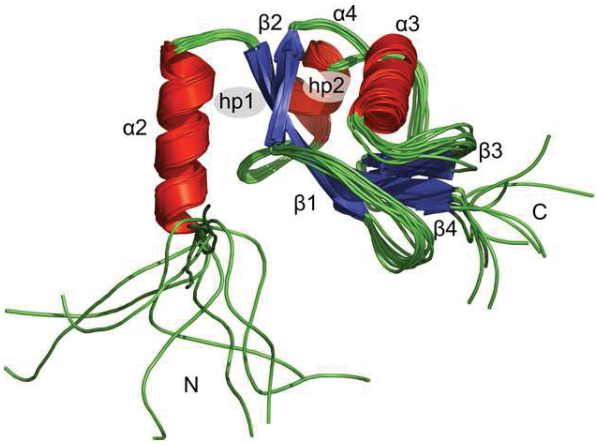

FIGURE 3

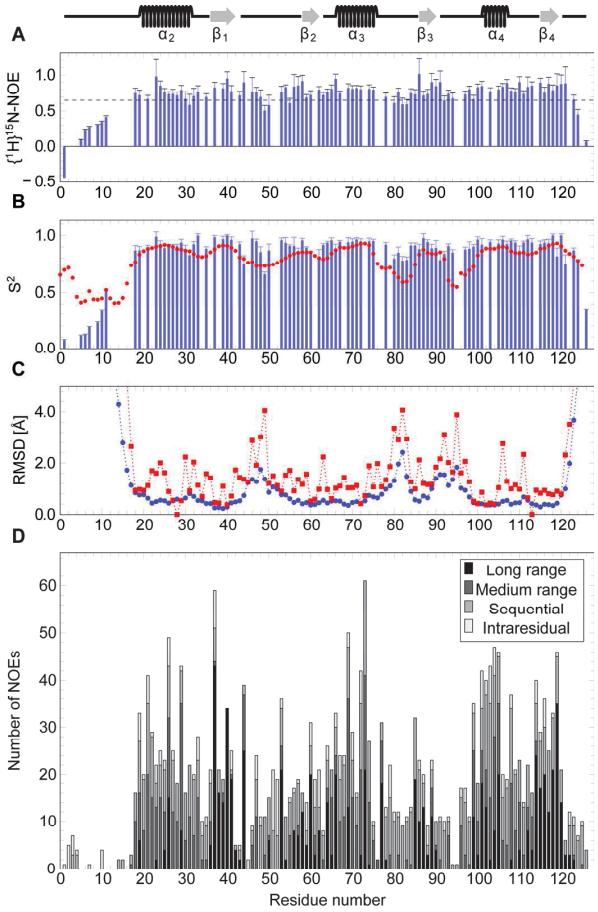
A
α2
β1
β2
α3
β3
α4
β4
{1H}15N-NOE
B
S2
C
RMSD [Å]
D
Long range
Medium range
Sequential
Intraresidual
Number of NOEs
Residue number

FIGURE 4

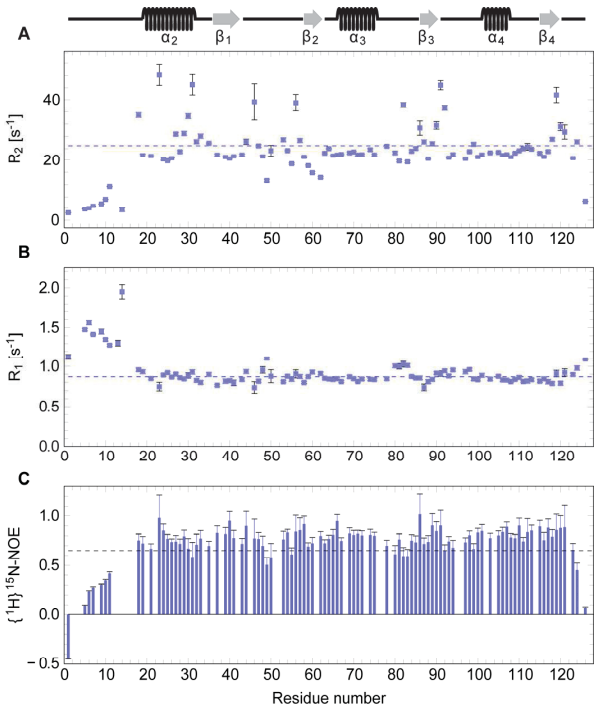

FIGURE 5

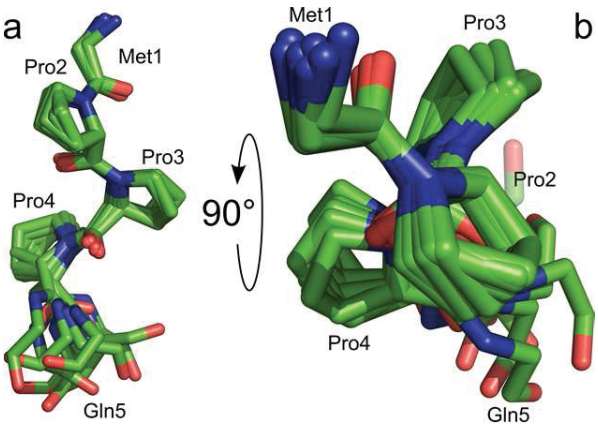

FIGURE 6

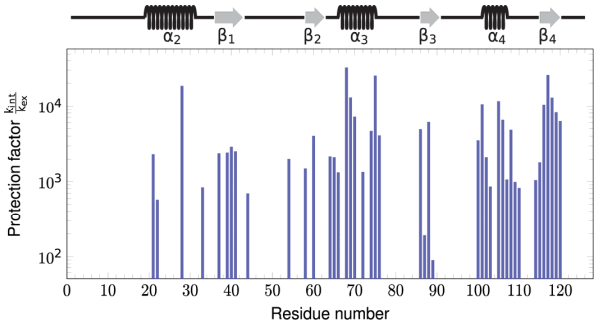
α2
β1
β2
α3
β3
α4
β4
Protection factor $\frac{k_{int}}{k_{ex}}$
10^4
10^3
10^2
0
10
20
30
40
50
60
70
80
90
100
110
120
Residue number

FIGURE 7

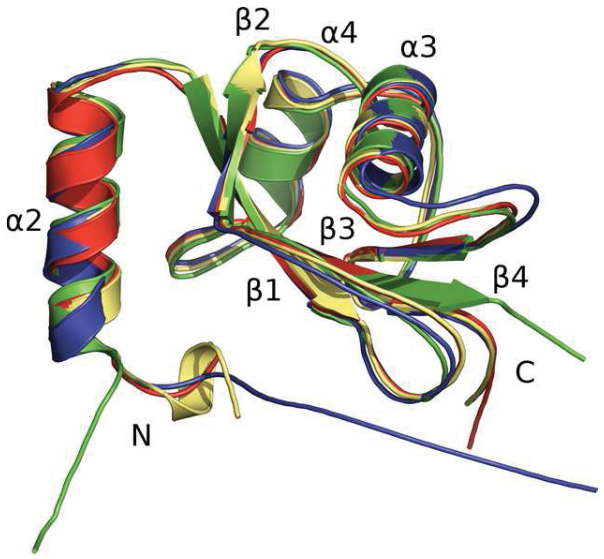

FIGURE 8

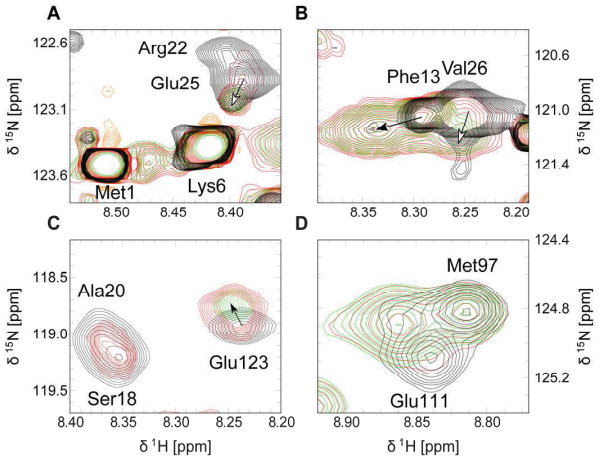
A
B
C
D
Arg22
Glu25
Met1
Lys6
Phe13
Val26
Ala20
Ser18
Glu123
Met97
Glu111
δ 15N [ppm]
δ 1H [ppm]

FIGURE 9

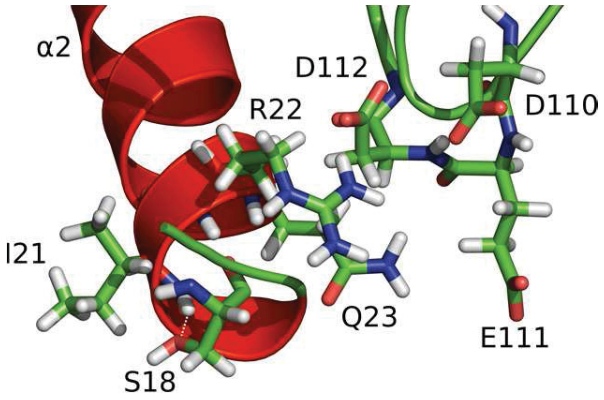

SUPPORTING INFORMATION

SUPPORTING TABLES

TABLE S1

Overview of molecular dynamics parameters used for structure calculation by CNS 1.21

Parameter	Value
TAD high temperature	10000 K
TAD time-step factor	9.0
Cartesian high temperature	2000 K
Cartesian 1st iteration	0
Time-step	3 fs
Cool1 final temperature	1000 K
Cool2 final temperature	50 K
High-temp steps	10000
Refine steps	4000
Cool1 steps	20000
Cool2 steps	20000

SUPPORTING FIGURES

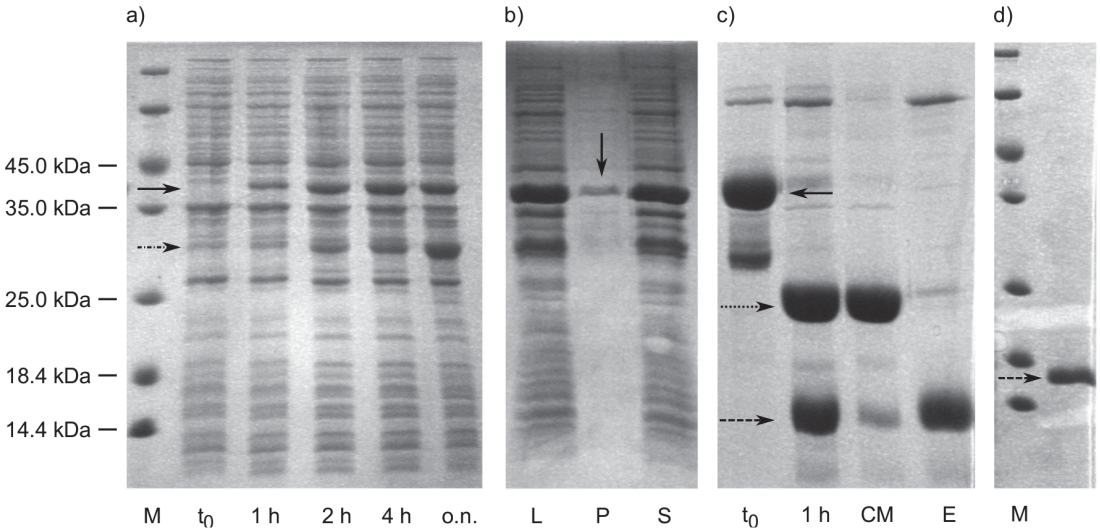

FIGURE S1. Purification of LC3C documented by SDS-PAGE. (**a**) Expression of GST-LC3C fusion protein (41.4 kDa, marked by arrow) at 25°C. M - protein marker, t_0 - before induction, 1 h/2 h/4 h - time points after induction, and o.n. - overnight expression. (**b**) Cell lysis, L - whole cell lysate, P - unsoluble pellet after centrifugation of lysate, S - supernatant. (**c**) On-column hydrolysis of GST-LC3C fusion protein by bovine thrombin at room temperature. t_0 - column material with bound GST-LC3C fusion protein (marked by arrow) before addition of thrombin, 1 h - resuspended column material one hour after addition of thrombin (GST marked by dotted arrow, LC3C marked by dashed arrow), CM - remaining column material after elution, E - elution fraction containing cleaved LC3C. (**d**) Purified LC3C after cation exchange and size exclusion chromatography steps (marked by dashed arrow).

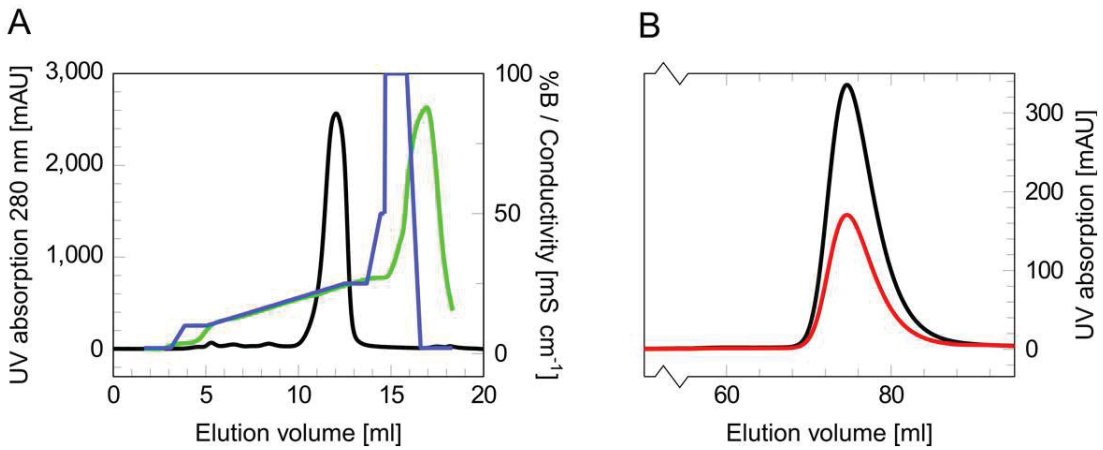

FIGURE S2. Overview of LC3C chromatographic purification. (**A**) Cation exchange chromatogram of LC3C (Resource S column in a buffer of 20 mM PIPES at pH 6.0 at a flow rate of 1.5 ml/min at room temperature). UV absorption recorded at 280 nm (black), high-salt gradient from 0.0 M (0% elution buffer B) to 1.0 M NaCl (100% elution buffer B consisting of 1.0 M NaCl, 20 mM PIPES, pH 6.0) (blue), and conductivity of eluent (green). (**B**) Size exclusion chromatogram of LC3C (Superdex 75 16/60 at a flow rate of 1.5 ml/min at 8°C). UV absorption recorded at 280 nm and 320 nm (black and red, respectively).

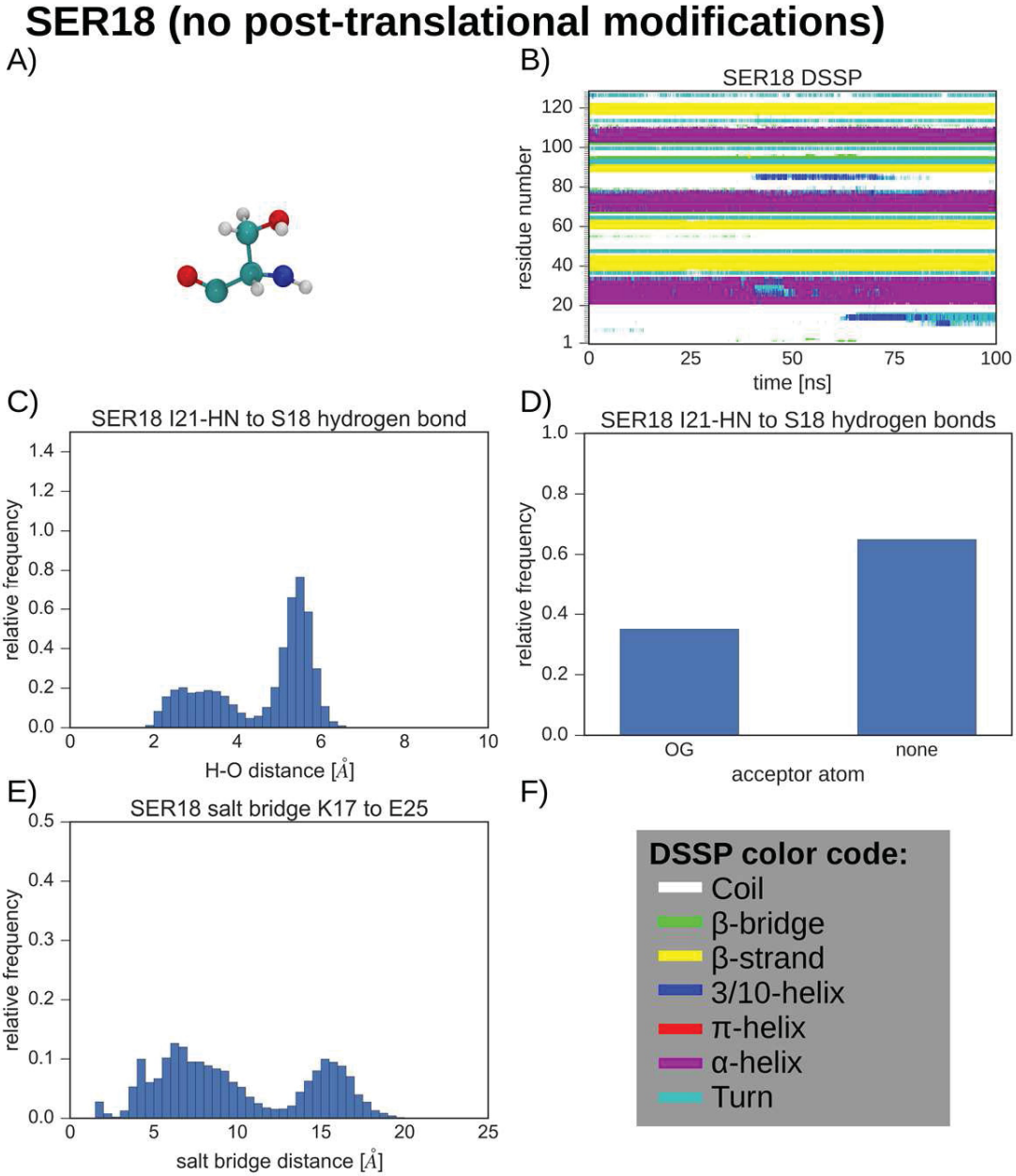

FIGURE S3. Analysis of the MD trajectory of unmodified LC3C. (**A**) Unmodified serine residue in ball-and-stick representation (C: cyan, N: blue, O: red, H: white). (**B**) Secondary structure elements along the MD trajectory as identified with DSSP (94; see color code at the bottom). (**C**) Histogram of the distance between the backbone amide proton of Ile21 and the hydroxyl oxygen of Ser18. (**D**) Histogram of the hydrogen bond acceptor for the amide proton of Ile21 (OG: Ser18 Oγ). (**E**) Histogram of the salt bridge distance between Lys17 and Glu25. All histograms have been normalized to unit area.

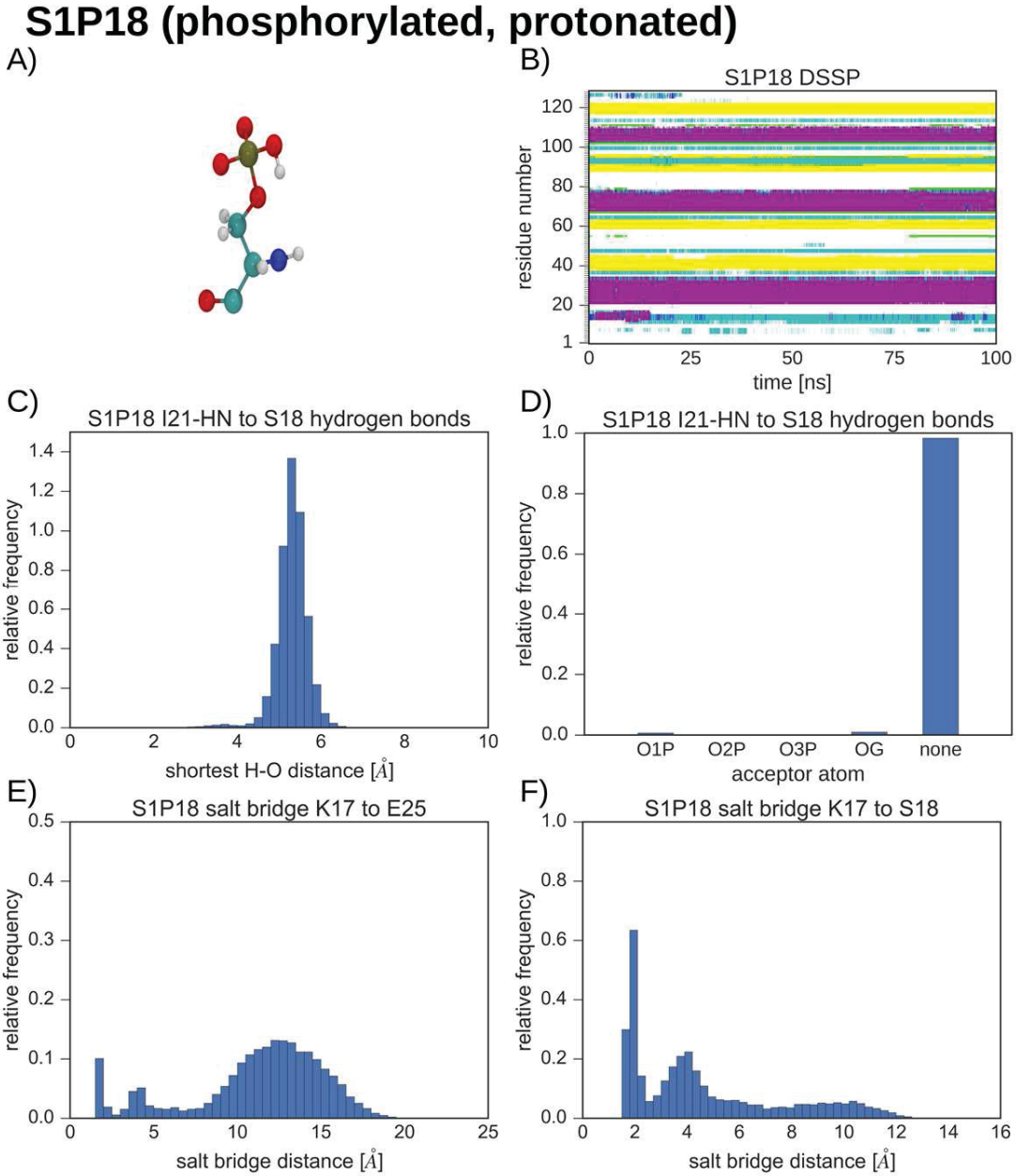

FIGURE S4. Analysis of the MD trajectory of phosphorylated LC3C in the monoanionic state. (**A**) Protonated phosphoserine residue in ball-and-stick representation. (**B**) Secondary structure elements along the MD trajectory as identified with DSSP. (**C**) Histogram of the shortest distance between the backbone amide proton of Ile21 and one of the four phosphate oxygens of pSer18^{-}. (**D**) Histogram of the hydrogen bond acceptor for the amide proton of Ile21 (OG: pSer18^{-} Oγ, O1P/O2P/O3P: pSer18^{-} terminal phosphate oxygens). (**E**) Histogram of the salt bridge distance between Lys17 and Glu25. (**F**) Histogram of the salt bridge distance between Lys17 and pSer18^{-}. See legend to Fig. S3 for details.

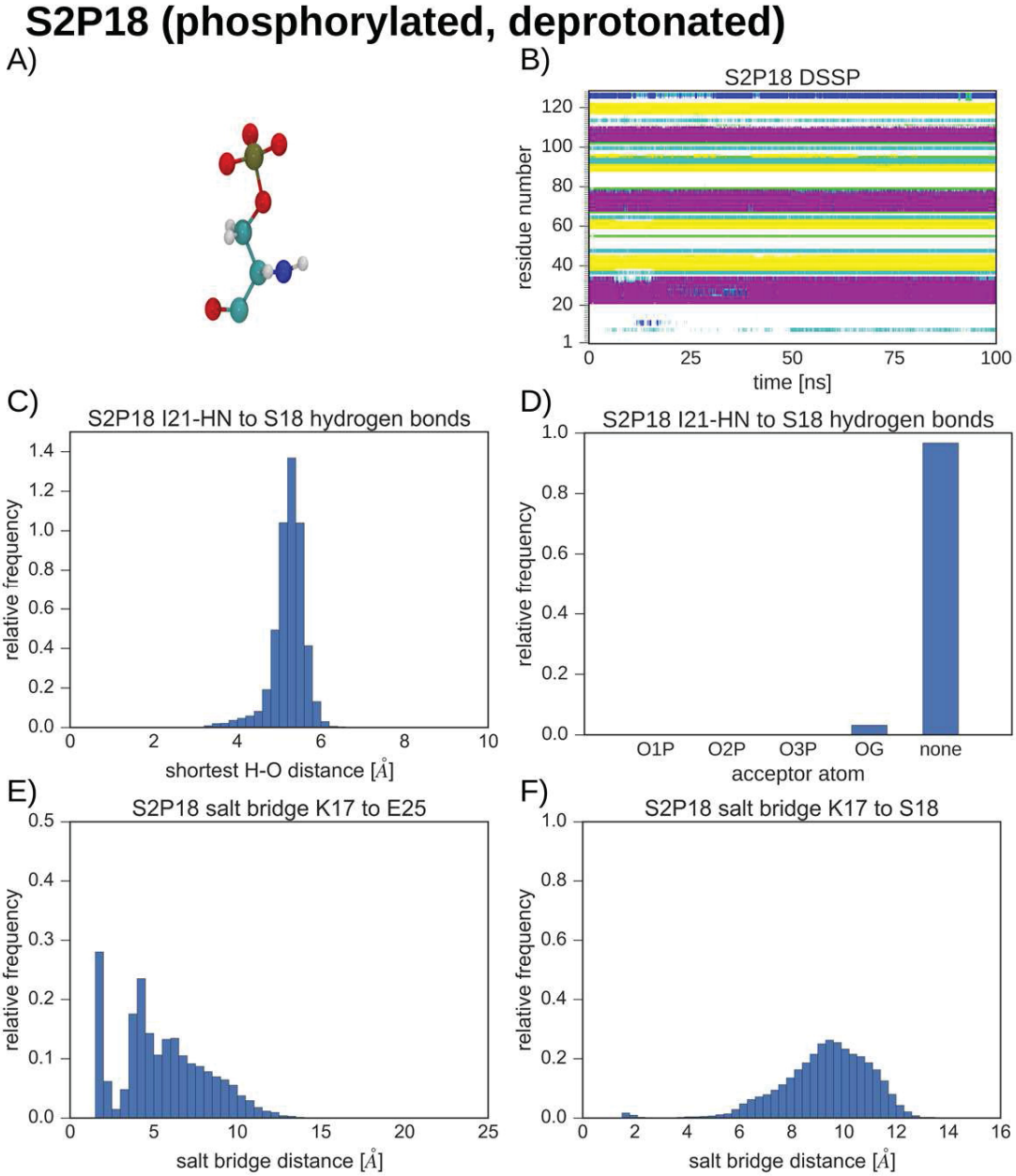

FIGURE S5. Analysis of the MD trajectory of phosphorylated LC3C in the dianionic state. (**A**) Deprotonated phosphoserine residue in ball-and-stick representation. (**B**) Secondary structure elements along the MD trajectory as identified with DSSP. (**C**) Histogram of the shortest distance between the backbone amide proton of Ile21 and one of the four phosphate oxygens of $pSer18^{2-}$. (**D**) Histogram of the hydrogen bond acceptor for the amide proton of Ile21 (OG: $pSer18^{2-}$ Oγ, O1P/O2P/O3P: $pSer18^{2-}$ terminal phosphate oxygens). (**E**) Histogram of the salt bridge distance between Lys17 and Glu25. (**F**) Histogram of the salt bridge distance between Lys17 and $pSer18^{2-}$. See legend to Fig. S3 for details.

4. Summary

Autophagy is a major lysosomal catabolic pathway essential for cellular homeostasis in eukaryotes. Cytoplasmatic cargo destined for autophagic degradation may comprise single proteins or protein aggregates, invading pathogens, and even entire organelles. In macroautophagy, the most intensely studied autophagic pathway, cargo is engulfed by a cup-shaped, growing double-membrane structure termed phagophore. Elongation of this autophagosomal membrane and sequestering of autophagic cargo is assisted by Atg8-like proteins. The lastly discovered and least well characterised member of the human LC3-like protein subfamily, LC3C, was the focus of this work.

Integral to a comprehensive understanding of a protein's function is knowledge of its three-dimensional structure. Therefore, the solution structure of LC3C was determined by liquid-state NMR spectroscopy. To this end, a cloning procedure, expression and purification schemes were established to procure pure and isotopically ^{15}N- and / or ^{13}C-labelled LC3C. Additionally, protein buffer, and NMR measurement conditions had to be established and optimised to generate highly concentrated (up to 760 μM), stable LC3C protein samples for data acquisition in multidimensional, heteronuclear NMR experiments. Subsequently, backbone and side-chain resonance assignments were determined and deposited in the BMRB (Krichel et al., 2016; BMRB accession ID: 26603).

The determination of LC3C's three-dimensional structure followed acquisition of NOESY data, which was translated into distance restraints in conjunction with residue-specific chemical shift assignments. The overall fold of LC3C is in accordance with other LC3-like paralogues, consisting of an ubiquitin-like core structure and an additional amino-terminal α-helix. Of special interest were the residues preceding this α-helix, which are–compared to other LC3-like proteins–in a state of higher structural dynamics or disorder as was shown through relaxation and heteronuclear NOE experiments. Similiar results in regard to its dynamic behaviour were obtained for LC3C's

carboxy-terminus.

While LC3C is structurally closely related to other LC3 paralogues, its cellular activity may be decisively modulated by post-translational modifications. Therefore, the phosphorylation of LC3C by PKA was studied. To this end, *in-vitro* phosphorylation experiments were optimised and phosphorylation of LC3C's PKA target residue (S18) observed by [^{1}H-^{15}N] HSQC NMR spectroscopy. This residue is also involved in the N-capping motif of the amino-terminal helix α2. Upon phosphorylation of S18, S18 to Q23, residues A31 to F33 (connecting the α2-helix to the ubiquitin-like core), and residues D110 to D112 (establishing electrostatic interactions to said α2-helix) experienced significant chemical shift changes. This might indicate an increased structural mobility of LC3C's amino-terminal helix α2 upon phosphorylation of S18. Overall, these findings provide the first indication of a post-translational phosphorylation modulating the structure of an LC3-like protein.

5. Zusammenfassung

Die Autophagie stellt einen katabolischen Stoffwechselweg eukaryotischer Zellen dar, der zum Erhalt zellulärer Homöostase beiträgt. Abbauziele der Autophagie umfassen sowohl zytosolische Proteine und Proteinaggregate, als auch vollständige Zellorganellen und Pathogene. Die Prozesse der sogenannten Makroautophagie gehören zu den umfänglichst untersuchten autophagischen Stoffwechselwegen. Wird die Makroautophagie aktiviert, formt sich eine schalenartige Doppelmembran aus (Phagophore), die die autophagischen Abbauziele umfasst und letztendlich einschließt. An dem Wachstum der Phagophore sowie der Rekrutierung von Abbauzielen sind Atg8-artige Proteine entscheidend beteiligt. In menschlichen Zellen sind Atg8-artige Proteine in die GABARAP- und LC3-Subfamilien gegliedert. Das nur wenig erforschte und zuletzt entdeckte humane LC3-artige Protein LC3C stellt den Mittelpunkt dieser Arbeit dar.

Für das vollständige Verständnis der Funktion eines Proteins ist die Kenntnis dessen dreidimensionaler Struktur unerlässlich. Als strukturaufkärende Methode wurde NMR-Spektroskopie herangezogen, die es ermöglichte den räumlichen Aufbau des LC3C-Proteins in Lösung zu ermitteln. Dies erforderte sowohl die Etablierung und Optimierung eines Klonierungs-, als auch von heterologen Expressions- und biochemischen Reinigungsprotokollen. Als Resultat dieser Arbeiten konnte ^{15}N- und / oder ^{13}C-Isotopen-markiertes LC3C gewonnen werden. Weiterhin wurden Proteinpuffer- und NMR-Messbedingungen entwickelt und verfeinert, welche die Aufnahme von multidimensionalen, heteronuklearen NMR-Datensätzen erlaubten. In der Folge konnten die Resonanzen von Rückgrat- und Seitenkettenatomen zugeordnet und publiziert werden (Krichel et al., 2016; Identifikationsnummer des BMRB-Eintrags: 26603).

Die Errechnung der dreidimensionalen LC3C-Struktur erfolgte aufgrund atomarer Abstandsinformationen aus NOESY-Experimenten, die unter Einbeziehung der Restspezifischen Resonanzzuordnung interpretiert werden konnten. Es zeigte sich, dass die Faltung von LC3C derjenigen anderer LC3-artiger Paraloge entspricht, bestehend aus einer Ubiquitin-ähnlichen Kernstruktur und einer Atg8-typischen, amino-

terminalen α-Helix. In dieser Arbeit wurde besonderes Augenmerk auf die Aminosäurereste gelegt, die der amino-terminalen α-Helix vorgelagert sind. Diese zeigen im Falle von LC3C, im Gegensatz zu anderen paralogen LC3-artigen Proteinen, eine erhöhte Dynamik, was durch Relaxations- und heteronukleare NOE-Experimente gezeigt werden konnte. Vergleichbar dynamische Eigenschaften wurden auch für die carboxy-terminalen Reste festgestellt.

Während die dreidimensionale Struktur von LC3C derjenigen anderer paraloger Proteine nahe verwandt ist, ist die zelluläre Aktivität vermutlich Paralog-spezifisch durch posttranslationale Phosphorylierung moduliert. Unter dieser Annahme wurde die *In-vitro* Phosphorylierung des LC3C-Zielrestes S18 mittels der Proteinkinase PKA durch [^{1}H-^{15}N] HSQC-NMR-Spektroskopie verfolgt. Von besonderem Interesse ist S18 zusätzlich, da dessen Seitenketten-Hydroxylgruppe das Sekundärstruktur-stabilisierende *N-capping*-Motiv der amino-terminalen α-Helix ausbildet. Es konnte anhand von [^{1}H-^{15}N] HSQC-Experimenten gezeigt werden, dass mit der Phosphorylierung von S18 signifikante Änderungen in der chemischen Verschiebung der Resonanzsignale des eigenen Amid-Protons von S18 und der sequentiell direkt benachbarten Reste der amino-terminalen α-Helix erfolgten. Außerdem wurde eine signifikante Beeinflussung der Resonanzsignale der Reste A31 bis F33, die eine Verknüpfung zwischen amino-terminaler α-Helix und Ubiquitin-Kernstruktur bilden, und der Reste D110 bis D112 beobachtet. Die zuletzt genannten Aminosäuren sind vermutlich eingebunden in Tertiärstruktur-stabilisierende elektrostatische Wechselwirkungen mit Seitenketten der zu S18 direkt benachbarten Reste R22 und Q23. Die Beeinflussung der Wechselwirkung könnte auf eine erhöhte Dynamik der amino-terminalen α-Helix hindeuten. Damit implizieren die Ergebnisse dieser Arbeit zudem erstmalig eine mögliche Modulation der räumlichen Struktur eines LC3-artigen Proteins als Folge einer posttranslationalen Phosphorylierung.

6. Experimental

6.1. Materials

6.1.1. Chemicals

All chemicals were of *pro analysi* (p.a.) quality or a higher purity grade. Chemicals not listed in Table 6.1 were purchased from AppliChem (Darmstadt, Germany), Merck KGaA (Darmstadt, Germany), Roth (Karlsruhe, Germany), and Sigma-Aldrich (Taufkirchen, Germany).

6.1.2. Enzymes

Enzymes (see Table 6.2) were stored at -20 °C and exposed to room temperature (RT) only for brief periods. Lyophilised bovine thrombin (Merck KgaA, Darmstadt, Germany) was stored at 6 °C.

6.1.3. Biochemical Kits

Biochemical kits used to purify DNA and site-directed mutagenesis are listed in Table 6.3 and were used in accordance with manufacturer's guidelines.

6.1.4. Crystallisation Kits

Commercially available kits used for sparse matrix or grid screening of protein crystallisation conditions are listed in Table 6.4. Kits were delivered as 10 ml stock solutions and were transferred by a pipetting robot (Freedom EVO, Tecan, Männedorf, Switzerland) into 1 ml deep well plates, sealed, and stored in accordance with manufacturer's guidelines.

Table 6.1.: Research chemicals.

Agarose MP	AppliChem, Darmstadt, Germany
Ammonium chloride [U-15N, 99%]	Cambridge Isotope Laboritories, Tewksbury, USA
Ampicillin	AppliChem, Darmstadt, Germany
Antifoam A	Sigma-Aldrich, Taufkirchen, Germany
Benzamidine sepharose	GE Healthcare, Freiburg, Germany
Chloramphenicol	Roth, Karlsruhe, Germany
Complete EDTA-free protease inhibitor	Roche, Mannheim, Germany
Dideuterium oxide ^2H_2O	Sigma-Aldrich, Taufkirchen, Germany
dNTP mix	Merck KGaA,Darmstadt, Germany
Ethylenediaminetetraacetic acid (EDTA)	AppliChem, Darmstadt, Germany
D-Glucose [U-13C, 99%]	Cambridge Isotope Laboritories, Tewksbury, USA
Glutathione, reduced	Merck KGaA,Darmstadt, Germany
Glutathione-sepharose 4B	GE Healthcare, Freiburg, Germany
Glycerol [U-D8, 99%]	Euriso-top, Gif-sur-Yvette, France
M9 trace elements	Merck KGaA,Darmstadt, Germany
2-Mercaptoethanol	Sigma-Aldrich, Taufkirchen, Germany
Phenylmethanesulfonyl fluoride (PMSF)	Sigma-Aldrich, Taufkirchen, Germany
Pierce Unstained Protein Molecular Weight Marker 26610	Thermo Scientific, Schwerte, Germany
1,4-Piperazinediethanesulfonic acid (PIPES)	AppliChem, Darmstadt, Germany
Triton X-100	Sigma-Aldrich, Taufkirchen, Germany
Tryptone	AppliChem, Darmstadt, Germany
Vitamins for vitamin solution	Merck KGaA,Darmstadt, Germany
Yeast extract	AppliChem, Damrstadt, Germany

Table 6.2.: Commercially obtained enzymes.

AccuPrime Pfx	Life Technologies, Thermo Fisher Scientific, Schwerte, Germany
*Bam*HI	Fermentas, St. Leon-Rot, Germany
cAMP-dependent Protein Kinase (PKA), murine, catalytic subunit	NEB, Frankfurt a. M., Germany
DNAse1	Merck KGaA,Darmstadt, Germany
*Not*I	Fermentas, St. Leon-Rot, Germany
Pfu polymerase	Strategene, Waldbronn, Germany
Shrimp alkaline phosphatase (SAP)	Fermentas, St. Leon-Rot, Germany
T4 DNA ligase	Fermentas, St. Leon-Rot, Germany
Taq DNA polymerase	Fermentas, St. Leon-Rot, Germany
Taq DNA polymerase	NEB, Frankfurt a.M., Germany
Thermosensitive alkaline phosphatase (FastAP)	Fermentas, St. Leon-Rot, Germany
Thrombin, bovine	Merck KGaA,Darmstadt, Germany

6.1.5. Buffers & Solutions

All solutions and buffers were prepared with Milli-Q-Biocell water (Millipore, Schwalbach, Germany) and prepared at RT unless stated otherwise. Non-autoclavable solutions were sterilised by filtration with sterile 0.2 μm cellulose nitrate filters (Sartorius, Göttingen, Germany) in sterile Nalgene filter devices (Thermo Scientific, Schwerte, Germany). The pH of buffers was adjusted by calibrated FE20 pH-meters (Mettler-Toledo, Gießen, Germany) at RT. Chromatography buffers were degassed under constant stirring (1 h, circa 50 mbar, RT).

6.1.6. Growth Media & Antibiotics

Lysogeny broth (LB) growth media, SOB (super optimal broth), SOC (super optimal broth with catabolite repression), $MgSO_4$, $CaCl_2$, glucose and M9 salt stock solutions were sterilised by autoclaving (120 °C, 20 min, 1.5 bar) and stored at RT. Trace ele-

Table 6.3.: Biochemical kits for DNA purification and site-directed mutagenesis.

NucleoBond PC 100	Macherey-Nagel, Düren, Germany
NucleoSpin Gel and PCR Clean-up	Macherey-Nagel, Düren. Germany
Qiagen Plasmid Plus midi kit	Qiagen, Hilden, Germany
QuikChange II XL site-directed mutagenesis kit	Stratagene, Waldbronn, Germany

Table 6.4.: Crystallisation screens.

Additive Screen HT	Hampton Research, Aliso Viejo, USA
AmSO4 Suite	Qiagen, Hilden, Germany
Crystal Screen I, II	Hampton Research, Aliso Viejo, USA
JCSG Core I-IV	Qiagen, Hilden, Germany
Low Ionic Strength	Sigma-Aldrich, Munich, Germany
MPD Suite	Qiagen, Hilden, Germany
PEG I, II Suite	Qiagen, Hilden, Germany
PEG Grid Screening	Sigma-Aldrich, Munich, Germany
Wizard I, II	Emerald BioSystems; now Rigaku, Seattle, USA

ment solution (TS), vitamin solution, and a Fe_2Cl_3 and thiamine hydrochloride solution used to supplement M9 minimal medium (Sambrook and Russell, 2001) were sterilised by filtration (sterile 0.2 μm syringe filters, Sartorius, Göttingen, Germany) and stored at -80 °C, with the exception of TS, which was stored at 6 °C.

The most limiting factor concerning achievable cell density of bacterial shaking cultures is often insufficient concentrations of magnesium ions preent in commercially available tryptone mixtures used for LB growth media (Studier, 2005). Therefore, LB medium for protein expression experiments was supplemented with 2 mM $MgSO_4$. All selective media contained either ampicillin (Amp, 100 μg/ml) and / or chloramphenicol (Cam, 34 μg/ml).

Table 6.5.: Protein buffers used for protein purification and NMR spectroscopy.

Lysis buffer	TBS pH 9.0, 5% (v/v) glycerol, 5 mM 2-mercaptoethanol, 20 μg/ml DNAse1, 0.1% (v/v) Triton-X100, complete EDTA-free protease inhibitor (one tablet per 100 ml buffer)
Wash buffer	TBS pH 8.0, 5% (v/v) glycerol, 1 mM 2-mercaptoethanol, 5 mM EDTA, 0.01% (v/v) Triton-X100
Thrombin reaction buffer	TBS pH 8.0, 5% (v/v) glycerol, 0.01% (v/v) Triton-X100
Glutathione elution buffer	200 mM Glutathione, 100 mM NaCl, pH 8.0
Dialysis buffer	20 mM PIPES, 50 mM NaCl, 0.5% (v/v) glycerol, pH 6.0
Ion exchange buffer A	20 mM PIPES, pH 6.0
Ion exchange buffer B	20 mM PIPES, 1 M NaCl, pH 6.0
SEC buffer	20 mM PIPES, 150 mM NaCl, 0.1 mM EDTA, pH 6.0
NMR buffer	20 mM PIPES, 150 mM NaCl, 0.1 mM EDTA, 2% (v/v) glycerol-D_8, pH 6.0

Table 6.6.: Biochemical buffers and staining solutions.

Coomassie-blue staining solution	25% (v/v) isopropanol, 10% (v/v) acetic acid, 0.5 g/l Coomassie Brilliant Blue R250
Laemmli buffer (4 x)	200 mM Tris-HCl, 40% (v/v) glycerol, 8% (w/v) SDS, 8% (v/v) 2-mercaptoethanol, 0.05% (w/v) bromophenol blue
Phosphate-buffered saline (PBS, 10 x)	80 g/l Nacl, 2 g/l KCl, 2.4 g/l KH_2PO_4, 18.05 g/l Na_2HPO_4 x 2 H_2O
Tris-buffered saline (TBS, 10 x)	80 g/l NaCl, 2 g/l KCl, 30 g/l Tris-HCl, adjusted to pH 9.0 or 8.0 at RT
SDS running buffer	50 mM Tris-HCl, 385 mM glycine, 0.1% SDS (w/v), pH 8.3
TAE buffer	40 mM Tris, 20 mM acetic acid, 1 mM EDTA

Table 6.7.: Growth media and additives.

Ampicillin (1000 x)	100 mg/ml ampicillin sodium salt in 20 mM Na_2PO_4, pH 8.0
Chloramphenicol (1000 x)	34 mg/ml Chloramphenicol in ethanol (100%)
LB	10 g/l Tryptone, 5 g/l yeast extract, 5 g/l NaCl
LB agar plates	LB supplemented with 0.02 g/l Agar
LB + Mg	10 g/l Tryptone, 5 g/l yeast extract, 5 g/l NaCl, 2 mM $MgSO_4$
SOB	20 g/l Tryptone, 5 g/l yeast extract, 0.58 g/l NaCl, 0.19 g/l KCl
SOC	962 ml/l SOB, 10 ml/l 1 M $MgCl_2$, 10 ml/l 1 M $MgSO_4$, 10 ml/l 20% Glucose
M9 salts (5 x)	21.5 g/l Na_2HPO_4 x 2 H_2O, 15 g/l KH_2PO_4, 2.5 g/l NaCl
Trace element solution (TS)	100 mg/l $ZnSO_4$ x $7H_2O$, 30 mg/l $MnCl_2$ x $4H_2O$, 300 mg/l H_3BO_3, 200 mg/l $CoCl_2$ x $6H_2O$, 20 mg/l $NiCl_2$ x $6H_2O$, 10 mg/l $CuCl_2$ x $2H_2O$, 900 mg/l Na_2MoO_4 x $2H_2O$, 20 mg/l Na_2SeO_3
Vitamin solution (1000 x)	1 mg/ml D-biotin, 1 mg/ml choline chloride, 1 mg/ml folic acid, 1 mg/ml nicotinamide, 1 mg/ml Na-D-pantothenate, 1 mg/ml pyridoxine hydrochloride, 0.1 mg/ml riboflavin
M9 minimal medium	1 x M9 salts, 1 x TS solution, 1 x vitamin solution, 0.5 g/l NH_4Cl, 2 g/l ^{13}C- or 4 g/l ^{12}C-glucose, 10 μM $FeCl_3$ x 6 H_2O, 5 mg/ml thiamine hydrochloride

Table 6.8.: Bacterial strains for gene cloning and protein expression.

Name (Supplier / Reference)	Genotype
OmniMax T1 (Invitrogen, Carlsbad, USA)	F'{proAB$^+$ lacI^q lacZΔM15 Tn10(Tet^R)} mcrA Δ(mrr-hsdRMS-mcrBC) Φ80(lacZ)ΔM15 Δ(lacZYA-argF) U169 endA1 supE44 thi-1 gyrA96 relA1 deoR tonA panD
Mach T1 (Invitrogen, Carlsbad, USA)	F$^-$ ϕ80(lacZ) ΔM1 ΔlacX74 hsdR(rK$^-$ mK$^+$) ΔrecA1398, endA1, tonA
Rosetta 2(DE3) (Millipore, Schwalbach, Germany)	F$^-$ ompT hsdSB(rB$^-$ mB$^-$) gal dcm(DE3) pRARE2 (Cam^R)

6.1.7. Bacterial Strains

In this work, *Escherichia coli* (*E. coli*) cells were used for DNA multiplication and cloning experiments (OmniMax T1, Mach1), as well as heterologous protein expression (Rosetta2 (DE3)).

6.1.8. Primer Pairs & Expression Vectors

DNA oligomers used as PCR primers were ordered HPLC-purified at BioTez (Berlin, Germany), dissolved in sterile H_2O, and stored at -20 °C. The vector pGEX-4T-2 (GE Healthcare, Freiburg, Germany) served as the expression vector for proteins. Resulting proteins contained a carboxy-terminal glutathione-S-transerfase domain that is linked to the expressed protein by a thrombin recognition sequence. Additionally, pGEX-4T-2 transfected bacteria are ampicillin-resistant due to a beta-lactamase gene.

6.1.9. Hardware & Consumables

Reusable equipment and laboratory hardware are summarised in Table 6.10, and consumable goods in Table 6.11. Unattributed hardware was of standard laboratory quality.

Table 6.9.: Primer sequences for DNA sequencing (T7, pGEX), site-directed mutagenesis (LC3C(147)), and LC3C$_{\Delta 2-9}$ deletion mutant.

Notation	5' – 3'
T7 forward primer (promotor)	TAA TAC GAC TCA CTA TAG GG
T7 reverse primer (terminator)	GCT AGT TAT TGC TCA GCG G
pGEX forward primer	GGG CTG GCA AGC CAC GTT TGG TG
pGEX reverse primer	CCG GGA GCT GCA TGT GTC AGA GG
LC3C(147) primer 'sense'	GCG AGC CAG GAA ACC TTT GGC TAG TAA GAG AGC GCT GCA
LC3C(147) primer 'anti-sense'	TGC AGC GCT CTC TTA CTA GCC AAA GGT TTC CTG GCT CGC
LC3C$_{\Delta 2-9}$ 'sense'	TTT GGA TCC ATG CGT CCG TTT AAA CAG
LC3C$_{\Delta 2-9}$ 'anti-sense'	AA GCG GCC GCT TAC TAG CCA AAG

6.2. Molecular Biology Methods

In this work, the enteric bacteria *Escherichia coli* (*E. coli*) was used for molecular biology experiments. Competent *E. coli* cells were created as described in Section 6.2.1. DNA transformation, cloning and DNA preparation experiments are depicted in Sections 6.2.2 to 6.2.6. Typically, *E. coli* cells for purification of plasmid DNA (see Section 6.2.7) were freshly transformed, while protein expression cultures were cultivated from frozen glycerol stock cultures (as depicted in Section 6.2.9).

6.2.1. Competent Cells

Competent *E. coli* cells were created by the $CaCl_2$ method (Cohen et al., 1972). To this end, 5 ml overnight culture was prepared from a glycerol stock culture and on the following day used to inoculate 100 ml of LB growth medium to a UV / Vis absorption at 600 nm (OD_{600}) of 0.1 units. This culture was grown at 37 °C and 160 rpm until its OD_{600}) reached 0.5 units and centrifuged at 4 °C and 7000 x *g* for 10 min. The bacterial pellet was resuspended in 10 ml of an ice-cooled 50 mM $CaCl_2$ solution, and centrifuged at 7000 x *g* for 10 min. Cell pellet was again resuspended in an ice-

Table 6.10.: Reusable equipment and laboratory hardware.

ÄKTApurifier	GE Healthcare, Freiburg, Germany
Äkta Superloop 50 ml	GE Healthcare, Freiburg, Germany
Amicon stirred cell (10 ml, 150 ml)	Millipore, Schwalbach, Germany
Cell disruptor, TS series	Constant Systems, Daventry, United Kingdom
Centrifuge Avanti J-20 XP	Beckman Coulter, Krefeld, Germany
Centrifuge Eppendorf 5415 R	Eppendorf, Hamburg, Germany
Centrifuge Eppendorf 5804 R	Eppendorf, Hamburg, Germany
DynaPro DLS	Wyatt Technology, Santa Barbara, USA
Freedom EVO pipetting robot	Tecan, Männedorf, Switzerland
GelDoc 2000, ChemiDoc MP	BioRad, München, Germany
Hoefer SE260	Hoefer, Holliston, USA
Incubator shaker Multitron Pro / InforsHT	Infors, Einsbach, Germany
Lambda 25 UV / Vis spectrophotometer	Perkin Elmer, Waltham, USA
Lyophiliser Alpha 1-4 Loc-1m	Christ GmbH, Osterode, Germany
Milli-Q-Biocell pure water system	Millipore, Schwalbach, Germany
Nalgene filter devices	Thermo Scientific, Schwerte, Germany
Nanophotometer P300	Implen, München, Deutschland
PCR iCycler	BioRad, München, Germany
pH-meter F20	Mettler-Toledo, Gießen, Germany
Pharmacia FPLC	Pharmacia Biotech, Uppsala, Sweden
Pipettes 'Research plus'	Eppendorf, Hamburg, Germany
Resource-S, 1 ml	GE Healthcare, Freiburg, Germany
Superdex 75 16/60 and 26/60	GE Healthcare, Freiburg, Germany
Thermomixer, Thermomixer compact	Eppendorf, Hamburg, Germany

Table 6.11.: Consumable goods.

Crystallisation plates CrystalQuick	Greiner BioOne, Frickenhausen, Germany
Dialysis membrane Spectra Por (1000 Da MWCO)	Spectrumlabs, Frankfurt a.M., Germany
Filter membrane (cellulose acetate, 0.2 µ)	Sartorius, Göttingen, Germany
Spin Column Amicon Ultra (0.5 ml, 3000 Da NMWL)	Millipore, Schwalbach, Germany
Syringe filter (PVDF, sterile)	Sartorius, Göttingen, Germany
Ultrafiltration membrane for Amicon stirred cell (1000 Da, and 3000 Da NMWL)	Millipore, Schwalbach, Germany

cooled $CaCl_2$ solution (20 ml, 50 mM $CaCl_2$), incubated on ice for 30 min, and then centrifuged at 7000 x *g* for 10 min. The cell pellet was resuspended in 5 ml ice-cooled $CaCl_2$ solution (50 mM) and incubated for 15 min on ice. 2.5 ml of this cold cell suspension was gently mixed with 469 µl of a pre-chilled 80% glycerol solution on ice. Finally, bacterial cells were aliquoted (200 µl) in pre-chilled 1.5 ml reaction tubes, flash-frozen in liquid nitrogen, and stored at -80 °C.

6.2.2. Transformation of *E. coli*

Frozen stock cultures of competent cells were thawed on ice for 20 min before transformation experiments. Then ~100 ng DNA in a volume of less than 1.0 µl was added to competent cells, the suspension gently mixed, and incubated on ice for 20 min. Transformation of competent cells was conducted by heat-shock at 42 °C for 45 s, immediately followed by addition of 500 µl SOB medium (Table 6.7), and 2 min incubation on ice. Bacterial cells were then cultivated at 37 °C and 800 rpm for 60 min in a benchtop incubator (Thermomixer, Eppendorf, Hamburg, Germany). Subsequently, 100 µl of this cell suspension was used to inoculate a selective LB agar plate while the remainder was centrifuged at RT, and 4000 x *g* for 5 min. The supernatant was removed for the most part and the cell pellet resuspended in the remaining volume. This concentrated cell suspension was used to inoculate another selective LB agar

plate, and both selective LB agar plates were incubated overnight at 37 °C.

6.2.3. Cloning of LC3C

In this work, an *E. coli* codon optimised, full-length human MAP1LC3C (microtubule-associated protein light chain 3C) coding sequence of 147 amino acids (LC3C(147)) according to Uniprot accession number Q9BXW4 (http://www.uniprot.org/uniprot/) was ordered from GeneArt (Regensburg, Germany; now Thermo Scientific). The synthesised gene contained restriction sites for *Kpn*I and *Bam*HI restriction enzymes at the 5' end, as well as, *Not*I and *Xho*I restriction sites at the 3' end of the LC3C(147) gene. Subsequent cloning experiments made use of only *Bam*HI and *Not*I restriction sites. The synthesised LC3C(147) gene was provided as an insert cloned into the GeneArt's pMKT-2 vector (pMKT-2-LC3C(147)). For all cloning experiments, *E. coli* OmniMax T1 cells were used.

Initially, 10 µg of pMKT-2-LC3C(147), and 10 µg of pGEX-4T-2 expression vector were individually incubated for 3 h at 37 °C in *Bam*HI-buffer and 10 U *Bam*HI (Fermentas, St. Leon-Rot, Germany). Subsequently, this reaction was incubated with 10 U *Not*I (Fermentas, St. Leon-Rot, Germany) for 3 h at 37 °C. Next, target vector pGEX-4T-2 was dephosphorylated by shrimp alkaline phosphatase (SAP) or fast thermosensitive alkaline phosphatase (FastAP) for 1.5 h at 37 °C to prevent recircularisation. Afterwards, solutions were incubated for 20 min at 80 °C to deactivate enzymes, and linearised vector DNA was purified by agarose gel electrophoresis (see Section 6.4.3).

Vector and LC3C(147) insert-DNA was mixed in molar ratios from 1:5 to 1:15 in T4 DNA ligase buffer (Fermentas, St. Leon-Rot, Germany) and ligated by addition of 2 µl T4 DNA ligase. The manufacturer's reaction buffer was supplemented with a high molecular weight PEG (5% (w/v) PEG 4000) to increase ligation efficiency and the ligation reaction was incubated overnight at 16 °C.

E. coli cells were transformed with the ligation product (see Section 6.2.2 for the transformation procedure), cultivated on LB-agar plates containing 100 µg/ml ampicillin overnight, and colonies were tested by colony PCR (see also Section 6.2.6). In a final step, *E. coli* with an insert of the expected molecular weight were cultivated in 10 ml LB-Amp medium containing 100 µg/ml ampicillin overnight, and plasmid DNA was extracted, and sequenced, as described in Section 6.4.1.

6.2.4. Site-Directed Mutagenesis

Table 6.12.: QuikChange site-directed mutagenesis reaction.

Volume	Component
5.0 µl	Reaction buffer*
0.6 µl (50 ng)	pGEX-4T-2-LC3C(147)
2.1 µl (1.25 µg)	Primer 'sense'
2.1 µl (1.25 µg)	Primer 'anti-sense'
1.0 µl	dNTP mix*
3.0 µl	Quik solution*
36.2 µl	H_2O
1.0 µl	PfuTurbo polymerase*

* Provided by QuikChange kit.

Site-directed mutagensis of gene sequences was accomplished using the QuikChange XL II kit (see Table 6.3), which is based on the method of Kunkel (1985). Primer sequences (LC3C(147), see Table 6.9), and reaction conditions were adjusted according to information provided by Stratagene's webservice (http://www.stratagene.com/qcprimerdesign, now: www.agilent.com/genomics/qcpd), and are listed in Tables 6.12 and 6.13.

Here, the expression vector pGEX-4T-2 containing a full-length human LC3C gene of 147 amino acids (pGEX-4T-2-LC3C(147)), circa 5,400 base pairs) was used as the template. The elongation time step in a PCR cycle (see Table 6.13) was adjusted under the assumption that the kit's PfuTurbo polymerase is able to extend DNA templates at a rate of ~500 base pairs per minute. In the final step of the QuikChange reaction, parental and therefore methylated DNA was hydrolysed by addition of *Dpn*I.

Two stop codons were introduced in the full-length LC3C gene sequence to create a gene coding for cytosolic, mature LC3C of 126 amino acids (pGEX-4T-2-LC3C). The QuikChange reaction product (pGEX-4T-2-LC3C) was purified via agarose gel electrophoresis (see Section 6.4.3) and sequenced (see also Section 6.4.1).

Table 6.13.: QuikChange site-directed mutagenesis PCR cycling.

Step	Cycles	Temperature	Time
1	1	95 °C	0.5 min
2	18	95 °C	0.5 min
		55 °C	1 min
		68 °C	10 min*
3	∞	4 °C	

* Elongation step.

6.2.5. PCR Mutagenesis

PCR mutagenesis was used to create a deletion mutant of mature, cytosolic LC3C (LC3C$_{\Delta 2-9}$), where amino acids 2 to 9 are removed from the protein sequence. PCR conditions and cycling are summarised in Tables 6.14 and 6.15, respectively. Primer pairs (LC3C$_{\Delta 2-9}$, listed in Table 6.9) containing 5' and 3' recognition sites for *Bam*HI and *Not*I restriction enzymes, respectively, were designed to match respective annealing temperatures, and overhangs necessary for optimal restriction enzyme efficency. Generally, *Bam*HI shows optimal activity with three or more additional (overhanging) nucleotides neighbouring the recognition sequence, whereas *Not*I shows optimal activity with one or more overhanging nucleotide (NEB guidelines).

PCR reaction products were purified via agarose gel electrophoresis (see also Sec-

Table 6.14.: PCR reaction buffer for deletion mutant LC3C$_{\Delta 2-9}$.

Volume	Component
5.0 µl	AccuPrime-Mix*
0.14 µl (100 ng)	pGEX-4T-2-LC3C
0.5 µl (50 µM)	Primer LC3C$_{\Delta 2-9}$ 'sense'
0.5 µl (50 µM)	Primer LC3C$_{\Delta 2-9}$ 'anti-sense'
42.86 µl	H_2O
1.0 µl	AccuPrime Pfx polymerase*

* Provided by AccuPrime manufacturer.

Table 6.15.: PCR cycling to create deletion mutant LC3C$_{\Delta 2-9}$.

Step	Cycles	Temperature	Time
1	1	95 °C	0.5 min
2	35	95 °C	0.5 min
		56 °C	1 min
		68 °C	1 min*
3	∞	4 °C	

* Elongation step.

tion 6.4.3) and ligated into expression vector pGEX-4T-2 according to the description in Section 6.2.3. Transformants were tested via colony PCR and sequenced, as described in Section 6.2.6 and Section 6.4.1, respectively.

6.2.6. Colony PCR

Colony PCR is a valuable high-throughput method to simultaneously screen multiple bacterial colonies for a DNA insert. For this, bacterial cells of selected colonies are lysed by a combination of SDS and a prolonged heating step in the first cycle of an otherwise regular PCR reaction.

To conduct a colony PCR experiment, a bacterial colony on an LB agar plate was touched by a sterile, disposable pipette tip. The tip was then rubbed against the inside of a thin-walled PCR test tube and subsequently streaked across a marked Section of a new selective LB agar plate. Then, the thin-walled test tubes were pre-chilled on ice, and 0.2 µl Taq polymerase and 50 µl colony PCR reaction buffer (see Table 6.16) added. Negative control reactions contained neither bacterial cells nor DNA. Positive control reactions contained the pGEX-4T-2 vector without an insert, and the pGEX-4T-2 vector with a confirmed and sequenced insert. The colony PCR cycle is summarised in Table 6.17.

Colony PCR experiments were analysed by separating PCR reaction products by agarose gel electrophoresis (Section 6.4.3). If an amplified DNA fragment could be attributed by its apparent size to to the expected insert size, the PCR reaction was

traced back to the originating bacterial colony and its plasmid DNA amplified and isolated (see also Section 6.2.7). Subsequently, DNA was sequenced as described in Section 6.4.1.

Table 6.16.: Colony PCR reaction buffer.

Volume	Component
5.0 µl	ThermoPol buffer*
3.0 µl	25 mM $MgCl_2$
0.5 µl	Forward primer
0.5 µl	Reverse primer
1.0 µl	dNTP mix*
0.2 µl	Taq polymerase*
39.8 µl	H_2O

* Provided by NEB.

Table 6.17.: Colony PCR cycling.

Step	Cycles	Temp.	Time
1	1	95 °C	5 min
2	30	95 °C	1 min
		60 °C	1 min
		68 °C	1 min*
3	∞	4 °C	

* Elongation step.

6.2.7. Purification of Plasmid DNA

Plasmid-DNA was extracted from *E. coli* cells with commercially available DNA-extraction and -purification kits (Table 6.3) in accordance with manufacturer's guidelines. Generally, plasmid-DNA was dried by a gaseous nitrogen stream after elution, dissolved in sterile H_2O, and stored at -20 °C.

6.2.8. DNA Library

Entries for pGEX-4T-2-LC3C$_{1-147}$, pGEX-4T-2-LC3C, pGEX-4T-2-GABARAP$_{1-117}$, pGEX-4T-2-GABARAP$_{1-116}$, pET-22b-LC3C, and pGEX-4T-2-LC3C$_{\Delta 2-9}$ have been placed in the institute's DNA library.

6.2.9. Stock Cultures

A convenient method to consistently grow bacterial cell cultures for protein expression is the use of a frozen bacterial glycerol stock-culture. The glycerol stock-culture was

generated from a single, uniform colony of a fresh *E. coli* tranformation experiment. This colony was used to inoculate 50 ml of selective LB medium to grow an overnight culture. On the next day, 10 ml fresh selective LB-medium was inoculated with the overnight culture to an OD_{600} of 0.1 units and grown to OD_{600} 0.5 units at 37 °C and 160 rpm. This bacterial culture was then cooled on ice for 15 min, 875 µl collected and slowly mixed with 100 µl ice-cooled 80% (v/v) glycerol and 25 µl of a sterile, 20% (w/v) glucose solution. Finally, the bacterial culture was aliquoted (250 µl), shock frozen in liquid nitrogen, and stored at -80 °C.

Typically, overnight starter cultures for expression cultures were inoculated by scraping a sterile pipette tip across the frozen surface of a glycerol stock-culture. The tip was then transferred into fresh selective LB medium for overnight incubation at 30 °C and 160 to 200 rpm.

6.3. Preparative Methods

The following Sections describe in detail the laboratory scale preparative methods used for protein expression (see Section 6.3.1, and protein purification (described in Sections 6.3.2 and 6.3.3). Additionally, Sections 6.3.4, and 6.3.5 portray the procedure applied to concentrate and lyophilise protein samples, respectively.

6.3.1. Heterologous Expression of LC3C

Human LC3C was heterologously expressed in *E. coli* Rosetta (DE3) and Rosetta 2 (DE3) cells by a pGEX-4T-2 vector construct (pGEX-4T-2-LC3C) requiring ampicillin and chloramphenicol selection markers. This construct lead to an amino-terminal glutathione S-transferase-LC3C (GST-LC3C) fusion protein. The protein linker sequence between GST and LC3C domain contains a recognition sequence for the serine protease thrombin. After proteolysis, two amino acid residues (glycine and serine) of the thrombin recognition sequence remained with the primary sequence of cleaved LC3C.

To express the fusion protein, an overnight culture was induced by inoculating 100 ml LB medium containing 100 μg/ml ampicillin, 34 μg/ml chloramphenicol, and 2 mM $MgSO_4$ (LB-Amp-Cam-Mg, composition see Table 6.7) with a glycerol stock culture (see also Section 6.2.9). Additionally, one drop of Antifoam A (Sigma-Aldrich, Taufkirchen, Germany) from a 50 μl sterile pipette tip was added to the medium and the culture was incubated overnight at 30 °C and 160 rpm. The overnight culture was then centrifuged for 20 min at 4000 x *g* and the supernatant discarded. The bacterial cell pellet was resuspended in LB-Amp-Cam-Mg medium and added to fresh 1 l LB-Amp-Cam-Mg medium in a 2 l, indented flask until the medium's OD_{600} reached 0.1 units. Again, a drop of Antifoam A was added, and the expression culture was cultivated at 37 °C and 200 rpm until its OD_{600} reached 0.6 units.

If isotopically unlabelled LC3C was to be expressed the temperature was reduced to 25 °C, and the culture incubated for 30 min while continuously shaken as before. Protein expression was induced by adding IPTG (isopropyl β-D-1-thiogalactopyranoside) to a final concentration of 200 μM and expressed for 4 h at 200 rpm and 25 °C.

To express [U-^{15}N]-, or [U-^{15}N, ^{13}C]-labelled LC3C protein, an expression culture in LB-Amp-Cam medium was centrifuged upon reaching OD_{600} 0.6. The bacterial

cell pellet was resuspended in labelled M9 minimal medium containing 100 μg/ml ampicillin (M9-Amp) and incubated at 37 °C and 200 rpm in indented 2 l flasks until OD_{600} of 1.0 units was reached. Then, the incubator shaker temperature was reduced to 25 °C, the expression culture shaken for 30 min, and, finally, protein expression induced by adding IPTG to a final concentration of 1 mM. The protein expression was continued for 5 to 6 h at 25 °C and 200 rpm.

Finally, the expression culture was centrifuged for 30 min at 8 °C and 4000 x *g* in an Avanti J-20 XP centrifuge (Beckman Coulter, Krefeld, Germany). The cell pellet resuspended in 10 ml of cold PBS buffer and transferred to a 50 ml sterile polypropylene tube. Resuspended bacteria were then centrifuged for 20 min at 6 °C and 4000 x *g*, the supernatant discarded, and the bacterial pellet was stored at -20 °C.

6.3.2. Purification of LC3C by Affinity Chromatography

Affinity chromatography commonly exploits a carboxy- or amino-terminally inserted protein domain into the protein of interest's primary sequence and a solid-phase material with a high affinity towards the inserted protein domain. Thereby, the protein of interest can be enriched relatively easy in a crude cell lysate. In this work, the first chromatographic step in the purification protocol took advantage of the affinity of GST-LC3C fusion protein towards glutathione (GSH). Glutathione is covalently attached to the solid-phase column material sepharose (GSH-sepharose). After washing steps, the peptide bond between GSH-bound GST and LC3C was enzymatically hydrolysed by thrombin. While the GST-domain remains attached to the solid phase material, LC3C is released into the surrounding aqueous buffer and further purified by additional chromatographic steps.

Commonly, a frozen bacterial pellet of an expression culture was thawed and resuspended in 5 ml cold lysis buffer per gram of the wet cell pellet (buffer composition summarised in Table 6.5). The cell suspension was homogenised in a Dounce homogeniser by a glass pestle. Cells were then disrupted twice in a TS cell disruptor (Constant Systems, Daventry, United Kingdom) at 1.7 kBar and 10 °C. Resulting bacterial lysate was centrifuged for 45 min at 50000 x *g* and 12 °C to remove insoluble impurities. Next, the cleared lysate was filtered by a syringe filter (0.45 μm, PVDF) and incubated with 5 ml GSH-sepharose, which had been washed and equilibrated with five column volumes (CV) of washing buffer (buffer composition listed in Table

6.5). The cell lysate / GSH-suspension was then incubated overnight in a cold room while being gently agitated on a roller shaker at 6 °C.

In the next step, a GSH-sepharose suspension was filled in a glass chromatography column and the buffer eluted by gravity flow. GSH-sepharose was washed with 10 CV washing buffer and consecutively 5 CV thrombin buffer (buffer composition see Table 6.5). The column was again drained by gravity flow. Afterwards, one column volume of thrombin buffer was added, containing 100 µl of a 2 mg/ml bovine thrombin stock solution, and the suspension gently homogenised. Beforehand, a thrombin stock solution was created by purifying the manufacturer's lyophilised bovine thrombin (Merck KGaA, Darmstadt, Germany). For this purpose, thrombin was dissolved in PBS and purified by size exclusion chromatography (Superdex 75, 26/60), equilibrated in PBS and using PBS as the mobile phase at 6 °C.

After circa 1 h, thrombin buffer was eluted and GSH-sepharose was washed three times with 1 CV thrombin buffer. To remove thrombin in the eluted fractions and reduce the probability of an unspecific interaction of thrombin with the protein of interest, 1 ml benzamidine sepharose (equilibrated with 5 CV thrombin buffer) was added to the eluted fractions. This suspension was incubated for 2 h on a roller shaker at 6 °C, then pipetted into a new glass chromatography column and the crude LC3C solution eluted by gravity flow. Afterwards, benzamidine sepharose was washed with 5 CV thrombin buffer and eluates were combined with the crude LC3C solution.

In a final step, the crude LC3C solution was transferred into a dialysis tube (Spectra Por, 1000 Da, Spectrumlabs, Frankfurt, Germany) and dialysed in 5 l pre-chilled dialysis buffer (see also Table 6.5) for 3 h at 6 °C. Then, the dialysis buffer was exchanged for fresh, pre-chilled dialysis buffer and dialysis completed overnight at 6 °C. The resulting dialysed, crude LC3C solution was syringe filtered (45 mm, 0.2 µm, PVDF) and loaded into a 50 ml Äkta superloop (GE Healthcare, Freiburg, Germany) to continue the purification scheme by ion exchange chromatography.

6.3.3. Purification of LC3C by Ion Exchange and Size Exclusion Chromatography

Ion exchange and size exclusion chromatography steps were executed using an ÄKTApurifier system (GE Healthcare, Freiburg, Germany) controlled by Unicorn 5.0 soft-

ware. UV absorption of the mobile phase was recorded at 280 and 320 nm to observe protein absorption and possible coagulation of protein molecules, respectively. Additionally, the conductance of the eluted mobile phase was recorded. Chromatographic gradients are noted below (composition of buffer B see Table 6.5).

The ion exchange chromatography step was accomplished using a Resource-S 1 ml cation exchange column (GE Healthcare, Freiburg, Germany) at a flow rate of 2 ml/min at RT. The Resource-S column was equilibrated with 5 CV 5% buffer B. The crude LC3C solution was loaded onto the column via an ÄKTA superloop at a flow-rate of 1.5 ml/min. After loading, the Resource-S column was washed with at least 5 CV 5% buffer B until the UV absorption and system pressure settled to constant values. Then, an ion exchange program (as specified below) was started and 500 µl fractions collected. Fractions indicating a homogeneous protein composition by UV absorption and peak shape symmetry were combined and the serine protease inhibitor phenylmethanesulfonyl fluoride (PMSF) added to a final concentration of 0.2 µM. PMSF was added from a concentrated, 100% ethanolic stock solution (1000 x) and therefore prediluted with eluted buffer from a neighbouring fraction containing no protein to avoid protein precipitation. Fractions from separate ion exchange chromatography runs were combined and concentrated (V < 3.5 ml) in an Amicon stirred-cell before size exclusion purification steps.

Final purification of LC3C was performed via size exclusion chromatography (SEC) with Superdex 75 16/60 or 26/60 columns (GE Healthcare, Freiburg, Germany) at a flow rate of 1.5 ml/min and at 8 °C. Superdex columns were equilibrated with 1.5 CV SEC buffer (buffer composition see Table 6.5). Fractions containing purified LC3C were pooled and stored at 6 °C.

- **Gradient 1**: Ion exchange chromatography of crude LC3C
  Buffer A: 20 mM PIPES, pH 6.0
  Buffer B: 20 mM PIPES, 1 M NaCl, pH 6.0
  Linear gradients: 0 – 1 min 5% B; 1 – 2 min 10% B; 2 – 7 min 10% B; 7 – 27 min 25% B; 27 – 29 min 25% B, 29 – 30 min 50% B, 30 – 31 min 50% B, 31 – 32 min 100% B; 32 – 34 min 100% B; 34 – 35 min 5% B, 35 –40 min 5% B

- **Gradient 2**: Ion exchange chromatography of GST / LC3C mixture
  Buffer A: 20 mM PIPES, pH 6.0
  Buffer B: 20 mM PIPES, 1 M NaCl, pH 6.0

Linear gradients: 0 – 1 min 5% B; 1 – 2 min 10% B; 2 – 7 min 10% B; 7 – 27 min 25% B; 27 – 29 min 25% B, 29 – 30 min 50% B, 30 – 31 min 50% B, 31 – 32 min 100% B; 32 – 34 min 100% B; 34 – 35 min 5% B, 35 –40 min 5% B

- **Isocratic**: Size exclusion chromatography of LC3C
  Buffer: SEC buffer
  Flow-rate: 1.5 ml/min

6.3.4. Concentrating Protein Samples

Protein solutions purified by SEC were concentrated in a two step procedure. First, by ultra filtration in a stirred Amicon cell (Millipore, Schwalbach, Germany), and secondly, by spin-columns in a refrigerated, bench-top centrifuge. Through stirred Amicon cells, high protein concentration gradients at the boundary layer of the ultrafiltration membrane are avoided. In addition, a concentration progress can be easily observed and controlled for larger volumes, while spin spin-columns are ideal for smaller volumes ($\leq$ 3 ml).

To concentrate a protein solution by ultra-filtration membranes (1,000 Da nominal molecular weight limit (NMWL), regenerated cellulose membrane, Millipore, Schwalbach, Germany), a stirred 10 ml Amicon cell, pressurised by gaseous nitrogen, was used in a cold room at 6 °C. The concentration process was interrupted, when the volume dropped below ~3 ml and the concentration progress was continued using spin-columns. In addition, a UV-Vis spectrum of the protein solution was recorded to determine the concentration of the protein solution as well as possible protein aggregation. Aggregation would be recognised by an increased base line absorption around 300 to 320 nm in a UV-Vis spectrum as a result of light-scattering effects of higher molecular-weight aggregates (Serdyuk et al., 2007).

Further concentration of the protein sample was achieved by using 500 µl spin-columns (Amicon Ultra, 3000 Da NMWL, Millipore, Schwalbach, Germany) in a pre-cooled, refrigerated bench-top centrifuge at 10 °C and 8000 x *g*. In 10 min intervals, a protein solution was carefully homogenised. The final concentration of a protein sample was determined by UV-Vis spectroscopy.

6.3.5. Lyophilisation of LC3C

A refrigerated, concentrated LC3C protein solution was supplemented by naturally abundant or uniformly ^{2}H-labelled 2% glycerol (v/v) in a 2 ml test-tube. The solution was carefully homogenised and subsequently flash-frozen in liquid nitrogen. Thereafter, the test tube's lid was exchanged for a manually perforated substitute and the sample placed in an Alpha1-lyophiliser overnight (Alpha1-4 Loc-1m, Martin Christ, Osterode am Harz, Germany).

6.4. Analytical Methods

All routinely utilised analytical methods are described in detail below. Sections 6.4.1 and 6.4.2 describe methods used to determine DNA sequences and concentrations, and the Section 6.4.3 specifies electrophoretic separation procedures for protein and DNA samples. The operation of UV / vis spectrophotometer with protein and DNA samples is depicted in Section 6.4.4.

6.4.1. DNA Sequencing

All DNA sequencing experiments were performed at Seqlab (Göttingen, Germany). Typically, 700 ng plasmid DNA was supplemented with 20 pmol forward and reverse primer DNA (summarised in Table 6.9), and the resulting volume was adjusted with H_2O to 7 µl. Sequencing chromatograms were analysed with Chromas 2.33 (Technelysium Pty Ltd., Australia), while Clustal (http://www.ebi.ac.uk/Tools/msa/clustalo/) was used for sequence alignments.

6.4.2. DNA Concentration

Absorption of DNA solutions were measured in a UV-Vis Nanophotometer P300 (Implen, München, Germany). A concentration was calculated based on the assumption that 50 µg double-stranded DNA leads to an absorption value of 1.0 at a 1 cm pathlength and wavelength of 260 nm. The ratio of UV absorption at 260 nm and 280 nm was also calculated to aid evaluation of the purity of DNA preparations. A ratio of ~1.8 is considered optimal for high quality DNA preparations. Ratios smaller than 1.6 are indicative of protein contaminations, while values larger than 1.8 may indicate a contamination with RNA molecules. Differing absorption ratios are a result of differences in absorption maxima between the constituting aromatic moieties of DNA, RNA, and amino acids.

6.4.3. Gel Electrophoresis

All gel electrophoretic methods use crosslinked polymers to separate macromolecules based on their hydrodynamic radii and charges, while macromolecules migrate along

an electric field. DNA can be easily separated based on its poly-anionic phosphate backbone and constant charge per monomer ratio. Here, a DNA molecule's charge is directly proportional to the number of DNA bases in a given DNA strand. In native proteins, the net-surface-charge depends on amino acid composition and pH of the surrounding solution, thus the net-charge of a protein is not coercively proportional to a protein's molecular size or number of residues. Therefore, electrophoretic separations commonly use amphiphilic sodium dodecyl sulphate (SDS), which denatures proteins and creates an overall negative net-charge as SDS binds proteins in a near constant binding ratio of circa 1.4 mg SDS per 1 mg protein (Pitt-Rivers and Impiombato, 1968). Subsequently, proteins will be separated by the number of residues and a mechanism dominated by mechanical resistance of the (crosslinked) polymer.

Agarose gel electrophoresis

Agarose gel electrophoresis was used to separate and analyse DNA molecules. For this purpose, 0.8 to 1.5% (w/v) agarose was added to 50 ml TAE buffer (buffer composition see Table 6.6) and dissolved by heating the solution to the boil. A higher agarose percentage was used if small DNA-fragments (< 1000 base pairs) were investigated. The agarose solution was allowed to cool to circa 50 °C, then supplemented with 1 μg/ml ethidium bromide, and poured into a casting chamber. After polymerisation was completed, DNA samples were mixed with 6 x loading dye (Fermentas, St. Leon-Rot, Germany) and loaded into the casted gel lanes. Typically, electrophoretic separation was conducted in 30 min at 80 V and 300 mA. Migrated DNA was visualised by irradiation with UV light using a GelDoc 2000 system (BioRad, München, Germany). Gel extraction of DNA fragments was accomplished by NucleoSpin Gel and / or PCR Clean-up kit (Macherey-Nagel, Düren, Germany). Purified DNA was eluted with H_2O and stored at -80 °C.

Sodium dodecyl sulphate polyacrylamide gel electrophoresis (SDS-PAGE)

Protein solutions were qualitatively analysed by denaturing electrophoresis according to Laemmli (1970). A non-continuous gel, consisting of an upper low pH, low crosslinked stacking gel, and an high pH, high crosslinked running gel below, act jointly with a glycine containing running buffer. Disparity of pH values in stacking and

Table 6.18.: Stacking gel (5%).

4.85% acrylamide (w/v)
0.15% bis-acrylamide (w/v)
125 mM Tris-HCl, pH 6.8
0.1% SDS (w/v)
0.1% APS (w/v)
0.1% TEMED (v/v)

Table 6.19.: Running gel (15%).

14.55% acrylamide (w/v)
0.45% bisacrylamide (w/v)
375 mM Tris-HCl, pH 8.8
0.1% SDS (w/v)
0.1% APS (w/v)
0.1% TEMED (v/v)

running gel make use of glycine's zwitterionic nature. While glycine is protonated in the stacking gel (composition see Table 6.18), it is uncharged in the running gel (composition see Table 6.19). The change in glycine's charge ultimately leads to a narrow, concentrated running front of analytes in a protein sample, and an increase in resolution.

All protein samples analysed by this method were heated to 95 °C for 5 min prior electrophoresis and 4 x Laemmli buffer added (composition see Table 6.6). Apparent molecular weights were estimated based on migration distance and compared to 'Pierce Unstained Protein Molecular Weight Marker' (26610, Thermo Scientific, Schwerte, Germany) for qualitative and semi-quantitative analyses (see also figure 6.1).

SDS-PAGE gel slabs were mounted in a vertical electrophoresis unit (Hoefer SE260, Hoefer Scientific Instruments, Holliston, USA), and submerged in SDS running buffer (buffer composition see Table 6.6). The design of electrophoresis units often lead to formation of foam inside a unit's lid, thereby possibly influencing electric flow by short circuiting electrodes. Hence, a triple folded, dry cellulose sheet was placed under the lid, in between electrodes to prevent an otherwise pronounced, sideward migration of analytes towards the end of an electrophoretic run.

Protein analytes were made visible by staining SDS-PAGE gel slabs in a heated Coomassie staining solution (see also Table 6.6) in a glass beaker and incubated for 5 to 10 min under mild agitation. The staining solution was then discarded and stained SDS-PAGE gel slabs were rinsed with deionized water. A glass beaker was filled to one third with deionized water, a stained SDS-PAGE gel slab and boiling pebbles added. The water was brought to the boil in a microwave and maintained boiling

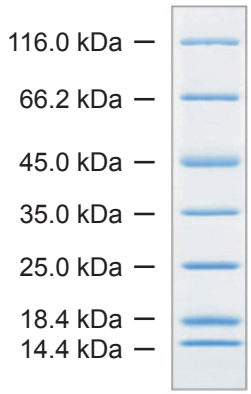

Figure 6.1.: SDS-PAGE band profile of "Pierce Unstained Molecular Weight Marker" 26610 provided by Thermo Scientific (Thermo Scientific, Schwerte, Germany), stained with Coomassie blue. Protein concentrations vary from 0.1 to 0.2 g/ml (http://www.piercenet.com/product/pierce-unstained-protein-mw-marker).

for at least 10 min. Stained deionized water was discarded and this process was repeated until destaining of SDS-PAGE gel slabs was sufficient. Destained SDS-PAGE gel slabs were photographically documented using a Geldoc 2000 system (BioRad, München, Germany).

6.4.4. UV / Vis Spectroscopy

Spectrophotometric measurements of protein samples in the ultra-violet and visible range (UV / Vis) were recorded by a Lambda 25 UV / Vis spectrophotometer (Perkin Elmer, Waltham, USA). Concentrations resulting from absorption measurements were calculated from Lambert-Beer-proportionality which predicts a linear dependence between an analyte's concentration and absorption between 0.1 and 1.0 absorption units. Bacterial cell densities were measured at 600 nm (OD_600) in disposable cuvettes, while protein concentrations were calculated from their UV-absorption at 280 nm in 200 µl quartz micro cuvettes (Hellma, Müllheim, Germany) and the extinction coefficient calculated by ExPASy's ProtParam tool (http://web.expasy.org/protparam/) in protein buffer. The extinction coefficient of LC3C was determined to be 8940 M^{-1} cm^{-1}. All UV / Vis spectroscopic measurements were repeated three times and the arithmetic mean calculated.

6.5. Protein Crystallography

6.5.1. Crystallisation

The crystallisation of a protein is regarded as a multi-parameter problem depending on–but not limited to–temperature, chemical potential, and changes of protein hydration in the phase transition from a soluble to an ordered insoluble or crystallised state (Rupp, 2009). Although algorithms can predict crystallisation probability (e.g. XtalPred (Slabinski et al., 2007)), whether, and how, a protein adopts an ordered, solid state still needs to be determined empirically.

In this work, protein solutions were dispensed by a pipetting robot (Freedom EVO, Tecan, Männedorf, Switzerland) into multi-well, sitting-drop crystallisation plates (96-well, Greiner BioOne, Frickenhausen, Germany) to coarse screen crystallisation conditions. Commonly, 70 µl of a crystallisation screening solution was transferred to a plate's reservoir, then 0.4 µl protein solution was placed in the sitting-drop well, and 0.4 µl reservoir solution was added to the sitting drop. Evaporation of solvents during pipetting steps was decreased by a mobile lid placed over the crystallisation plate. 96-well crystallisation plates were sealed by an adhesive, transparent foil (Greiner BioOne, Frickenhausen, Germany) and incubated under controlled temperature conditions in the dark.

Screening kits are listed in Table 6.4. Every screening-kit condition was tested with at least three protein concentrations (most notably 4, 8, and 12 mg/ml) and three incubation temperatures (RT, 16 °C, and 6 °C). If applicable, higher protein concentrations were tested. LC3C was concentrated in SEC buffer (buffer composition see Table 6.5) as described in Section 6.3.4 and protein concentrations were determined via UV / Vis spectroscopy as described in Section 6.4.4.

The outcome of crystallisation experiments was examined by a stereo microscope at RT, after three days incubation at the earliest. Experiments were then re-evaluated in regular intervals up to several months after the initial set-up. Successful crystallisation conditions were further investigated by manual hanging-drop crystallisation experiments. Here, reservoir solutions were dispensed into cell culture plate wells (24 well, Cellstar, Greiner BioOne, Frickenhausen, Germany). The raised rim of each well was prepared by polydimethylsiloxane grease (Baysilone mittelviskos, VWR, Darmstadt, Germany). Protein (1 µl) and reservoir solutions (1 µl) were mixed in the center

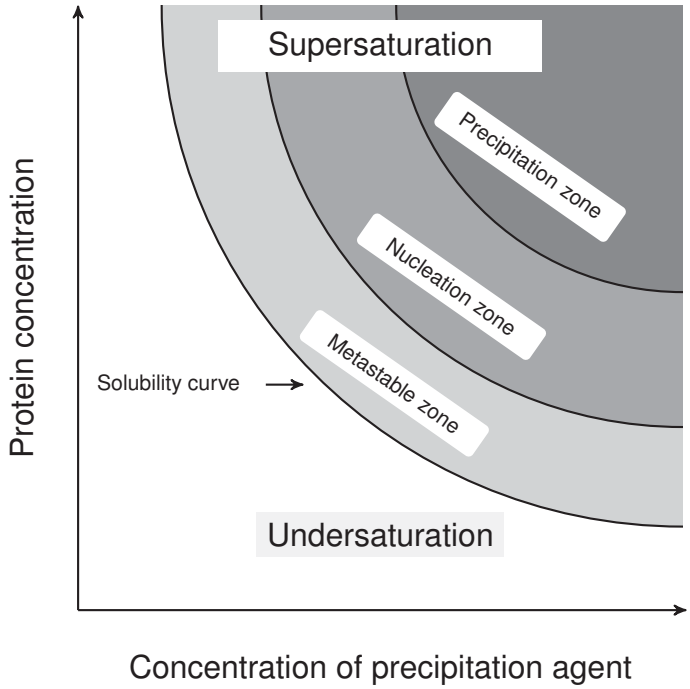

Figure 6.2.: Idealised phase diagram for protein crystallisation.

of a circular, hydrophobic glass cover-slip and positioned as a hanging-drop above a reservoir. Sealing of the cover-slip with the greased well rim was inspected visually.

6.5.2. Crystal Seeding

By using crystallisation seeds, crystallisation conditions that might be thermodynamically unfavourable towards nucleation, but ideally suited for crystal growth, can still be exploited. To generate a crystal seed stock, protein crystals were collected in 50 µl mother-liquor in a 1.5 ml reaction tube. A small plastic-bead was added and the closed reaction tube was vortexed. Cross-micro-seeding experiments were set up by adding 0.25 µl of the seed suspension to sitting-drops of a 96-well crystallisation experiment by a pipetting robot, analogous to the coarse screening protocol described in Section 6.5.1. Manual seeding of crystallisation drops was accomplished by streak-seeding with a seeding hair, using vortexed or crushed protein crystals as seed stock.

6.5.3. Controlled Dehydration

Controlled dehydration of protein crystals has been reported to improve obtainable resolution of protein crystals, possibly as a result of an increased order in the crystal lattice due to improved crystal packing when a solvent is evaporated (Heras et al., 2003; Heras and Martin, 2005; Wheeler et al., 2012). In controlled dehydration experiments, 24-well plates were used (Cellstar, Greiner BioOne, Frickenhausen, Germany). A cover-slip with a crystallisation drop containing protein crystals was detached from the original reservoir and placed above fresh reservoir solution containing an increased precipitant concentration (e.g., 2.0 to 2.5 M NaCl, 2.5 to 3.0 M NaCl). Then the crystallisation drop was equilibrated for at least 72 h at RT and the experiment repeated with a higher precipitant concentration. During equilibration, the water content of a crystallisation drop is slowly reduced, and thereby, possibly, the crystal's water content decreased.

6.5.4. Cryo-Crystallography

Modern protein crystallography is mainly performed at reduced temperature instrumental in decreasing radiation damage of sensitive protein crystals. For this, protein crystals are commonly equilibrated in a cryo-solution before flash cooling to a cryo-temperature of 100 K, thereby protecting protein crystals from ice formation which would normally occur during this temperature shift.

Protein crystals were prepared from crystallisation drops using nylon loops (CryoLoop, Hampton Research, Aliso Viejo, USA) and then flash-cooled in a stream of dried nitrogen gas at 100 K (Cryostream, Oxford Cryosystems, Oxford, United Kingdom). If a crystallisation solution remained clear when flash-cooled, respective crystals were isolated and tested in diffraction experiments. Otherwise, cryo-additives (e.g., 5-25% glycerol, PEG 800, PEG 3350, MPD, sucrose) were tested with a protein's crystallisation solution and crystals evaluated after a short incubation in the modified buffer. A compatible cryo-additive leads to a glass-like mother-liquor in the loop at 100 K and, ideally, to an improved diffraction experiment with low susceptibility of a protein crystal to radiation damage.

6.6. Nuclear Magnetic Resonance Spectroscopy

Nuclear magnetic resonance (NMR) spectroscopy relies on NMR active, ^{15}N and ^{13}C spin-½ nuclei. While the natural abundance of these nuclei is very low, proteins used for NMR experiments were expressed by *E. coli* in growth media containing exclusively ^{15}N- and / or ^{13}C-labelled nitrogen and / or carbon sources. Adapted protocols for ^{15}N- and / or ^{13}C-labelled protein expression are described in Section 6.3.1. Furthermore, NMR protein sample preparation is illustrated in Section 6.6.1 whereas data acquisition parameters and processing procedures are depicted in Section 6.6.2. Additionally, structural restraints used to calculate LC3C's NMR ensemble structures are specified in Section 6.6.4.

6.6.1. Sample Preparation

Protein samples to be examined by NMR spectroscopy were transferred to an optimised NMR buffer by size-exclusion chromatography in the last step of the LC3C purification scheme and NMR buffer composition is given in Table 6.5. Then, protein samples were concentrated as described in Section 6.3.4 and resulting concentrations were determined as described in Section 6.4.4. Generally, NMR samples contained between 370 and 760 µM LC3C protein.

The NMR protein buffer was supplemented with 2% (v/v) glycerol-D_8 (Euriso-top, Gif-sur-Yvette, France) which was added to a concentrated protein solution and subsequently carefully homogenised. NMR protein samples were then adjusted with 10% (v/v) ^2H_2O for the NMR deuterium-lock signal and were centrifuged for 20 min at 8 °C at maximum centripetal force in a pre-chilled benchtop centrifuge. Finally, 360 to 400 µl of the NMR protein sample was carefully transferred into a 5 mm ^2H_2O-matched Shigemi tube (BMS-005, VWR, Darmstadt, Germany).

As residual water resonance signal can overlap with important NMR resonance signals, H_2O was exchanged with ^2H_2O by ultrafiltration or lyophilisation of an NMR protein sample when appropriate. Exchange by ultrafiltration was achieved in 500 µl spin-columns (Amicon Ultra, 3,000 Da NMWL, Millipore, Schwalbach, Germany), as described in Section 6.3.4. To this end, the volume of an NMR protein sample was halved and subsequently carefully readjusted to the initial volume with a ^2H_2O-based buffer (^2H_2O > 99.9%). This process was repeated at least ten times, thereby reducing

H_2O concentration to less than 0.1%-within the range of H_2O impurities of the ^2H_2O solvent.

Exchange by lyophilisation was accomplished by supplementing an NMR protein sample with 2% (v/v) glycerol-D_8 and then lyophilising the NMR protein sample overnight (as summarised in Section 6.3.5). The resulting gel-like protein concentrate or protein powder was (re-)solved in ^2H_2O (> 99.9%), centrifuged for 10 min at 8 °C and maximum centripetal force to immobilise and remove unsoluble protein aggregates. In a final step, the ^2H_2O NMR protein sample was transferred into a matched Shigemi tube.

6.6.2. Acquisition & Processing of NMR Data

All NMR experiments were recorded at 20.0 °C on Varian INOVA or Bruker AVANCE III spectrometers operating at ^1H frequencies of 600 or 800 MHz. Probes were cryogenically cooled and possessed triple or quadruple resonance and pulse-field gradient capabilities. Chemical shifts of ^1H-protons were referenced to an external DSS (4,4-dimethyl-4-silapentane-1-sulfonic acid) sample. ^{13}C and ^{15}N chemical shifts were referenced indirectly using magnetogyric ratios (Markley et al., 1998).

Acquisition parameters are summarised in Table 6.20. NMR data was processed by using a sine-bell apodization function and zero-filling. If applicable, an automatic baseline correcting function was enabled. All NMR data was processed using NMRPipe and NMRDraw (Delaglio et al., 1995). Processed spectra were initially assessed by NMRDraw and evaluated in detail with NMRView 9.0.0.b114 (One Moon Scientific, Inc.), and CcpNmr Analysis 2.4.1 (Vranken et al., 2005).

Table 6.20.: Acquisition and processing parameters of NMR experiments.

Experiment	sw1 [ppm]	sw2 [ppm]	sw3 [ppm]	t1 [pt]	t2 [pt]	t3 [pt]	nt #	d1 [s]	mix [ms]	ω1 [pt]	ω2 [pt]	ω3 [pt]
2D [^{1}H-^{15}N] HSQC	16.0	31.0	–	614	192	–	8	1.5	–	1228	384	–
2D [^{1}H-^{13}C] ct-HSQC	16.0	140.0	–	1024	506	–	32	1.1	–	2048	1012	–
3D HNCO	16.0	31.0	15.1	1024	32	40	16	1.05	–	2048	64	80
3D HNCA	16.0	31.0	26.0	1024	32	48	16	1.5	–	2048	64	96
3D HNCACB	16.0	31.0	59.0	1024	32	48	48	1.5	–	2048	64	96
3D CBCA(CO)NH	16.0	31.0	59.0	1024	32	48	64	1.5	–	2048	64	96
3D HC(CO)NH	16.0	31.0	70.0	1024	32	64	48	1	–	2048	64	128
3D (H)CCH-COSY	16.0	30.0	70.0	1024	28	64	32	1.1	–	2048	56	128
3D HNHA	16.0	31.0	12.0	1024	32	48	32	1.2	12.3	2048	64	96
3D HBHA(CO)NH	16.0	31.0	6.0	1024	32	64	32	1.0	–	2048	64	128
3D H(C)CH-COSY	16.0	30.0	7.0	1024	28	72	–	–	20	2048	28	72
3D HC(C)H-TOCSY	16.0	10.0	30.0	512	86	32	16	2.0	–	1024	172	64
3D [^{1}H-^{15}N] TOCSY-HSQC	16.0	12.0	31.0	614	128	22	64	1.0	–	1228	256	44
2D [^{1}H-^{1}H] TOCSY	16.0	31.0	–	1024	512	–	32	1.5	–	2048	1024	–
3D [^{1}H-^{15}N] [^{1}H-^{15}N] HSQC-NOESY-HSQC	614	128	16.0	16.0	31.0	32	32	1.0	120	1228	256	64
3D [^{1}H-^{13}C] [^{1}H-^{15}N] HSQC-NOESY-HSQC	512	32	16.0	30.0	12.0	128	16	1.0	120	1024	64	256
2D ^{1}H-^{1}H-NOESY	1024	512	16.0	14.0	–	–	48	1.5	120	2048	1024	–
2D ^{15}N {^{1}H}-NOE	16.1	31.0	–	825	96	–	16	15.0,9.0	–	1650	192	–
T_1-Relaxation	16.0	31.0	–	1024	96	–	16	2.6	–	2048	192	–
$T_{1\rho}$-Relaxation	16.0	31.0	–	1024	96	–	16	3.0	–	2048	192	–
[^{1}H-^{15}N] SQ-CPMG	16.0	31.0	–	614	96	–	16	2.5	–	1228	192	–

6.6.3. Resonance Assignments

Sequence-specific assignment of backbone resonances followed [^{1}H-^{15}N] HSQC, HNCA (Bax and Ikura, 1991), HNCACB (Wittekind and Muller, 1993), CBCA(CO)NH (Grzesiek et al., 1993), and C(CO)NH (Grzesiek et al., 1993) experiments. Chemical shifts of backbone carbonyl groups were extracted from an HNCO experiment (Ikura et al., 1990).

Side-chain resonances were assigned by analysis of [^{1}H-^{13}C] ct-HSQC, HNHA (Vuister and Bax, 1993), HBHA(CO)NH (Grzesiek and Bax, 1993), HC(CO)NH, [^{1}H-^{15}N] TOCSY-HSQC, (H)CCH-COSY, H(C)CH-COSY, HC(C)H-TOCSY (Kovacs and Gossert, 2014), and 2D [^{1}H-^{1}H] TOCSY experiments. Assignments of aromatic side-chains were obtained from HC(C)H-TOCSY (Kovacs and Gossert, 2014), [^{1}H-^{15}N] NOESY-HSQC, and [^{1}H-^{13}C] NOESY-HSQC experiments. Assignments have been deposited with the Biological Magnetic Resonance Data Bank and can be accessed by the accession number 26603.

6.6.4. Structural Restraints

Determination of biomolecular structures by solution-state NMR is commonly based on data derived from nuclear Overhauser effect (NOE). In NOE spectroscopy (NOESY), nuclear magnetic spin polarisation is transferred through space to spatially close, NMR-sensitive nuclei. The intensity of the magnetisation transfer between nuclei is inversely proportional to the sixth power of their distance. Thus making it possible to derive distance information by measuring cross peak intensities. Ideally, NOESY leads to a concise collection of distance information for the majority of ^{1}H-nuclei of a biomolecule. Still, ambiguity in NOESY assignments due to spectral overlap, conformational heterogeneity, protein dynamics or line broadening, may still result in uncertainty of derived distance informations and higher local displacement values.

Apart from distance restraints, restraints based on backbone dihedral angles Φ and Ψ, residual dipolar couplings, or hydrogen-bond donor/acceptor pairs may correct for inaccuracy in NOESY data. In this work, backbone dihedral angles and hydrogen-bond pairs were used.

NOE Assignments and Distance Restraints

Assignments and interpretation of NOE spectra remain the most time consuming step in the structural characterisation of a biomolecule by NMR spectroscopy. Commonly, assignments are hindered by NMR line-broadening, overlapping signals, or poor signal-to-noise-ratios that lead to decreased spectral quality.

For LC3C, proton-proton distance information was derived from [^{1}H-^{13}C] NOESY-HSQC (120 ms mixing time), 3D [^{1}H-^{15}N] [^{1}H-^{15}N] HSQC-NOESY-HSQC (150 ms mixing time), and 3D [^{1}H-^{13}C] [^{1}H-^{15}N] HSQC-NOESY-HSQC (150 ms mixing time) experiments (Sattler et al., 1999; Cavanagh et al., 2007).

Assignments of NOESY data were semi-automatically accomplished with ARIA 2 and analysed with CcpNmr Analysis 2.4.1 (Vranken et al., 2005; Nilges, 1995; Nilges et al., 1997; Linge et al., 2001). Frequency windows used in ARIA's routines were optimised (Fossi et al., 2005). For the 3D [^{1}H-^{15}N] [^{1}H-^{15}N] HSQC-NOESY-HSQC spectrum and aliphatic resonances of the 3D [^{1}H-^{13}C] [^{1}H-^{15}N] HSQC-NOESY-HSQC spectrum, cutoff frequency windows for automated assignments were set to 0.02 ppm, and 0.04 ppm for direct, and indirect dimension, respectively, and to 0.2 ppm for ^{15}N or ^{13}C nuclei. NOESY peaks belonging to aromatic side-chains, were assigned by frequency windows of 0.05 ppm for the direct, 0.02 ppm the indirect ^{1}H dimension, and 0.5 ppm for ^{13}C nuclei, due to a lowered signal-to-noise ratio in the aromatic parts of the [^{1}H-^{13}C] [^{1}H-^{15}N] HSQC-NOESY-HSQC spectrum. Additionally, a 2D [^{1}H-^{13}C] NOESY-HSQC experiment was recorded and used in later stages of the structure calculation process. Due to spectral overlap, a NOE peak in the 2D [^{1}H-^{13}C] NOESY-HSQC spectrum< was only assigned if a symmetry-related peak existed and the chemical shift was well defined. After semi-automatical assignments, all ARIA suggestions were vigorously reevaluated at all stages of the model building process.

J-Coupling And Dihedral Restraints

Dihedral restraints resulting from LC3C's residues backbone conformation were derived experimentally from the three bond scalar coupling constant $^{3}J_{HNH\alpha}$. This constant represents the magnitude of scalar coupling between a residue's backbone amide and α-proton. $^{3}J_{HNH\alpha}$ depends on conformational arrangement of amide and α-proton and varies most between a staggered and eclipsed conformation (Jacobsen,

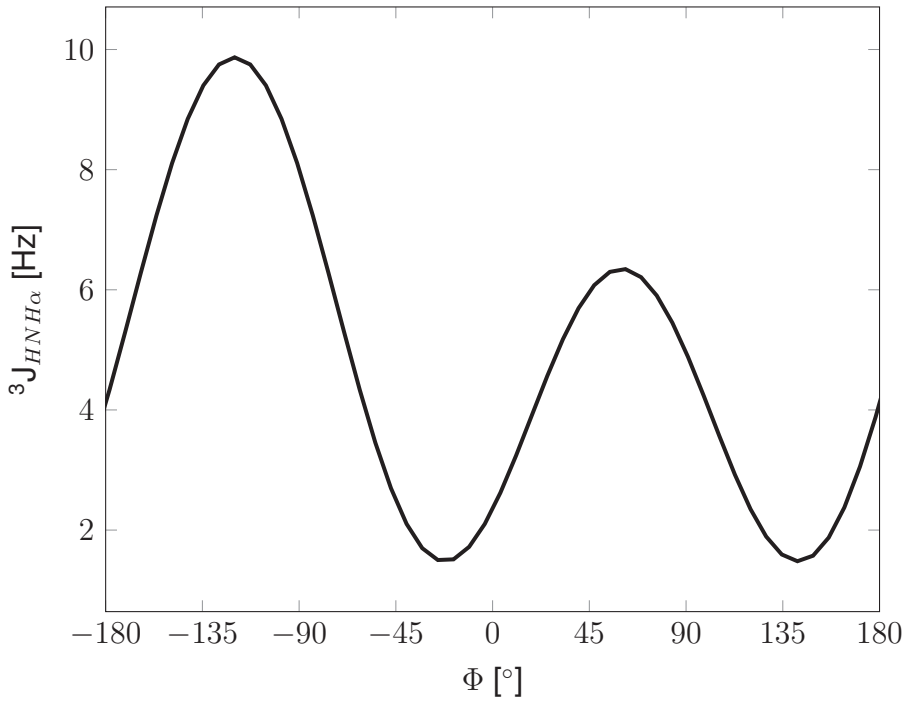

Figure 6.3.: Coupling constant $^3J_{HNH\alpha}$ plotted as function of the dihedral angle Φ according to the Karplus relation (Karplus and Anderson, 1959).

2007). With knowledge of $^3J_{HNH\alpha}$, backbone dihedral angle Φ can be calculated by the Karplus relation (Karplus and Anderson, 1959; see also Figure 6.3):

$$J = A\,cos^2(\Phi - 60) + B\,cos(\Phi - 60) + C \tag{6.1}$$

where parameters $A = 6.51$, $B = -1.76$, and $C = 1.60$ depend upon the involved nuclei (Vuister and Bax, 1993; Cavanagh et al., 2007). Coupling constant $^3J_{HNH\alpha}$ was calculated in CcpNMR Analysis 2.4.1 from intensity ratios of cross and diagonal peaks of a quantitative HNHA experiment (Vuister and Bax, 1994; Zhang et al., 1997):

$$^3J_{HNH\alpha} = C\,\frac{1}{2\pi\,\delta}\,arctan\sqrt{-\frac{I_c}{I_d}} \tag{6.2}$$

where $\delta = 12.3$ ms is the coherence transfer time and $C = 1.10$ represents a scaling factor correcting for the molecular weight of LC3C (Cavanagh et al., 2007).

$^3J_{HNH\alpha}$ is influenced by motional averaging (Hyberts et al., 1987). Typical for unstructured peptides are $^3J_{HNH\alpha}$ values of circa 7.0 Hz (Cavanagh et al., 2007).

Therefore, $^3J_{HNH\alpha}$ values between 6 Hz and 8 Hz were excluded for Φ calculations. Whereas $^3J_{HNH\alpha} < 4.0$ Hz is characteristic in an α-helical environment and $^3J_{HNH\alpha} > 8.0$ Hz is typical for residues involved in β-strand formation.

Additionally, the TALOS-N (torsion angle likeliness obtained from shift and sequence similarity) algorithm was used to predict Φ and Ψ backbone dihedral angles (Shen and Bax, 2013). TALOS-N uses an artificial neural network in combination with a database search containing information about 7-mer peptide sequences sequentially matching the protein of interest's sequence and its chemical shift assignments as input data.

Hydrogen Bond Restraints

Hydrogen bonds are essential for formation of biomoleculur structures. Therefore, identifying hydrogen bond donor-acceptor pairs may provide essential structural information. Particularly hydrogen bonds formed by backbone amide protons are important in formation of secondary and tertiary structures of proteins. Amide protons exchange over time with protons of the surrounding protogenic solvent, provided the particular proton is not involved in a hydrogen bond; in which case, the amide proton's exchange rate will be significantly quenched.

In NMR spectroscopy this behaviour is escpecially interesting as an exchange of a NMR-sensitive ^1H amide proton for an NMR-inactive ^2H is easily achieved by changing the solvent from ^1H_2O to ^2H_2O (H/D-exchange). Subsequently, amide hydrogens likely involved in hydrogen bonds can be identified as their signal intensity persists over time in a time-dependent series of 2D [^1H-^{15}N] HSQC correlation spectra.

In secondary structure elements like α-helices and β-sheets respective hydrogen bond acceptors are well documented and incorporated as structural restraints (Wüthrich, 1986). Other hydrogen bond acceptors were identified by spatial proximitiy in comparison with an ensemble structure obtained without applying any hydrogen bond restraints. H/D-exchange rates were semiquantitatively analysed by using CcpNMR Analysis' internal routines (menu 'Data Analysis' - 'Follow Intensity Changes').

Hydrogens bonds present in LC3C were identified by lyophilising the protein as described in Section 6.3.5 and dissolved in ^2H_2O resulting in an NMR sample with a final concentration of 760 μM. A series of 2D [^1H-^{15}N] HSQC spectra were recorded over the course of eighteen hours while data acquisition was finished after 0.3, 1.6,

2.8, 5.4, 7.9, 12.9, and 17.9 h, respectively. An amide proton was classified as hydrogen bond donor if the signal existed beyond 2.8 h due to its slow exchange rate. A hydrogen bond's structural restraint's lower and upper distance limit was set to 1.5 and 2.3 Å, respectively, in CcpnNMR Analysis.

6.6.5. Structure Calculation with ARIA / CNS

Ensemble structures of LC3C based on NOESY distance information, dihedral angle restraints, and hydrogen bond restraints were computed by ARIA 2 / CNS 1.21 (Nilges, 1995; Nilges et al., 1997; Linge et al., 2001; Habeck et al., 2004; Rieping et al., 2007; Brünger et al., 1998). ARIA (Ambiguous Restraints for Iterative Assignment) was instructed to import NOE peak lists, dihedral angle restraints, and hydrogen bond restraints from a CcpNMR Analysis project. ARIA / CNS structural ensembles were then exported back to CcpNmr Analysis for inspection.

Beginning from a stretched protein conformation and without prior knowledge of a protein's structure, ARIA / CNS performs an iterative approach for NOE cross peaks assignments and resulting distance restraints. In each new iteration, a predefined number of lowest total energy structures are used as the starting data set to reevalute NOE cross peak assignments and distance restraints. The distance violation tolerance parameter is lowered in succeeding iterations, which ideally resolves ambigous NOE assignments.

Overall, ARIA / CNS uses eight iterations of model calculations *in vacuo*, followed by a water refinement step of the ten lowest energy structures, which improves structure quality (Rieping et al., 2007). In this work, ARIA / CNS was instructed to use a 'flat-bottom harmonic potential' with an automated restraint weighting in the second cooling phase (Nilges et al., 2008). Molecular dynamics (MD) calculation parameters are listed in Table 6.22. ARIA's standard parameters have been adjusted to decelerate cooling rates (Cool1, Cool2). All user adjustable ARIA parameters have been described in-depth elsewhere (Lecher, 2011). The ARIA configuration file in xml-format containing all ARIA / CNS variables and parameters is listed in the appendix.Ensemble structures were analysed and inspected with CcpNMR Analysis (Vranken et al., 2005), iCing (Doreleijers et al., 2012), PyMOL 1.7.2.1 (Schrödinger, LLC, 2014), PROCHECK-NMR (Laskowski et al., 1993) and MolProbity (Chen et al., 2010).

Table 6.22.: Molecular dynamics parameters used by CNS.

Parameter	Value
TAD high temperature	10000.0
TAD time-step factor	9.0
Cartesian high temperature	2000.0
Cartesian 1st iteration	0
Time-step	0.003
Cool1 final temperature	1000.0
Cool2 final temperature	50.0
High-temp steps	10000
Refine steps	4000
Cool1 steps	20000
Cool2 steps	20000

6.6.6. Structural Dynamics

A decisive advantage of NMR spectroscopy in comparison to other biophysical techniqiues is the possibility to determine not only information on the fixed, three dimensional structure of a biomolecule but also on structural dynamics. In this work, the structural dynamics of LC3C's backbone amide groups were investigated on the fast picosecond to nanosecond (ps-ns) time scale and in slower time regimes from milliseconds to hours.

Fast dynamics was analysed by computating longitudinal relaxation rates (R_1) in dependence of delay times between 80 ms and 1200 ms and transversal relaxation rates (R_2) following $T_{1\rho}$ experiments with delay times between 10 ms and 100 ms and a 2.0 kHz spin-lock field (Lakomek et al., 2012), recorded at 600 and 800 MHz and 20 °C. Heteronuclear NOE (hetNOE) experiments were recorded at 600 MHz in presence and absence of a 3.6 s pre-saturation pulse (Kay et al., 1989).

Subsequently, a generalised squared order parameter S^2 was calculated by the model-free approach with Tensor 2.0 on the basis of R_1 and R_2 relaxation rates, and hetNOE values for backbone amide protons (Lipari and Szabo, 1982a,b; Dosset et al.,

2000). In this work, each S^2 value ($0 \leq S^2 \leq 1$) characterises an intramolecular motional amplitude of an amide group, while a backbone's amide S^2 = 1.0 indicates absolute rigidity on the fast ps-ns time scale (Cavanagh et al., 2007).

Structural dynamics of LC3C on the microsecond to millisecond time scale were researched by ^{15}N CPMG (Carr-Purcell-Meiboom-Gill) relaxation dispersion (RD) experiments (Loria et al., 1999; Tollinger et al., 2001). This intermediate time scale allows observation of dynamical processes such as chain rotations, loop motions or secondary structure changes. CPMG RD experiments rely on a series of of spin-echo pulse elements (τ–180–τ) that refocus exchange broadening occuring during the spin-echo delay τ. If a spin experiences a different chemical shift during the spin-echo delay, e.g. due to dynamical processes, refocusing will be incomplete and line broadening will occur. Thus allowing allowing the determination of exchange rates between two states A and B, population occupancy of these states, or chemical shift differences between A and B (Kleckner and Foster, 2011).

Finally, the slow time scale (seconds to hours) was assessed by identifying H/D-exchange rates. These exchange experiments were analysed with CcpnNMR Analysis (experiments recorded as described in Section 6.6.4), while relaxation experiments were interpretated using NMRView and MUNIN (Orekhov et al., 2001).

6.6.7. *In-vitro* Phosphorylation of LC3C

In this work, *in vitro* phosphorylation of LC3C was studied as a model for the post-translational modification of autophagic proteins. Particular interest was focused on the observation of phosphorylation by NMR spectroscopy. LC3C's phosphorylation site was identified by sequence homology to a conserved LC3A site (Cherra et al., 2010) and by prediction algorithms based on LC3C's protein sequence (NetPhos http://www.cbs.dtu.dk/services/NetPhos/, and NetPhosK http://www.cbs.dtu.dk/services/NetPhosK/).

In vitro phosphorylation of LC3C was initiated by adding catalytical amounts of murine protein kinase A (PKA; NEB, Frankfurt a. M., Germany) to a concentrated and isotopically labelled LC3C sample in NMR buffer. Additionally, phosphorylation of LC3C by PKA required ATP, and Mg^{2+}-ions as co-factors. The influence on the [*U*-^{15}N,^{13}C]-labelled LC3C fingerprint 2D [^{1}H-^{15}N] HSQC spectrum was tested for each co-factor separately and in combination. The *in vitro* phosphorylation reaction

of LC3C was initiated by adding 0.5 µl PKA solution (circa 1000 u) to a cold, concentrated LC3C sample (600 to 700 µM, 6 °C) in NMR buffer containing 1 mM ATP and 5 mM $MgCl_2$–each co-factor was added to the NMR buffer from a concentrated (1000 x), sterile filtered stock solution. The NMR sample was carefully homgenised, centrifuged for 5 min at RT in a bench-top centrifuge, and transferred into a 5 mm Shigemi tube for NMR experiments. All 2D [^{1}H-^{15}N] HSQC spectra were recorded at a ^{1}H frequency of 600 MHz and at 20 °C.

The reaction progress was then observed and followed by twelve consecutive 2D [^{1}H-^{15}N] HSQC spectra (acquisition completed after 3.5, 7.0, ..., 21.0, 25.4, 28.9, ..., 44.9 h). Additionally, 2D ^{1}H-^{13}C ct-HSQC and 3D HNCA experiments were recorded. As modification of a protein's target side-chain by phosphorylation introduces a strong point charge, spatially close local magnetic fields will most likely be influenced. Thus the impact on the chemical shifts of backbone amide resonances was analysed.

After 72 h, 5 µl of [*U*-^{15}N,^{13}C]-labelled LC3C was isolated and analysed by proteolytic hydrolysis (trypsin, Glu-C) followed by MALDI-LTQ-Orbitrap MS/MS (LTQ-Orbitrap XL, Thermo Scientific, Schwerte, Germany) in cooperation with ZEA-3 (Forschungszentrum Jülich, Germany).

7. Abbreviations

2D	Two-dimensional
3D	Three-dimensional
Atg	Autophagy-related
Amp	Ampicillin
ATP	Adenosine triphosphate
ARIA	Ambigous restraints for iterative assignment
BMRB	Biological Magnetic Resonance Data Bank
Cam	Chloramphenicol
CD	Circular dichroism
CNS	Crystallographic and NMR system
CPMG	Carr-Purcell-Meiboom-Gill
ct	Constant time
CV	Column volume
Da	Dalton
DLS	Dynamic light scattering
DNA	Deoxyribonucleic acid
ϵ	Molar extinction coefficient
EDTA	Ethylenediaminetetraacetic acid
E. coli	*Escherichia coli*
FPLC	Fast protein liquid chromatography
g	Gravitational acceleration
GABARAP	γ-aminobutyric acid type A receptor-associated protein
GSH	Glutathione
GST	Glutathione S-transferase
HetNOE	Heteronuclear (nuclear) Overhauser effect
HSQC	Heteronuclear single quantum coherence
IPTG	Isopropyl β-D-1-thiogalactopyranoside

LB	Lysogeny broth
LC3C	Microtubulus-associated protein 1 light chain 3C
M9	Minimal medium 9
min	Minute, minutes
MPD	2-Methyl-2,4-pentanediol
MWCO	Molecular weight cut off
NOE(SY)	Nuclear Overhauser effect / enhancement (spectroscopy)
NMWL	Nominal molecular weight limit
OD	Optical density
p.a.	*pro analysi*
PAGE	Polyacrylamide gel electrophoresis
PBS	Phosphate buffered saline
PCR	Polymerase chain reaction
PDB	Protein data bank
PE	Phosphatidylethanolamine
PEG	Polyethylene glycol
PIPES	1,4-Piperazinediethanesulfonic acid
PMSF	Phenylmethanesulfonyl fluoride
PPM	Parts per million
pt	Points
RD	Relaxation dispersion
RT	Room temperature
SAP	Shrimp alkaline phosphatase
SDS	Sodium dodecyl sulphate
SEC	Size exclusion chromatography
SOB	Super optimal broth
SOC	Super optimal broth, with catabolite repression
TALOS	Torsion angle likelihood obtained from shift and sequence similarity
TBS	Tris buffered saline
TEMED	N,N,N',N'-Tetramethylethane-1,2-diamine
Tris	2-Amino-2-hydroxymethyl-propane-1,3-diol
TS	Trace element solution
UV	Ultraviolet
V	Volume

(v/v)	Volume to volume ratio
(w/v)	Weight to volume ratio

8. Bibliography

Alemu, E. A., Lamark, T., Torgersen, K. M., Birgisdottir, A. B., Larsen, K. B., Jain, A., Olsvik, H., Øvervatn, A., Kirkin, V., and Johansen, T. (2012). ATG8 family proteins act as scaffolds for assembly of the ULK complex: sequence requirements for LC3-interacting region (LIR) motifs. J. Biol. Chem., 287(47):39275–39290.

Ashford, T. P. and Porter, K. R. (1962). Cytoplasmic components in hepatic cell lysosomes. J. Cell Biol., 12:198–202.

Bampton, E. T., Goemans, C. G., Niranjan, D., Mizushima, N., and Tolkovsky, A. M. (2005). The dynamics of autophagy visualized in live cells: from autophagosome formation to fusion with endo/lysosomes. Autophagy, 1(1):23–36.

Bavro, V. N., Sola, M., Bracher, A., Kneussel, M., Betz, H., and Weissenhorn, W. (2002). Crystal structure of the GABA(A)-receptor-associated protein, GABARAP. EMBO Rep., 3(2):183–189.

Bax, A. and Ikura, M. (1991). An efficient 3d nmr technique for correlating the proton and 15n backbone amide resonances with the α-carbon of the preceding residue in uniformly 15n/13c enriched proteins. J. Biomol. NMR, 1(1):99–104.

Brünger, A. T., Adams, P. D., Clore, G. M., DeLano, W. L., Gros, P., Grosse-Kunstleve, R. W., Jiang, J. S., Kuszewski, J., Nilges, M., Pannu, N. S., Read, R. J., Rice, L. M., Simonson, T., and Warren, G. L. (1998). Crystallography & NMR system: A new software suite for macromolecular structure determination. Acta Crystallogr. D Biol. Crystallogr., 54(Pt 5):905–921.

Burroughs, A. M., Balaji, S., Iyer, L. M., and Aravind, L. (2007a). A novel superfamily containing the beta-grasp fold involved in binding diverse soluble ligands. Biol. Direct, 2:4.

Burroughs, A. M., Balaji, S., Iyer, L. M., and Aravind, L. (2007b). Small but versatile: the extraordinary functional and structural diversity of the beta-grasp fold. Biology Direct, 2(1).

Cavanagh, J., Fairbrother, W. J., Palmer, A. G., Rance, M., and Skelton, N. J. (2007). Protein NMR Specgtroscopy - Principles and Practice. Academic Press, 2nd edition.

Ceccarelli, D. F., Song, H. K., Poy, F., Schaller, M. D., and Eck, M. J. (2006). Crystal structure of the FERM domain of focal adhesion kinase. J. Biol. Chem., 281(1):252–259.

Chen, V. B., Arendall, W. B., Headd, J. J., Keedy, D. A., Immormino, R. M., Kapral, G. J., Murray, L. W., Richardson, J. S., and Richardson, D. C. (2010). MolProbity: all-atom structure validation for macromolecular crystallography. Acta Crystallogr. D Biol. Crystallogr., 66(Pt 1):12–21.

Cherra, S. J., Kulich, S. M., Uechi, G., Balasubramani, M., Mountzouris, J., Day, B. W., and Chu, C. T. (2010). Regulation of the autophagy protein LC3 by phosphorylation. J. Cell Biol., 190(4):533–539.

Clark, S. L. (1957). Cellular differentiation in the kidneys of newborn mice studies with the electron microscope. J. Biophys. Biochem. Cytol., 3(3):349–362.

Cohen, S. N., Chang, A. C., and Hsu, L. (1972). Nonchromosomal antibiotic resistance in bacteria: genetic transformation of Escherichia coli by R-factor DNA. PNAS, 69(8):2110–2114.

Coyle, J. E., Qamar, S., Rajashankar, K. R., and Nikolov, D. B. (2002). Structure of GABARAP in two conformations: implications for GABA(A) receptor localization and tubulin binding. Neuron, 33(1):63–74.

Delaglio, F., Grzesiek, S., Vuister, G. W., G., Z., Pfeifer, J., and Bax, A. (1995). NMRPipe: a multidimensional spectral processing system based on UNIX popes. J. Biomol. NMR, 6(3):277–293.

Doreleijers, J. F., Sousa da Silva, A. W., Krieger, E., Nabuurs, S. B., Spronk, C. A., Stevens, T. J., Vranken, W. F., Vriend, G., and Vuister, G. W. (2012). CING:

an integrated residue-based structure validation program suite. J. Biomol. NMR, 54(3):267–283.

Dosset, P., Hus, J. C., Blackledge, M., and Marion, D. (2000). Efficient analysis of macromolecular rotational diffusion from heteronuclear relaxation data. J. Biomol. NMR, 16(1):23–28.

Dunn, W. A., Cregg, J. M., Kiel, J. A., van der Klei, I. J., Oku, M., Sakai, Y., Sibirny, A. A., Stasyk, O. V., and Veenhuis, M. (2005). Pexophagy: the selective autophagy of peroxisomes. Autophagy, 1(2):75–83.

Feng, Y., He, D., Yao, Z., and Klionsky, D. J. (2014). The machinery of macroautophagy. Cell Res., 24(1):24–41.

Fossi, M., Linge, J., Labudde, D., Leitner, D., Nilges, M., and Oschkinat, H. (2005). Influence of chemical shift tolerances on NMR structure calculations using ARIA protocols for assigning NOE data. J. Biomol. NMR, 31(1):21–34.

Fu, M. M., Nirschl, J. J., and Holzbaur, E. L. (2014). LC3 binding to the scaffolding protein JIP1 regulates processive dynein-driven transport of autophagosomes. Dev. Cell, 29(5):577–590.

Fujita, N., Itoh, T., Omori, H., Fukuda, M., Noda, T., and Yoshimori, T. (2008). The Atg16L complex specifies the site of LC3 lipidation for membrane biogenesis in autophagy. Mol. Biol. Cell, 19(5):2092–2100.

Goldstein, R. A. (2008). The structure of protein evolution and the evolution of protein structure. Curr. Opin. Struct. Biol., 18(2):170–177.

Grzesiek, S., Anglister, J., and Bax, A. (1993). Correlation of Backbone Amide and Aliphatic Side-Chain Resonances in 13C/15N-Enriched Proteins by Isotropic Mixing of 13C Magnetization. J. Magn. Reson., Ser B, 101(1):114 – 119.

Grzesiek, S. and Bax, A. (1993). Amino acid type determination in the sequential assignment procedure of uniformly 13C/15N-enriched proteins. J. Biomol. NMR, 3(2):185–204.

Habeck, M., Rieping, W., Linge, J. P., and Nilges, M. (2004). Noe assignment with aria 2.0: The nuts and bolts. Methods Mol. Biol.: Protein NMR Techniques, 278:379–402.

He, H., Dang, Y., Dai, F., Guo, Z., Wu, J., She, X., Pei, Y., Chen, Y., Ling, W., Wu, C., Zhao, S., Liu, J. O., and Yu, L. (2003). Post-translational modifications of three members of the human MAP1LC3 family and detection of a novel type of modification for MAP1LC3B. J. Biol. Chem., 278(31):29278–29287.

Heras, B., Edeling, M. A., Byriel, K. A., Jones, A., Raina, S., and Martin, J. L. (2003). Dehydration converts DsbG crystal diffraction from low to high resolution. Structure, 11(2):139–145.

Heras, B. and Martin, J. L. (2005). Post-crystallization treatments for improving diffraction quality of protein crystals. Acta Crystallogr. D Biol. Crystallogr., 61(Pt 9):1173–1180.

Hochstrasser, M. (2000). Evolution and function of ubiquitin-like protein-conjugation systems. Nat. Cell Biol., 2(8):E153–157.

Huang, R., Xu, Y., Wan, W., Shou, X., Qian, J., You, Z., Liu, B., Chang, C., Zhou, T., Lippincott-Schwartz, J., and Liu, W. (2015). Deacetylation of nuclear LC3 drives autophagy initiation under starvation. Mol. Cell, 57(3):456–466.

Huang, W. P., Scott, S. V., Kim, J., and Klionsky, D. J. (2000). The itinerary of a vesicle component, Aut7p/Cvt5p, terminates in the yeast vacuole via the autophagy/Cvt pathways. J. Biol. Chem., 275(8):5845–5851.

Hyberts, S. G., Märki, W., and Wagner, G. (1987). Stereospecific assignments of side-chain protons and characterization of torsion angles in eglin c. Eur. Biophys. J., 164(3):625–635.

Ichimura, Y., Kirisako, T., Takao, T., Satomi, Y., Shimonishi, Y., Ishihara, N., Mizushima, N., Tanida, I., Kominami, E., Ohsumi, M., Noda, T., and Ohsumi, Y. (2000). A ubiquitin-like system mediates protein lipidation. Nature, 408(6811):488–492.

Ichimura, Y., Kumanomidou, T., Sou, Y. S., Mizushima, T., Ezaki, J., Ueno, T., Kominami, E., Yamane, T., Tanaka, K., and Komatsu, M. (2008). Structural basis for sorting mechanism of p62 in selective autophagy. J. Biol. Chem., 283(33):22847–22857.

Ikura, M., Kay, L. E., and Bax, A. (1990). A novel approach for sequential assignment of 1H, 13C, and 15N spectra of proteins: heteronuclear triple-resonance three-dimensional NMR spectroscopy. Application to calmodulin. Biochemistry, 29(19):4659–4667.

Ingles-Prieto, A., Ibarra-Molero, B., Delgado-Delgado, A., Perez-Jimenez, R., Fernandez, J. M., Gaucher, E. A., Sanchez-Ruiz, J. M., and Gavira, J. A. (2013). Conservation of protein structure over four billion years. Structure, 21(9):1690–1697.

Jacobsen, N. E. (2007). NMR Spectroscopy Explained: Simplified Theory, Applications and Examples for Organic Chemistry and Structural Biology. John Wiley & Son, 1st edition.

Jiang, H., Cheng, D., Liu, W., Peng, J., and Feng, J. (2010). Protein kinase C inhibits autophagy and phosphorylates LC3. Biochem. Biophys. Res. Commun., 395(4):471–476.

Kabeya, Y., Mizushima, N., Ueno, T., Yamamoto, A., Kirisako, T., Noda, T., Kominami, E., Ohsumi, Y., and Yoshimori, T. (2000). LC3, a mammalian homologue of yeast Apg8p, is localized in autophagosome membranes after processing. EMBO J., 19(21):5720–5728.

Karplus, M. and Anderson, D. H. (1959). Valence-bond interpretation of electron-coupled nuclear spin interactions; application to methane. J. Chem. Phys., 30(1):6–10.

Kay, L. E., Torchia, D. A., and Bax, A. (1989). Backbone dynamics of proteins as studied by 15N inverse detected heteronuclear NMR spectroscopy: application to staphylococcal nuclease. Biochemistry, 28(23):8972–8979.

Kim, J., Huang, W. P., and Klionsky, D. J. (2001). Membrane recruitment of Aut7p in the autophagy and cytoplasm to vacuole targeting pathways requires Aut1p, Aut2p, and the autophagy conjugation complex. J. Cell Biol., 152(1):51–64.

Kirisako, T., Baba, M., Ishihara, N., Miyazawa, K., Ohsumi, M., Yoshimori, T., Noda, T., and Ohsumi, Y. (1999). Formation process of autophagosome is traced with Apg8/Aut7p in yeast. J. Cell Biol., 147(2):435–446.

Kirisako, T., Ichimura, Y., Okada, H., Kabeya, Y., Mizushima, N., Yoshimori, T., Ohsumi, M., Takao, T., Noda, T., and Ohsumi, Y. (2000). The reversible modification regulates the membrane-binding state of Apg8/Aut7 essential for autophagy and the cytoplasm to vacuole targeting pathway. J. Cell Biol., 151(2):263–276.

Kirkin, V., Lamark, T., Sou, Y. S., Bjørkøy, G., Nunn, J. L., Bruun, J. A., Shvets, E., McEwan, D. G., Clausen, T. H., Wild, P., Bilusic, I., Theurillat, J. P., Øvervatn, A., Ishii, T., Elazar, Z., Komatsu, M., Dikic, I., and Johansen, T. (2009). A role for NBR1 in autophagosomal degradation of ubiquitinated substrates. Mol. Cell, 33(4):505–516.

Kleckner, I. R. and Foster, M. P. (2011). An introduction to NMR-based approaches for measuring protein dynamics. Biochim. Biophys. Acta, 1814(8):942–968.

Klionsky, D. J. (2008a). Autophagy revisited: a conversation with Christian de Duve. Autophagy, 4(6):740–743.

Klionsky, D. J., Cuervo, A. M., and Seglen, P. O. (2007). Methods for monitoring autophagy from yeast to human. Autophagy, 3(3):181–206.

Klionsky, D. J. and Schulman, B. A. (2014). Dynamic regulation of macroautophagy by distinctive ubiquitin-like proteins. Nat. Struct. Mol. Biol., 21(4):336–345.

Klionsky, D. J. e. a. (2008b). Guidelines for the use and interpretation of assays for monitoring autophagy in higher eukaryotes. Autophagy, 4(2):151–175.

Knight, D., Harris, R., McAlister, M. S., Phelan, J. P., Geddes, S., Moss, S. J., Driscoll, P. C., and Keep, N. H. (2002). The X-ray crystal structure and putative ligand-derived peptide binding properties of gamma-aminobutyric acid receptor type A receptor-associated protein. J. Biol. Chem., 277(7):5556–5561.

Kouno, T., Mizuguchi, M., Tanida, I., Ueno, T., Kanematsu, T., Mori, Y., Shinoda, H., Hirata, M., Kominami, E., and Kawano, K. (2005). Solution structure of microtubule-associated protein light chain 3 and identification of its functional subdomains. J. Biol. Chem., 280(26):24610–24617.

Kovacs, H. and Gossert, A. (2014). Improved NMR experiments with 13C-isotropic mixing for assignment of aromatic and aliphatic side chains in labeled proteins. J. Biomol. NMR, 58:101–112.

Krichel, C., Weiergraber, O. H., Pavlidou, M., Mohrluder, J., Schwarten, M., Willbold, D., and Neudecker, P. (2016). Sequence-specific (1)H, (15)N, and (13)C resonance assignments of the autophagy-related protein LC3C. Biomol NMR Assign, 10(1):41–43.

Kumeta, H., Watanabe, M., Nakatogawa, H., Yamaguchi, M., Ogura, K., Adachi, W., Fujioka, Y., Noda, N. N., Ohsumi, Y., and Inagaki, F. (2010). The NMR structure of the autophagy-related protein Atg8. J. Biomol. NMR, 47(3):237–241.

Kunkel, T. A. (1985). Rapid and efficient site-specific mutagenesis without phenotypic selection. PNAS, 82(2):488–492.

Kuznetsov, S. A. and Gelfand, V. I. (1987). 18 kDa microtubule-associated protein: identification as a new light chain (LC-3) of microtubule-associated protein 1 (MAP-1). FEBS Lett., 212(1):145–148.

Laemmli, U. K. (1970). Cleavage of structural proteins during the assembly of the head of bacteriophage T4. Nature, 227(5259):680–685.

Lakomek, N. A., Ying, J., and Bax, A. (2012). Measurement of 15N relaxation rates in perdeuterated proteins by TROSY-based methods. J. Biomol. NMR, 53(3):209–221.

Laskowski, R. A., MacArthur, M. W., Moss, D. S., and Thornton, J. M. (1993). PROCHECK: a program to check the stereochemical quality of protein structures. J. Appl. Cryst., 26:283–291.

Lecher, J. (2011). NMR studies on the islated C39 peptidase-like domain of ABC transporter Haemolysin B from E. coli: Investigation of the solution structure and the binding interface with HlyA. Dissertation, Heinrich Heine Universität Düsseldorf.

Lee, I. H., Cao, L., Mostoslavsky, R., Lombard, D. B., Liu, J., Bruns, N. E., Tsokos, M., Alt, F. W., and Finkel, T. (2008). A role for the NAD-dependent deacetylase Sirt1 in the regulation of autophagy. PNAS, 105(9):3374–3379.

Lee, I. H. and Finkel, T. (2009). Regulation of autophagy by the p300 acetyltransferase. J. Biol. Chem., 284(10):6322–6328.

Li, W. W., Li, J., and Bao, J. K. (2012). Microautophagy: lesser-known self-eating. Cell. Mol. Life Sci., 69(7):1125–1136.

Linge, J. P., O'Donoghue, S. I., and Nilges, M. (2001). Automated assignment of ambiguous nuclear overhauser effects with ARIA. Methods Enzymol., 339:71–90.

Lipari, G. and Szabo, A. (1982a). Model-free approach to the interpretation of nuclear magnetic resonance relaxation in macromolecules. 1. theory and range of validity. J. Am. Chem. Soc., 104(17):4546–4559.

Lipari, G. and Szabo, A. (1982b). Model-free approach to the interpretation of nuclear magnetic resonance relaxation in macromolecules. 2. analysis of experimental results. J. Am. Chem. Soc., 104(17):4559–4570.

Loria, J. P., Rance, M., and Palmer, A. G. (1999). A relaxation-compensated carr-purcell-meiboom-gill sequence for characterizing chemical exchange by nmr spectroscopy. J. Am. Chem. Soc., 121(10):2331–2332.

Ma, P., Schillinger, O., Schwarten, M., Lecher, J., Hartmann, R., Stoldt, M., Mohrluder, J., Olubiyi, O., Strodel, B., Willbold, D., and Weiergraber, O. H. (2015). Conformational Polymorphism in Autophagy-Related Protein GATE-16. Biochemistry, 54(35):5469–5479.

Mann, S. S. and Hammarback, J. A. (1994). Molecular characterization of light chain 3. A microtubule binding subunit of MAP1A and MAP1B. J. Biol. Chem., 269(15):11492–11497.

Markley, J. L., Bax, A., Arata, Y., Hilbers, C. W., Kaptein, R., Sykes, B. D., Wright, P. E., and Wuthrich, K. (1998). Recommendations for the presentation of NMR structures of proteins and nucleic acids. IUPAC-IUBMB-IUPAB Inter-Union Task Group on the Standardization of Data Bases of Protein and Nucleic Acid Structures Determined by NMR Spectroscopy. J. Biomol. NMR, 12(1):1–23.

Matsuura, A., Tsukada, M., Wada, Y., and Ohsumi, Y. (1997). Apg1p, a novel protein kinase required for the autophagic process in Saccharomyces cerevisiae. Gene, 192(2):245–250.

Mizushima, N., Noda, T., Yoshimori, T., Tanaka, Y., Ishii, T., George, M. D., Klionsky, D. J., Ohsumi, M., and Ohsumi, Y. (1998). A protein conjugation system essential for autophagy. Nature, 395(6700):395–398.

Mizushima, N., Ohsumi, Y., and Yoshimori, T. (2002). Autophagosome formation in mammalian cells. Cell Struct. Funct., 27(6):421–429.

Mizushima, N., Yamamoto, A., Matsui, M., Yoshimori, T., and Ohsumi, Y. (2004). In vivo analysis of autophagy in response to nutrient starvation using transgenic mice expressing a fluorescent autophagosome marker. Mol. Biol. Cell, 15(3):1101–1111.

Mizushima, N., Yoshimori, T., and Levine, B. (2010). Methods in mammalian autophagy research. Cell, 140(3):313–326.

Mizushima, N., Yoshimori, T., and Ohsumi, Y. (2011). The role of Atg proteins in autophagosome formation. Annu. Rev. Cell Dev. Biol., 27:107–132.

Murzin, A. G., Brenner, S. E., Hubbard, T., and Chothia, C. (1995). SCOP: a structural classification of proteins database for the investigation of sequences and structures. J. Mol. Biol., 247(4):536–540.

Nakatogawa, H., Ichimura, Y., and Ohsumi, Y. (2007). Atg8, a ubiquitin-like protein required for autophagosome formation, mediates membrane tethering and hemifusion. Cell, 130(1):165–178.

Nakatogawa, H., Suzuki, K., Kamada, Y., and Ohsumi, Y. (2009). Dynamics and diversity in autophagy mechanisms: lessons from yeast. Nat. Rev. Mol. Cell Biol., 10(7):458–467.

Nilges, M. (1995). Calculation of protein structures with ambiguous distance restraints. Automated assignment of ambiguous NOE crosspeaks and disulphide connectivities. J. Mol. Biol., 245(5):645–660.

Nilges, M., Bernard, A., Bardiaux, B., Malliavin, T., Habeck, M., and Rieping, W. (2008). Accurate NMR structures through minimization of an extended hybrid energy. Structure, 16(9):1305–1312.

Nilges, M., Macias, M. J., O'Donoghue, S. I., and Oschkinat, H. (1997). Automated NOESY interpretation with ambiguous distance restraints: the refined NMR solution structure of the pleckstrin homology domain from beta-spectrin. J. Mol. Biol., 269(3):408–422.

Noda, N. N., Kumeta, H., Nakatogawa, H., Satoo, K., Adachi, W., Ishii, J., Fujioka, Y., Ohsumi, Y., and Inagaki, F. (2008). Structural basis of target recognition by Atg8/LC3 during selective autophagy. Genes Cells, 13(12):1211–1218.

Novikoff, A. B., Beaufay, H., and de Duve, C. (1956). Electron microscopy of lysosomerich fractions from rat liver. J. Biochem. Bioph. Cytol., 2(4 Suppl):179–184.

Novikoff, A. B. and Essner, E. (1962). Cytolysomes and mitochondrial degeneration. J. Cell Biol., 15:140–146.

Orekhov, V. Y., Ibraghimov, I. V., and Billeter, M. (2001). MUNIN: a new approach to multi-dimensional NMR spectra interpretation. J. Biomol. NMR, 20(1):49–60.

Orengo, C. A., Jones, D. T., and Thornton, J. M. (1994). Protein superfamilies and domain superfolds. Nature, 372(6507):631–634.

Overington, J. P. (1992). Comparison of three-dimensional structures of homologous proteins. Curr. Opin. Struct. Biol., 2(3):394–401.

Pankiv, S., Clausen, T. H., Lamark, T., Brech, A., Bruun, J. A., Outzen, H., Øvervatn, A., Bjørkøy, G., and Johansen, T. (2007). p62/SQSTM1 binds directly to Atg8/LC3 to facilitate degradation of ubiquitinated protein aggregates by autophagy. J. Biol. Chem., 282(33):24131–24145.

Paz, Y., Elazar, Z., and Fass, D. (2000). Structure of GATE-16, membrane transport modulator and mammalian ortholog of autophagocytosis factor Aut7p. J. Biol. Chem., 275(33):25445–25450.

Pickart, C. M. (2001). Mechanisms underlying ubiquitination. Annu. Rev. Biochem., 70:503–533.

Pitt-Rivers, R. and Impiombato, F. S. (1968). The binding of sodium dodecyl sulphate to various proteins. Biochem. J., 109(5):825–830.

Rieping, W., Habeck, M., Bardiaux, B., Bernard, A., Malliavin, T. E., and Nilges, M. (2007). ARIA2: automated NOE assignment and data integration in NMR structure calculation. Bioinformatics, 23(3):381–382.

Rogov, V. V., Suzuki, H., Fiskin, E., Wild, P., Kniss, A., Rozenknop, A., Kato, R., Kawasaki, M., McEwan, D. G., Lohr, F., Guntert, P., Dikic, I., Wakatsuki, S., and Dotsch, V. (2013). Structural basis for phosphorylation-triggered autophagic clearance of Salmonella. Biochem. J., 454(3):459–466.

Rozenknop, A., Rogov, V. V., Rogova, N. Y., Lohr, F., Guntert, P., Dikic, I., and Dotsch, V. (2011). Characterization of the interaction of GABARAPL-1 with the LIR motif of NBR1. J. Mol. Biol., 410(3):477–487.

Rupp, B. (2009). Biomolecular Crystallography: Principles, Practice, and Application to Structural Biology. Garland Science, New York, 1st edition.

Sambrook, J. and Russell, D. W. (2001). Molecular Cloning: A Laboratory Manual. Cold Spring Harbor Laboratory Press, 3rd edition.

Sattler, M., Schleucher, J., and Griesinger, C. (1999). Heteronuclear multidimensional NMR experiments for the structure determination of proteins in solution employing pulsed field gradients. Prog. Nucl. Magn. Reson. Spectrosc., 34(2):93 – 158.

Schrödinger, LLC (2014). The PyMOL Molecular Graphics System, Version 1.7.2.1.

Schwarten, M., Stoldt, M., Mohrluder, J., and Willbold, D. (2010). Solution structure of Atg8 reveals conformational polymorphism of the N-terminal domain. Biochem. Biophys. Res. Commun., 395(3):426–431.

Serdyuk, I. N., Zaccai, N. R., and Zaccai, J. (2007). Methods in Molecular Biophysics: Structure, Dynamics, Function. Cambridge University Press, 1st edition.

Shakhnovich, B. E., Dokholyan, N. V., DeLisi, C., and Shakhnovich, E. I. (2003). Functional fingerprints of folds: evidence for correlated structure-function evolution. J. Mol. Biol., 326(1):1–9.

Shen, Y. and Bax, A. (2013). Protein backbone and sidechain torsion angles predicted from NMR chemical shifts using artificial neural networks. J. Biomol. NMR, 56(3):227–241.

Shpilka, T., Weidberg, H., Pietrokovski, S., and Elazar, Z. (2011). Atg8: an autophagy-related ubiquitin-like protein family. Genome Biol., 12(7):226.

Shvets, E., Fass, E., Scherz-Shouval, R., and Elazar, Z. (2008). The N-terminus and Phe52 residue of LC3 recruit p62/SQSTM1 into autophagosomes. J. Cell. Sci., 121(16):2685–2695.

Slabinski, L., Jaroszewski, L., Rodrigues, A. P., Rychlewski, L., Wilson, I. A., Lesley, S. A., and Godzik, A. (2007). The challenge of protein structure determination–lessons from structural genomics. Protein Sci., 16(11):2472–2482.

Sou, Y.-s., Tanida, I., Komatsu, M., Ueno, T., and Kominami, E. (2006). Phosphatidylserine in addition to phosphatidylethanolamine is an in vitro target of the mammalian atg8 modifiers, lc3, gabarap, and gate-16. J. Biol. Chem., 281(6):3017–3024.

Stangler, T., Mayr, L. M., and Willbold, D. (2002). Solution structure of human GABA(A) receptor-associated protein GABARAP: implications for biolgoical funcrion and its regulation. J. Biol. Chem., 277(16):13363–13366.

Studier, F. W. (2005). Protein production by auto-induction in high density shaking cultures. Protein Expr. Purif., 41(1):207–234.

Sugawara, K., Suzuki, N. N., Fujioka, Y., Mizushima, N., Ohsumi, Y., and Inagaki, F. (2004). The crystal structure of microtubule-associated protein light chain 3, a mammalian homologue of Saccharomyces cerevisiae Atg8. Genes Cells, 9(7):611–618.

Suzuki, H., Tabata, K., Morita, E., Kawasaki, M., Kato, R., Dobson, R. C., Yoshimori, T., and Wakatsuki, S. (2014). Structural basis of the autophagy-related LC3/Atg13 LIR complex: recognition and interaction mechanism. Structure, 22(1):47–58.

Suzuki, K., Kirisako, T., Kamada, Y., Mizushima, N., Noda, T., and Ohsumi, Y. (2001). The pre-autophagosomal structure organized by concerted functions of APG genes is essential for autophagosome formation. EMBO J., 20(21):5971–5981.

Suzuki, N. N., Yoshimoto, K., Fujioka, Y., Ohsumi, Y., and Inagaki, F. (2005). The crystal structure of plant ATG12 and its biological implication in autophagy. Autophagy, 1(2):119–126.

Takeshige, K., Baba, M., Tsuboi, S., Noda, T., and Ohsumi, Y. (1992). Autophagy in yeast demonstrated with proteinase-deficient mutants and conditions for its induction. J. Cell Biol., 119(2):301–311.

Tanida, I., Komatsu, M., Ueno, T., and Kominami, E. (2003). GATE-16 and GABARAP are authentic modifiers mediated by Apg7 and Apg3. Biochem. Biophys. Res. Commun., 300(3):637–644.

Tanida, I., Sou, Y. S., Ezaki, J., Minematsu-Ikeguchi, N., Ueno, T., and Kominami, E. (2004). HsAtg4B/HsApg4B/autophagin-1 cleaves the carboxyl termini of three human Atg8 homologues and delipidates microtubule-associated protein light chain 3- and GABAA receptor-associated protein-phospholipid conjugates. J. Biol. Chem., 279(35):36268–36276.

Thumm, M., Egner, R., Koch, B., Schlumpberger, M., Straub, M., Veenhuis, M., and Wolf, D. H. (1994). Isolation of autophagocytosis mutants of Saccharomyces cerevisiae. FEBS Lett., 349(2):275–280.

Tollinger, M., Skrynnikov, N. R., Mulder, F. A., Forman-Kay, J. D., and Kay, L. E. (2001). Slow dynamics in folded and unfolded states of an SH3 domain. J. Am. Chem. Soc., 123(46):11341–11352.

Tsukada, M. and Ohsumi, Y. (1993). Isolation and characterization of autophagy-defective mutants of Saccharomyces cerevisiae. FEBS Lett., 333(1-2):169–174.

Ubersax, J. A. and Ferrell, J. E. (2007). Mechanisms of specificity in protein phosphorylation. Nat. Rev. Mol. Cell Biol., 8(7):530–541.

Vadlamudi, R. K., Joung, I., Strominger, J. L., and Shin, J. (1996). p62, a phosphotyrosine-independent ligand of the SH2 domain of p56lck, belongs to a new class of ubiquitin-binding proteins. J. Biol. Chem., 271(34):20235–20237.

Verdin, E., Ott, M., and Allfrey, V. (2015). 50 years of protein acetylation: from gene regulation to epigenetics, metabolism and beyond. Nat. Rev. Mol. Cell Biol., 16(4):258–264.

von Muhlinen, N., Akutsu, M., Ravenhill, B. J., Foeglein, A., Bloor, S., Rutherford, T. J., Freund, S. M., Komander, D., and Randow, F. (2012). LC3C, bound selectively by

a noncanonical LIR motif in NDP52, is required for antibacterial autophagy. Mol. Cell, 48(3):329–342.

Vranken, W. F., Boucher, W., Stevens, T. J., Fogh, R. H., Pajon, A., Llinas, M., Ulrich, E. L., Markley, J. L., Ionides, J., and Laue, E. D. (2005). The CCPN data model for NMR spectroscopy: development of a software pipeline. Proteins, 59(4):687–696.

Vuister, G. W. and Bax, A. (1993). Quantitative j correlation: A new approach for measuring homonuclear three-bond j(hnha) coupling constants in 15n-enriched proteins. J. Am. Chem. Soc., 115(17):7772–7777.

Vuister, G. W. and Bax, A. (1994). Measurement of four-bond HN-Ha J-couplings in staphylococcal nuclease. J. Biomol. NMR, 4(2):193–200.

Wang, H., Bedford, F. K., Brandon, N. J., Moss, S. J., and Olsen, R. W. (1999). GABA(A)-receptor-associated protein links GABA(A) receptors and the cytoskeleton. Nature, 397(6714):69–72.

Wang, H. and Olsen, R. W. (2000). Binding of the GABA(A) receptor-associated protein (GABARAP) to microtubules and microfilaments suggests involvement of the cytoskeleton in GABARAPGABA(A) receptor interaction. J. Neurochem., 75(2):644–655.

Weidberg, H., Shvets, E., Shpilka, T., Shimron, F., Shinder, V., and Elazar, Z. (2010). LC3 and GATE-16/GABARAP subfamilies are both essential yet act differently in autophagosome biogenesis. EMBO J., 29(11):1792–1802.

Weiergräber, O. H., Mohrlüder, J., and Willbold, D. (2013). Atg8 Family Proteins — Autophagy and Beyond, Autophagy - A Double-Edged Sword - Cell Survival or Death? InTech.

Wheeler, M. J., Russi, S., Bowler, M. G., and Bowler, M. W. (2012). Measurement of the equilibrium relative humidity for common precipitant concentrations: facilitating controlled dehydration experiments. Acta Crystallogr. F Struct. Biol. Commun., 68(Pt 1):111–114.

Wild, P., Farhan, H., McEwan, D. G., Wagner, S., Rogov, V. V., Brady, N. R., Richter, B., Korac, J., Waidmann, O., Choudhary, C., Dötsch, V., Bumann, D., and Dikic, I.

(2011). Phosphorylation of the autophagy receptor optineurin restricts salmonella growth. Science, 333(6039):228–233.

Wittekind, M. and Muller, L. (1993). HNCACB, a High-Sensitivity 3D NMR Experiment to Correlate Amide-Proton and Nitrogen Resonances with the Alpha- and Beta-Carbon Resonances in Proteins. J. Magn. Reson., Ser B, 101(2):201 – 205.

Wüthrich, K. (1986). NMR of proteins and nucleic acids. John Wiley & Son, 1st edition.

Xie, Y., Kang, R., Sun, X., Zhong, M., Huang, J., Klionsky, D. J., and Tang, D. (2015). Posttranslational modification of autophagy-related proteins in macroautophagy. Autophagy, 11(1):28–45.

Xie, Z. and Klionsky, D. J. (2007). Autophagosome formation: core machinery and adaptations. Nat. Cell Biol., 9(10):1102–1109.

Xie, Z., Nair, U., and Klionsky, D. J. (2008). Atg8 controls phagophore expansion during autophagosome formation. Mol. Biol. Cell, 19(8):3290–3298.

Xin, Y., Yu, L., Chen, Z., Zheng, L., Fu, Q., Jiang, J., Zhang, P., Gong, R., and Zhao, S. (2001). Cloning, expression patterns, and chromosome localization of three human and two mouse homologues of GABA(A) receptor-associated protein. Genomics, 74(3):408–413.

Zhang, W., Smithgall, T., and Gmeiner, W. (1997). Three-dimensional structure of the Hck SH2 domain in solution. J. Biomol. NMR, 10(3):263–272.

A. Appendix

```
1  <!DOCTYPE project SYSTEM "project1.0.dtd">
2  <project name="ARIA_LC3C" version="1.0" author="carsten" date="2016" description="" comment="" references=""
       working_directory="/home/carsten/NMR_lc3c/analysis/aria" temp_root="/home/carsten/NMR_lc3c/analysis/aria/tmp" run="1"
       file_root="LC3C" cache="yes" cleanup="yes">
3    <data>
4      <ccpn_model filename="LC3C"/>
5      <molecule file="" format="ccpn" ccpn_id="LC3C_293K|A">
6        <linkage_definition name="automatic" filename=""/>
7        <parameter_definition name="automatic" filename=""/>
8        <topology_definition name="automatic" filename=""/>
9      </molecule>
10     <spectrum enabled="yes" use_assignments="yes" trust_assigned_peaks="no" structural_rules="no" filter_diagonal_peaks="yes
           " filter_unassigned_peaks="yes">
11       <shifts file="" format="ccpn" ccpn_id="LC3C|2" default_shift_error="0.0" use_shift_error="yes"/>
12       <peaks file="" format="ccpn" ccpn_id="LC3C|1|1|57" peak_size="volume" freq_window_proton1="0.02" freq_window_hetero1="
             0.2" freq_window_proton2="0.04" freq_window_hetero2="0.0">
13         <lower_bound_correction value="0.0" enabled="no"/>
14         <upper_bound_correction value="6.0" enabled="yes"/>
15       </peaks>
16       <experiment_data molecule_correlation_time="0.0" spectrum_mixing_time="0.0" spectrometer_frequency="0.0"
             ambiguity_type="intra"/>
17     </spectrum>
18     <spectrum enabled="yes" use_assignments="yes" trust_assigned_peaks="yes" structural_rules="no" filter_diagonal_peaks="
           yes" filter_unassigned_peaks="yes">
19       <shifts file="" format="ccpn" ccpn_id="LC3C|2" default_shift_error="0.0" use_shift_error="yes"/>
20       <peaks file="" format="ccpn" ccpn_id="LC3C|3|1|108" peak_size="volume" freq_window_proton1="0.02" freq_window_hetero1=
             "0.2" freq_window_proton2="0.05" freq_window_hetero2="0.2">
21         <lower_bound_correction value="0.0" enabled="no"/>
22         <upper_bound_correction value="6.0" enabled="yes"/>
23       </peaks>
24       <experiment_data molecule_correlation_time="0.0" spectrum_mixing_time="0.0" spectrometer_frequency="0.0"
             ambiguity_type="intra"/>
25     </spectrum>
26     <spectrum enabled="yes" use_assignments="yes" trust_assigned_peaks="yes" structural_rules="no" filter_diagonal_peaks="
           yes" filter_unassigned_peaks="yes">
27       <shifts file="" format="ccpn" ccpn_id="LC3C|2" default_shift_error="0.0" use_shift_error="yes"/>
28       <peaks file="" format="ccpn" ccpn_id="LC3C|17|1|26" peak_size="volume" freq_window_proton1="0.01" freq_window_hetero1=
             "0.0" freq_window_proton2="0.03" freq_window_hetero2="0.0">
29         <lower_bound_correction value="0.0" enabled="no"/>
30         <upper_bound_correction value="6.0" enabled="yes"/>
31       </peaks>
32       <experiment_data molecule_correlation_time="0.0" spectrum_mixing_time="0.0" spectrometer_frequency="0.0"
             ambiguity_type="intra"/>
33     </spectrum>
34     <spectrum enabled="yes" use_assignments="yes" trust_assigned_peaks="yes" structural_rules="no" filter_diagonal_peaks="
           yes" filter_unassigned_peaks="yes">
35       <shifts file="" format="ccpn" ccpn_id="LC3C|2" default_shift_error="0.0" use_shift_error="yes"/>
36       <peaks file="" format="ccpn" ccpn_id="LC3C|3|1|127" peak_size="volume" freq_window_proton1="0.05" freq_window_hetero1=
             "0.5" freq_window_proton2="0.02" freq_window_hetero2="0.5">
37         <lower_bound_correction value="0.0" enabled="no"/>
38         <upper_bound_correction value="5.5" enabled="yes"/>
39       </peaks>
40       <experiment_data molecule_correlation_time="0.0" spectrum_mixing_time="0.0" spectrometer_frequency="0.0"
             ambiguity_type="intra"/>
41     </spectrum>
```

```
42    <jcouplings file="" format="ccpn" ccpn_id="52|1" enabled="no" parameter_class="1"/>
43    <hbonds file="" format="ccpn" ccpn_id="39|20" enabled="yes" data_type="standard"/>
44    <dihedrals file="" format="ccpn" ccpn_id="39|16" enabled="yes" data_type="standard"/>
45    <dihedrals file="" format="ccpn" ccpn_id="37|33" enabled="yes" data_type="talos"/>
46    <symmetry enabled="no" method="standard" n_monomers="1" symmetry_type="None" ncs_enabled="no" packing_enabled="no"/>
47    <initial_structure file="" format="iupac" ccpn_id="" enabled="no"/>
48  </data>
49  <structure_generation engine="cns">
50    <cns local_executable="/opt/scisoft/usr/bin/cns_remote" keep_output="yes" keep_restraint_files="yes" create_psf_file="
          yes" generate_template="yes" nonbonded_parameters="PARALLHDG">
51      <annealing_parameters>
52        <unambiguous_restraints first_iteration="0" k_hot="10.0" k_cool1_initial="10.0" k_cool1_final="50.0" k_cool2="50.0"/
              >
53        <ambiguous_restraints first_iteration="0" k_hot="10.0" k_cool1_initial="10.0" k_cool1_final="50.0" k_cool2="50.0"/>
54        <hbond_restraints first_iteration="0" k_hot="10.0" k_cool1_initial="10.0" k_cool1_final="50.0" k_cool2="50.0"/>
55        <dihedral_restraints k_hot="5.0" k_cool1="25.0" k_cool2="200.0"/>
56        <karplus_restraints parameter_class="1" a="6.98" b="-1.38" c="1.72" d="-60.0" k_hot="0.0" k_cool1="0.2" k_cool2="1.0
              "/>
57        <karplus_restraints parameter_class="2" a="6.98" b="-1.38" c="1.72" d="-60.0" k_hot="0.0" k_cool1="0.2" k_cool2="1.0
              "/>
58        <karplus_restraints parameter_class="3" a="6.98" b="-1.38" c="1.72" d="-60.0" k_hot="0.0" k_cool1="0.2" k_cool2="1.0
              "/>
59        <karplus_restraints parameter_class="4" a="6.98" b="-1.38" c="1.72" d="-60.0" k_hot="0.0" k_cool1="0.2" k_cool2="1.0
              "/>
60        <karplus_restraints parameter_class="5" a="6.98" b="-1.38" c="1.72" d="-60.0" k_hot="0.0" k_cool1="0.2" k_cool2="1.0
              "/>
61        <rdc_restraints parameter_class="1" method="SANI" first_iteration="0" k_hot="0.0" k_cool1="0.2" k_cool2="1.0" r="0.4
              " d="8.0" border_hot_initial="0.1" border_hot_final="40.0" border_cool1_initial="40.0" border_cool1_final="
              40.0" border_cool2_initial="40.0" border_cool2_final="40.0" center_hot_initial="0.1" center_hot_final="0.1"
              center_cool1_initial="10.0" center_cool1_final="10.0" center_cool2_initial="10.0" center_cool2_final="10.0"/>
62        <rdc_restraints parameter_class="2" method="SANI" first_iteration="0" k_hot="0.0" k_cool1="0.2" k_cool2="1.0" r="0.4
              " d="8.0" border_hot_initial="0.1" border_hot_final="40.0" border_cool1_initial="40.0" border_cool1_final="
              40.0" border_cool2_initial="40.0" border_cool2_final="40.0" center_hot_initial="0.1" center_hot_final="0.1"
              center_cool1_initial="10.0" center_cool1_final="10.0" center_cool2_initial="10.0" center_cool2_final="10.0"/>
63        <rdc_restraints parameter_class="3" method="SANI" first_iteration="0" k_hot="0.0" k_cool1="0.2" k_cool2="1.0" r="0.4
              " d="8.0" border_hot_initial="0.1" border_hot_final="40.0" border_cool1_initial="40.0" border_cool1_final="
              40.0" border_cool2_initial="40.0" border_cool2_final="40.0" center_hot_initial="0.1" center_hot_final="0.1"
              center_cool1_initial="10.0" center_cool1_final="10.0" center_cool2_initial="10.0" center_cool2_final="10.0"/>
64        <rdc_restraints parameter_class="4" method="SANI" first_iteration="0" k_hot="0.0" k_cool1="0.2" k_cool2="1.0" r="0.4
              " d="8.0" border_hot_initial="0.1" border_hot_final="40.0" border_cool1_initial="40.0" border_cool1_final="
              40.0" border_cool2_initial="40.0" border_cool2_final="40.0" center_hot_initial="0.1" center_hot_final="0.1"
              center_cool1_initial="10.0" center_cool1_final="10.0" center_cool2_initial="10.0" center_cool2_final="10.0"/>
65        <rdc_restraints parameter_class="5" method="SANI" first_iteration="0" k_hot="0.0" k_cool1="0.2" k_cool2="1.0" r="0.4
              " d="8.0" border_hot_initial="0.1" border_hot_final="40.0" border_cool1_initial="40.0" border_cool1_final="
              40.0" border_cool2_initial="40.0" border_cool2_final="40.0" center_hot_initial="0.1" center_hot_final="0.1"
              center_cool1_initial="10.0" center_cool1_final="10.0" center_cool2_initial="10.0" center_cool2_final="10.0"/>
66        <flat_bottom_harmonic_wall m_rswitch_hot="0.5" m_rswitch_cool1="0.5" m_rswitch_cool2="0.5" rswitch_hot="0.5"
              rswitch_cool1="0.5" rswitch_cool2="0.5" m_asymptote_hot="-1.0" m_asymptote_cool1="-1.0" m_asymptote_cool2="
              -0.1" asymptote_hot="1.0" asymptote_cool1="1.0" asymptote_cool2="0.1"/>
67        <symmetry_restraints k_packing_hot="15.0" k_packing_cool1="10.0" k_packing_cool2="5.0" last_iteration_packing="8"
              k_ncs="50.0"/>
68        <logharmonic_potential enabled="no" use_auto_weight="yes" weight_unambig="25.0" weight_ambig="25.0" weight_hbond="
              25.0"/>
69      </annealing_parameters>
70      <md_parameters dynamics="torsion" random_seed="89764443" tad_temp_high="10000.0" tad_timestep_factor="9.0"
            cartesian_temp_high="2000.0" cartesian_first_iteration="0" timestep="0.003" temp_cool1_final="1000.0"
            temp_cool2_final="50.0" steps_high="10000" steps_refine="4000" steps_cool1="20000" steps_cool2="20000"/>
71    </cns>
72    <job_manager default_command="csh -f">
73      <host enabled="yes" command="qsub -S /opt/scisoft/bin/csh" executable="/opt/scisoft/usr/bin/cns_remote" n_cpu="100"
            use_absolute_path="yes"/>
74    </job_manager>
75  </structure_generation>
76  <protocol floating_assignment="yes">
77    <iteration number="0" n_structures="30" sort_criterion="total_energy" n_best_structures="10" n_kept_structures="0">
78      <assignment/>
79      <merging method="standard"/>
80      <calibration relaxation_matrix="no" distance_cutoff="6.0" estimator="ratio_of_averages" error_estimator="distance"/>
81      <violation_analysis violation_tolerance="1000.0" violation_threshold="0.5"/>
```

```
82      <partial_assignment weight_threshold="1.0" max_contributions="20"/>
83      <network_anchoring high_residue_threshold="4.0" enabled="yes" min_residue_threshold="1.0" min_atom_threshold="0.25"/>
84    </iteration>
85    <iteration number="1" n_structures="30" sort_criterion="total_energy" n_best_structures="10" n_kept_structures="0">
86      <assignment/>
87      <merging method="standard"/>
88      <calibration relaxation_matrix="no" distance_cutoff="6.0" estimator="ratio_of_averages" error_estimator="distance"/>
89      <violation_analysis violation_tolerance="5.0" violation_threshold="0.5"/>
90      <partial_assignment weight_threshold="0.9999" max_contributions="20"/>
91      <network_anchoring high_residue_threshold="4.0" enabled="yes" min_residue_threshold="1.0" min_atom_threshold="0.25"/>
92    </iteration>
93    <iteration number="2" n_structures="30" sort_criterion="total_energy" n_best_structures="10" n_kept_structures="0">
94      <assignment/>
95      <merging method="standard"/>
96      <calibration relaxation_matrix="no" distance_cutoff="6.0" estimator="ratio_of_averages" error_estimator="distance"/>
97      <violation_analysis violation_tolerance="3.0" violation_threshold="0.5"/>
98      <partial_assignment weight_threshold="0.999" max_contributions="20"/>
99      <network_anchoring high_residue_threshold="4.0" enabled="yes" min_residue_threshold="1.0" min_atom_threshold="0.25"/>
100   </iteration>
101   <iteration number="3" n_structures="30" sort_criterion="total_energy" n_best_structures="10" n_kept_structures="0">
102     <assignment/>
103     <merging method="standard"/>
104     <calibration relaxation_matrix="no" distance_cutoff="6.0" estimator="ratio_of_averages" error_estimator="distance"/>
105     <violation_analysis violation_tolerance="1.0" violation_threshold="0.5"/>
106     <partial_assignment weight_threshold="0.99" max_contributions="20"/>
107     <network_anchoring high_residue_threshold="4.0" enabled="yes" min_residue_threshold="1.0" min_atom_threshold="0.25"/>
108   </iteration>
109   <iteration number="4" n_structures="30" sort_criterion="total_energy" n_best_structures="10" n_kept_structures="0">
110     <assignment/>
111     <merging method="standard"/>
112     <calibration relaxation_matrix="no" distance_cutoff="6.0" estimator="ratio_of_averages" error_estimator="distance"/>
113     <violation_analysis violation_tolerance="1.0" violation_threshold="0.5"/>
114     <partial_assignment weight_threshold="0.98" max_contributions="20"/>
115     <network_anchoring high_residue_threshold="4.0" enabled="yes" min_residue_threshold="1.0" min_atom_threshold="0.25"/>
116   </iteration>
117   <iteration number="5" n_structures="30" sort_criterion="total_energy" n_best_structures="10" n_kept_structures="0">
118     <assignment/>
119     <merging method="standard"/>
120     <calibration relaxation_matrix="no" distance_cutoff="6.0" estimator="ratio_of_averages" error_estimator="distance"/>
121     <violation_analysis violation_tolerance="1.0" violation_threshold="0.5"/>
122     <partial_assignment weight_threshold="0.96" max_contributions="20"/>
123     <network_anchoring high_residue_threshold="4.0" enabled="yes" min_residue_threshold="1.0" min_atom_threshold="0.25"/>
124   </iteration>
125   <iteration number="6" n_structures="30" sort_criterion="total_energy" n_best_structures="10" n_kept_structures="0">
126     <assignment/>
127     <merging method="standard"/>
128     <calibration relaxation_matrix="no" distance_cutoff="6.0" estimator="ratio_of_averages" error_estimator="distance"/>
129     <violation_analysis violation_tolerance="0.1" violation_threshold="0.5"/>
130     <partial_assignment weight_threshold="0.93" max_contributions="20"/>
131     <network_anchoring high_residue_threshold="4.0" enabled="yes" min_residue_threshold="1.0" min_atom_threshold="0.25"/>
132   </iteration>
133   <iteration number="7" n_structures="30" sort_criterion="total_energy" n_best_structures="10" n_kept_structures="0">
134     <assignment/>
135     <merging method="standard"/>
136     <calibration relaxation_matrix="no" distance_cutoff="6.0" estimator="ratio_of_averages" error_estimator="distance"/>
137     <violation_analysis violation_tolerance="0.1" violation_threshold="0.5"/>
138     <partial_assignment weight_threshold="0.9" max_contributions="20"/>
139     <network_anchoring high_residue_threshold="4.0" enabled="yes" min_residue_threshold="1.0" min_atom_threshold="0.25"/>
140   </iteration>
141   <iteration number="8" n_structures="100" sort_criterion="total_energy" n_best_structures="10" n_kept_structures="0">
142     <assignment/>
143     <merging method="standard"/>
144     <calibration relaxation_matrix="no" distance_cutoff="6.0" estimator="ratio_of_averages" error_estimator="distance"/>
145     <violation_analysis violation_tolerance="0.1" violation_threshold="0.5"/>
146     <partial_assignment weight_threshold="0.8" max_contributions="20"/>
147     <network_anchoring high_residue_threshold="4.0" enabled="yes" min_residue_threshold="1.0" min_atom_threshold="0.25"/>
148   </iteration>
149   <water_refinement solvent="water" n_structures="10" enabled="yes" write_solvent_molecules="no"/>
150 </protocol>
```

```
151   <analysis>
152     <structures_analysis enabled="yes"/>
153     <procheck executable="/opt/scisoft64/usr/bin/procheck" enabled="yes"/>
154     <prosa executable="/usr/bin/prosa" enabled="no"/>
155     <whatif executable="/opt/scisoft64/usr/local/nmrlocal/lib/whatif/src/whatif" enabled="yes"/>
156     <clashlist executable="/opt/scisoft64/usr/bin/clashlist" enabled="yes"/>
157   </analysis>
158   <report>
159     <ccpn export_assignments="yes" export_noe_restraint_list="last" export_structures="yes"/>
160     <molmol enabled="yes"/>
161     <noe_restraint_list pickle_output="yes" text_output="yes" xml_output="yes"/>
162     <spectra write_assigned="no" write_assigned_force="no" iteration="last" write_unambiguous_only="no"/>
163   </report>
164 </project>
```

Die hier vorliegende Dissertation habe ich eigenständig und ohne unerlaubte Hilfe angefertigt. Die Dissertation wurde in der vorgelegten oder in ähnlicher Form noch bei keiner anderen Institution eingereicht. Ich habe bislang keine erfolglosen Promotionsversuche unternommen.

Carsten Krichel
Jülich, den 22.04.2016